

NASA TECHNICAL NOTE



NASA TN D-3217

LOAN COPY: REI  
AFWL (WLI)  
KIRTLAND AFB,

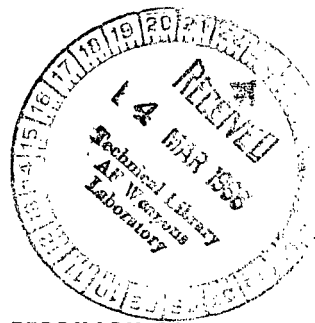


TECH LIBRARY KAFB, NM

NASA TN D-3217

# LONGITUDINAL AERODYNAMIC CHARACTERISTICS OF A FLAPPED TILT-WING FOUR-PROPELLER V/STOL TRANSPORT MODEL

*by Kenneth W. Goodson  
Langley Research Center  
Langley Station, Hampton, Va.*





LONGITUDINAL AERODYNAMIC CHARACTERISTICS OF A  
FLAPPED TILT-WING FOUR-PROPELLER  
V/STOL TRANSPORT MODEL

By Kenneth W. Goodson

Langley Research Center  
Langley Station, Hampton, Va.

NATIONAL AERONAUTICS AND SPACE ADMINISTRATION

---

For sale by the Clearinghouse for Federal Scientific and Technical Information  
Springfield, Virginia 22151 - Price \$4.00

LONGITUDINAL AERODYNAMIC CHARACTERISTICS OF A  
FLAPPED TILT-WING FOUR-PROPELLER  
V/STOL TRANSPORT MODEL

By Kenneth W. Goodson  
Langley Research Center

SUMMARY

An investigation of the aerodynamic characteristics of a 1/11-scale model of a four-propeller tilt-wing V/STOL transport configuration has been conducted in the 17-foot test section of the Langley 300-MPH 7- by 10-foot tunnel. Tests were made of the model through the transition-speed range for various combinations of wing tilt angle and thrust coefficient using propellers having a blade pitch of  $12^{\circ}$ . Some tests were made in ground effect.

Tuft studies indicate that flow separation occurs at descent angles of about  $6^{\circ}$  at some transition speeds. The descent capability, therefore, should be at least  $6^{\circ}$  and may be greater depending on the intensity of buffet encountered on the actual aircraft. Considerable improvement in descent capability was obtained by extending and drooping the leading edge of the wing or by using a lower propeller-blade pitch angle of  $8^{\circ}$ .

INTRODUCTION

The results obtained from various tilt-wing V/STOL investigations (refs. 1 to 15) indicate that the flapped tilt wing is an attractive configuration for a vertical-take-off-and-landing aircraft. One of the primary problems of a tilt-wing configuration is the wing stall in transition and the associated limit on rate of descent and deceleration capability. (See ref. 16.)

The present investigation was undertaken to study these problems in transition both in and out of ground effect on a four-propeller tilt-wing configuration. The investigation was conducted on a 1/11-scale model in the 17-foot test section of the Langley 300-MPH 7- by 10-foot wind tunnel. Other work on this configuration is reported in references 17 and 18. Flight tests on this configuration are being conducted.

## SYMBOLS AND COEFFICIENTS

This investigation covered the conditions representing the complete transition-speed range from hovering to conventional flight. In order to avoid the problems of conventional coefficients approaching infinity as the hover condition is approached, the data are presented in the form of coefficients based on the dynamic pressure in the slipstream. These coefficients reduce to the conventional form at zero thrust, that is, power-off test conditions. The coefficients based on slipstream dynamic pressure are indicated by the subscript *s*. The slipstream coefficients can be converted to conventional coefficients by dividing by  $(1 - C_{T,s})$ ; that is,

$$C_L = \frac{C_{L,s}}{(1 - C_{T,s})}$$

The positive direction of forces, moments, and angles is indicated in figure 1. Data for the complete model are presented about the stability axes with moments presented about the center of gravity as shown in figures 1(a) and 2. The propeller data are presented about the body axis, with propeller moments referred to the center of the propeller. (See fig. 1(b).)

Measurements for this investigation were taken in the U.S. Customary System of Units. Equivalent values are indicated herein in the International System of Units (SI) in the interest of promoting the use of this system in future NASA reports. Details concerning the use of SI, together with physical constants and conversion factors, are given in reference 19. (Also, see appendix.)

*b* wing span, ft (meters)

*c* wing chord, ft (meters)

$\bar{c}$  wing mean geometric chord, ft (meters)

$C_D$  drag coefficient based on free stream,  $\frac{\text{Drag}}{qS}$

$C_L$  lift coefficient based on free stream,  $\frac{\text{Lift}}{qS}$

$C_m$  pitching-moment coefficient based on free stream,  $\frac{\text{Pitching moment}}{qS\bar{c}}$

$C_l$  rolling-moment coefficient based on free stream,  $\frac{\text{Rolling moment}}{qSb}$

$C_n$	yawing-moment coefficient based on free stream, $\frac{\text{Yawing moment}}{qSb}$
$C_Y$	side-force coefficient based on free stream, $\frac{\text{Side force}}{qS}$
$C_{D,s}$	drag coefficient based on slipstream, $\frac{\text{Drag}}{q_s S}$
$C_{L,s}$	lift coefficient based on slipstream, $\frac{\text{Lift}}{q_s S}$
$C_{m,s}$	pitching-moment coefficient based on slipstream, $\frac{\text{Pitching moment}}{q_s S \bar{c}}$
$C_{T,s}$	averaged slipstream thrust coefficient based on slipstream and total thrust of all propellers, $\frac{\text{Thrust}}{q_s N \frac{\pi D^2}{4}}$
$(C_{T,s})_{\text{nom}}$	nominal thrust coefficient used to identify curves, usually $C_{T,s}$ , at $\alpha = 0^\circ$
$C_{T,s,p}$	slipstream thrust coefficient of individual propeller, $\frac{\text{Propeller thrust}}{q_s \frac{\pi D^2}{4}}$
$C_T$	thrust coefficient of individual propeller, $\frac{\text{Propeller thrust}}{\rho n^2 D^4}$
$C_p$	power coefficient of individual propeller, $\frac{2\pi n Q}{\rho n^3 D^5}$
$C_{N,p}$	normal-force coefficient of individual propeller, $\frac{\text{Propeller normal force}}{q_s S}$
$C_{m,p}$	pitching-moment coefficient of individual propeller, $\frac{\text{Propeller pitching moment}}{q_s S \bar{c}}$
$C_{Y,p}$	side-force coefficient of individual propeller, $\frac{\text{Propeller side force}}{q_s S}$
$C_{n,p}$	yawing-moment coefficient of individual propeller, $\frac{\text{Propeller yawing moment}}{q_s S b}$
$D$	propeller diameter, ft (meters)
$h$	fuselage bottom height above ground, ft (meters)
$h/\bar{c}$	ratio of fuselage height to wing mean geometric chord

$i_t$	horizontal-tail incidence angle with respect to fuselage reference line, deg
$i_w$	wing-incidence angle with respect to fuselage reference line, deg
$M$	pitching moment, ft-lbs (meter-newtons)
$N$	number of propellers
$n$	propeller revolution per second, rps
$p_b$	pressure on fuselage bottom, lb/ft <sup>2</sup> (newtons/meter <sup>2</sup> )
$Q$	propeller torque, ft-lbs (meter-newtons)
$q$	free-stream dynamic pressure, $\frac{1}{2}\rho V^2$ , lb/ft <sup>2</sup> (newtons/meter <sup>2</sup> )
$q_s$	slipstream dynamic pressure, $q + \frac{T}{\frac{N\pi D^2}{4}}$ , lb/ft <sup>2</sup> (newtons/meter <sup>2</sup> )
$R$	maximum radius of propeller, ft (meters)
$r$	propeller radius to any section, ft (meters)
$S$	wing area, ft <sup>2</sup> (meters <sup>2</sup> )
$T$	total thrust of all propellers, lbs (newtons)
$T_p$	thrust of single propeller, lbs (newtons)
$V$	free-stream velocity, ft/sec or knots (meters/sec)
$v$	propeller-induced velocity, ft/sec (meters/sec)
$W$	weight of aircraft, lbs (newtons)
$x$	distance along bottom of fuselage from center line of inboard propellers when tilted up to 90° (see fig. 2), ft (meters)
$\alpha$	angle of attack of fuselage reference line, deg

$\beta$	angle of sideslip, deg
$\beta_{.75R}$	propeller blade angle, measured at the 75-percent radius location, deg
$\gamma$	flight-path angle, $\tan^{-1} \frac{C_D}{C_L}$ , deg
$\delta_f$	flap deflection, deg
$\delta_v$	vane deflection, deg
$\delta_n$	leading-edge nose-droop angle, deg
$\rho$	mass density of air, slugs/cu ft (kilograms/meter <sup>3</sup> )
Subscript:	
max	maximum

## MODEL AND APPARATUS

A drawing of the 1/11-scale complete model showing the important dimensions and other physical characteristics is presented in figure 2. The drawing shows the wing at zero and 90° incidence. The wing construction consisted of an aluminum box spar covered with mahogany to obtain the airfoil contours. The wing was fitted with a double slotted flap (see fig. 3). The propellers were mounted 5.6 percent propeller diameter below the section wing chord line. When the double slotted flap was deflected 0°, 40°, and 60°, the flap vane angle was 0°, 10°, and 30°, respectively.

The fuselage was constructed with an aluminum strongback covered with mahogany panels. A sketch showing the fuselage cross sections is presented in figure 4. The wing-incidence angle could be changed remotely through an angle range from 0° to 90° with an electric motor operated mechanism; the angle was determined with a calibrated linear slide-wire potentiometer. Wing-fuselage ramps used to improve the airflow in the center section are shown in figure 5.

The horizontal tail could be set at various incidence angles. The geometric characteristics of the propellers are shown in figure 6. The four-blade propellers were constructed of resin-bonded glass fibers over a balsa wood core. The propellers were driven by four variable-frequency  $7\frac{1}{2}$ -horsepower electric motors. The directions of rotation are shown in figure 2. Each electric motor was instrumented to record the

propeller thrust, torque, normal force, and pitching moment, or if rotated  $90^{\circ}$  about its axis, to record the side force and yawing moment.

Photographs of the sting-supported model mounted on an electrical strain-gage balance in the 17-foot test section are shown in figure 7. Figure 7(b) shows tufts on the wing and fuselage which were used to study the airflow near a fixed ground board.

Figure 8 shows details of two leading-edge slat configurations used on the model. Figure 9 shows the wing chord extended 10 percent with the 10-percent-chord leading edge drooped  $10^{\circ}$ . Location of pressure orifices on the bottom of the fuselage is shown in figure 10.

## TESTS

The investigation was conducted in the 17-foot test section of the Langley 300-MPH 7- by 10-foot tunnel which is described in reference 2.

Power-off (propeller removed) tests were made at a free-stream dynamic pressure of approximately 10 pounds per square foot (478.8 newtons/meter<sup>2</sup>). Power-on tests were made over a slipstream thrust-coefficient range from 0 to 1.0.

Thrust-coefficient calibrations were obtained by setting the model wing and fuselage at zero angle of attack and measuring the model drag through a tunnel speed range for power-off (propellers removed) and power-on (constant propeller revolutions per minute and constant propeller-blade pitch angle). These results were used to compute thrust-coefficient variation with tunnel speed. From a curve of these results, the tunnel speed desired for a given thrust coefficient (with propeller rotational speed held constant at the calibrated value) at zero fuselage angle of attack could be determined for the various wing-flap conditions. The thrust coefficient established at zero angle of attack, however, did not remain constant with change in model angle of attack because of change in propeller characteristics with change in angle of attack as seen on the various data figures. The solid symbols on the figures indicate zero angle of attack.

It should be noted here that, at the beginning of the test program, the thrust of all propellers was matched through the speed range; however, as will be noted in the propeller data for some wing-flap thrust-coefficient conditions, this match did not hold, as is discussed in the section entitled "Effect of Propeller Blade Pitch."

Ground-effect tests were made at two heights ( $h/\bar{c} = 0.74$  and  $2.70$ ) over the fixed ground board. The model heights were measured relative to the bottom of the fuselage. The propeller rotational speed used in the ground-effect tests (7500 rpm) was higher than that used out of ground effect (7000 rpm) because of warpage of the propeller blades which occurred during the several months between the out-of-ground-effect tests and the

in-ground-effect tests. To correct for this warpage, the propeller rotational speed was adjusted to give approximately the same thrust as that used for the earlier runs.

The Reynolds number of these tests based on the wing mean aerodynamic chord of 8.8 inches (22.35 cm) and the aforementioned slipstream dynamic pressure was about  $0.51 \times 10^6$ .

A study of the effects of tunnel walls on the aerodynamic characteristics of V/STOL configurations (ref. 20) using the method of reference 21 shows that, for small model-to-tunnel-size ratios, the corrections to lift and drag are small. This study (ref. 20) also shows that corrections to the pitching moments are in the wrong direction. In view of these findings and the relatively small size of the present model, model corrections have not been applied to the present results.

## PRESENTATION OF RESULTS

Results of the present investigation are presented in the following figures:

	Figure
Out of ground effect –	
Comparison with and without tufts . . . . .	11
Effect of thrust coefficient . . . . .	12 to 14
Effect of wing incidence . . . . .	15 to 16
Effect of horizontal stabilizer:	
(a) Power off (propellers off) . . . . .	17
(b) Power on . . . . .	18 to 21
Effect of propeller-blade angle (also includes propeller force and moment data):	
(a) $\beta_{.75R} = 12^\circ$ . . . . .	22
(b) $\beta_{.75R} = 8^\circ$ . . . . .	23
Comparison of $S_1$ to $S_2$ slats . . . . .	24
Leading-edge chord extension with nose droop . . . . .	25
In ground effect –	
Effect of thrust coefficient (also includes propeller force and moment data):	
(a) $h/\bar{c} = 0.74$ . . . . .	26
(b) $h/\bar{c} = 2.70$ . . . . .	27
Pressure ratio on bottom of fuselage . . . . .	28
Tuft studies . . . . .	29 to 33
Transition characteristics –	
Assumed wing-tilt flap-deflection program . . . . .	34
Transition characteristics at fixed wing incidences . . . . .	35

	Figure
Effect of horizontal tail . . . . .	36
Descent and deceleration characteristics:	
Comparison of criteria . . . . .	37
Effect of flap deflection . . . . .	38
Effect of various alterations including ground effect . . . . .	39

## DISCUSSION

Many of the results obtained in this investigation are similar to those obtained on other tilt-wing configurations (refs. 1 to 15) and are, therefore, not discussed in detail. The data are presented, however, to be available for future analysis and correlation with flight and large-scale-model results. The discussion is restricted primarily to those items related to the problem of wing stall in transition and the associated descent and deceleration limitations which was the primary purpose of the investigation.

### Transition Characteristics

The significant results of the investigation can be discussed best on the basis of the transition characteristics of an assumed airplane as calculated from the basic data. For this purpose the model was assumed to be a 1/11-scale model of an airplane operating at a wing loading of 70 pounds per square foot (3350 newtons per square meter). The flap was assumed to be programmed to deflect with wing incidence as shown in figure 34 with the 60° flap deflection representing a landing-flap condition and the 40° deflection representing take-off flaps. The symbols in figure 34 represent combinations of flap deflection and wing incidence for which basic data are presented.

Typical variations of pitching moment, fuselage angle of attack, and thrust required for steady-level flights are shown in figure 35 for selected wing-incidence angles representing the landing-flap program. Except for large negative angles of attack of the fuselage, the thrust required is relatively independent of wing incidence; that is (as also shown in fig. 16), the transition characteristics are dependent on the angle of attack of the wing (wing incidence plus fuselage angle of attack) with respect to the free-stream flow and are little affected by the fuselage attitude with respect to this flow at the relatively low speeds involved in transition. At the higher speeds the change in drag with fuselage attitude would be more important, but this drag effect is not significant in the range of the present tests.

The wing incidence required for transition with zero fuselage attitude (with the landing-flap program) and the effects of horizontal-tail incidence are presented in figure 36. The stabilizer settings required for trim at the high-speed end of transition

were not covered in the basic data; but, the reduction in effectiveness of the tail as a trimming device as the speed is reduced is readily apparent from the comparison of the moments for  $10^\circ$  and  $20^\circ$  stabilizer setting. The tail rotor that would be required for trim and control at low speeds was not included on the model.

### Descent Characteristics

One of the main purposes of the investigation was to study the wing stall in transition and to determine the relation of the onset of stall to the descent and deceleration characteristics of the configuration. The wing of the model was, therefore, covered with tufts in order to obtain a visual indication of flow separation to correlate with the force data. As shown in figure 11, these tufts caused a small reduction in lift and an increase in drag on the configuration with the flaps retracted. These effects were accepted in order to be able to study the stall pattern in the transition range.

Two possible methods of determining the descent boundary were investigated: One method, referred to as the  $C_{L,max}$  boundary, was based on the drag-lift ratio achieved at maximum lift coefficient. The other, referred to as  $C_{L,tuft}$  stall, is based on the drag-lift ratio at which flow breakdown (as indicated by the tufts, figs. 29 to 33) occurred on the part of the wing in the propeller slipstream. Descent boundaries for the fuselage level attitude obtained by using the present data at  $C_{L,max}$  and at  $C_{L,tuft}$  stall are presented in figure 37. The descent boundary based on  $C_{L,max}$  shows a descent capability of about  $-4^\circ$  for  $i_w \approx 20^\circ$  to  $\approx 45^\circ$  ( $V_K \approx 60$  to  $30$  knots or  $31$  to  $15$  meters/sec); whereas, tuft-stall boundaries indicate a descent capability of  $-6^\circ$  and greater. Comparison of these descent boundaries obtained from the wind-tunnel results with boundaries obtained on a scaled free-flight model (also shown in fig. 37) shows good agreement when compared with the tuft-stall boundaries. Preliminary flights of the full-scale airplane indicate that the airplane can achieve appreciably higher descent angles than those predicted by the model on the basis of the initial flow separation. The flight-test results to date, however, are based on pilot reports of buffet. There is at present no indication of the amount of flow separation that would be required to produce the observed buffet.

Figure 38 illustrates the importance of flap-deflection angle on the descent capability. Note that for  $\delta_f = 40^\circ$ , the flight-path angle is essentially  $0^\circ$  in the 40-to-60-knot (21-to-31 m/s) speed range as compared with  $-6^\circ$  or more for  $\delta_f = 60^\circ$ .

The reduced descent capability in ground effect shown in figure 39 (although of no practical significance in the descent angle sense, because the airplane is so close to the ground) is indicative of the reduction in maximum lift coefficient and the change in drag coefficient observed when comparing the out-of-ground and in-ground effect data of figures 14 and 26. A comparison of the maximum lift coefficient out-of-ground and

in-ground effect for  $i_w = 40^\circ$  and  $\delta_f = 60^\circ$  at  $C_{T,s} \approx 0.82$  shows the maximum lift coefficient is reduced from about 2.0 to 1.65 for  $h/\bar{c} = 0.74$  or about 17 percent.

### Effect of Configuration Changes

Effect of propeller-blade pitch.- The results of figure 39 (obtained from figs. 22 and 23 and tuft pictures) show that reducing the propeller-blade pitch angle from  $12^\circ$  to  $8^\circ$  made tremendous improvement in the descent capability of the tilt-wing configuration especially at high wing-tilt angles. For example, for the high wing-tilt angle tested ( $i_w = 40^\circ$ ) with the fuselage level the descent angle was increased from  $-7^\circ$  to  $-17^\circ$ , and for the lower wing-tilt angle ( $i_w = 20^\circ$ ) it was increased from  $-5.5^\circ$  to  $-8.0^\circ$ .

Whether the aforementioned results obtained with small-scale propellers represent results that would be obtained with the full-scale propeller characteristics (induced flows, rotational effects, and so forth) on a full-scale airplane or are associated with model scale effects has not been determined. However, analysis and data obtained on propeller-driven configurations with a wing immersed in the propeller slipstream (refs. 16 to 18) have indicated that the direction of propeller rotation, propeller-blade angle, and propeller-power-absorption characteristics could be expected to have an effect on the aerodynamic characteristics of such configurations.

A simplified analysis, based on propeller momentum and power considerations, indicates that upwash and downwash at the wing leading edge due to the up-going and down-going blades is proportional to the power-to-thrust-coefficient ratio as indicated by the following equation:

$$\Delta\alpha = f \left[ \frac{C_P \frac{8}{3} v}{C_T \pi} \right] \frac{1}{V + 2v}$$

This change in local angle of attack indicates that a propeller having a relatively low pitch angle would absorb less power per unit thrust than would a large blade angle, and, as the equation indicates, the upwash behind the blade would be reduced, thereby reducing the local wing-stall angle ( $\Delta\alpha$ ). A reduction in local wing stall should improve the descent capability.

As mentioned in the section entitled "Tests," the thrust of all propellers was matched to reduce asymmetries of flow across the wing span; however, upon inspection of the individual propeller thrust coefficients presented in figures 22, 23, and 26, it is evident that the thrust match did not hold constant for all wing-flap configurations tested. In view of the apparent importance of propeller-blade pitch angle previously discussed, it should be noted that this mismatch of thrust coefficient seems to be of small consequence as seen by comparing the stall patterns across the wing span (figs. 29 to 33),

although the variation from the nominal value indicates a propeller-blade pitch-angle change as large as  $1.4^\circ$  in some cases.

Slats.- In anticipation of stall problems, the present design included leading-edge slats ( $S_1$ ) behind the up-going propeller blades for the configurations with the flaps deflected. During the present investigation an attempt was made to improve the stall characteristics between nacelles by increasing the span of the inboard slats. ( $S_2$ , see fig. 8.) The large-span leading-edge slats gave a slight improvement in wing stall for  $i_w = 20^\circ$  at the lower thrust coefficients. (See figs. 24 and 31.) This improved flow increased the descent capability for  $i_w = 20^\circ$  from  $-6.5^\circ$  to about  $-8.2^\circ$  (fig. 39).

Leading-edge chord-extension group.- Another device investigated to improve the stall characteristics was a 10-percent-extended chord leading edge with the nose drooped  $10^\circ$  (fig. 9). Comparison of figure 25 with figure 14(e) shows that the chord extension combined with leading-edge droop for  $i_w = 40^\circ$  and  $\delta_f = 60^\circ$  reduced the abruptness and delayed the stall. The drooped-chord extension increased the descent capability at  $i_w = 40^\circ$  from  $-6.5^\circ$  to about  $-15.0^\circ$ . (See fig. 39.)

#### CONCLUDING REMARKS

An investigation of a four-propeller tilt-wing V/STOL transport configuration at transition speeds has indicated the following conclusions.

The descent capability for the model is low but is considerably better at  $60^\circ$  flap deflection than at  $40^\circ$  using a propeller-blade pitch angle of  $12^\circ$ . The results show that the airplane would have a descent capability of approximately  $6^\circ$  based on stall indicated by tuft studies for the flap deflected  $60^\circ$ . Descent boundaries obtained from wind-tunnel tuft-stall values correlated well with boundaries obtained on a free-flight model. Preliminary results of flight tests of the full-scale airplane indicate that the airplane achieves appreciably higher descent angles (based on buffet) than indicated by model flow separation. At present there is no correlation between the degree of model flow separation and airplane buffet.

Considerable improvement in descent capability was obtained by drooping and extending the wing chord or by using a lower propeller-blade pitch angle of  $8^\circ$ .

Langley Research Center,  
National Aeronautics and Space Administration,  
Langley Station, Hampton, Va., November 3, 1965.

APPENDIX

CONVERSION TO INTERNATIONAL SYSTEM OF UNITS (SI)

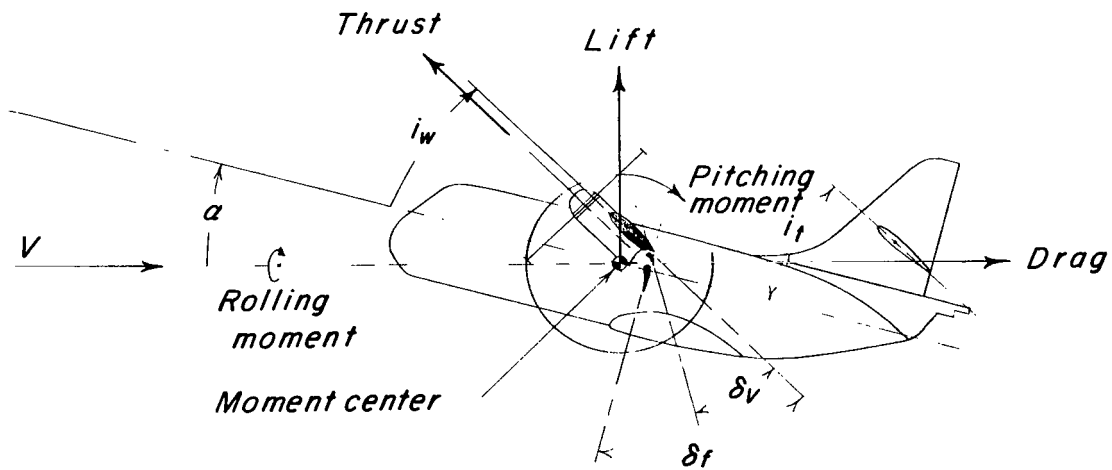
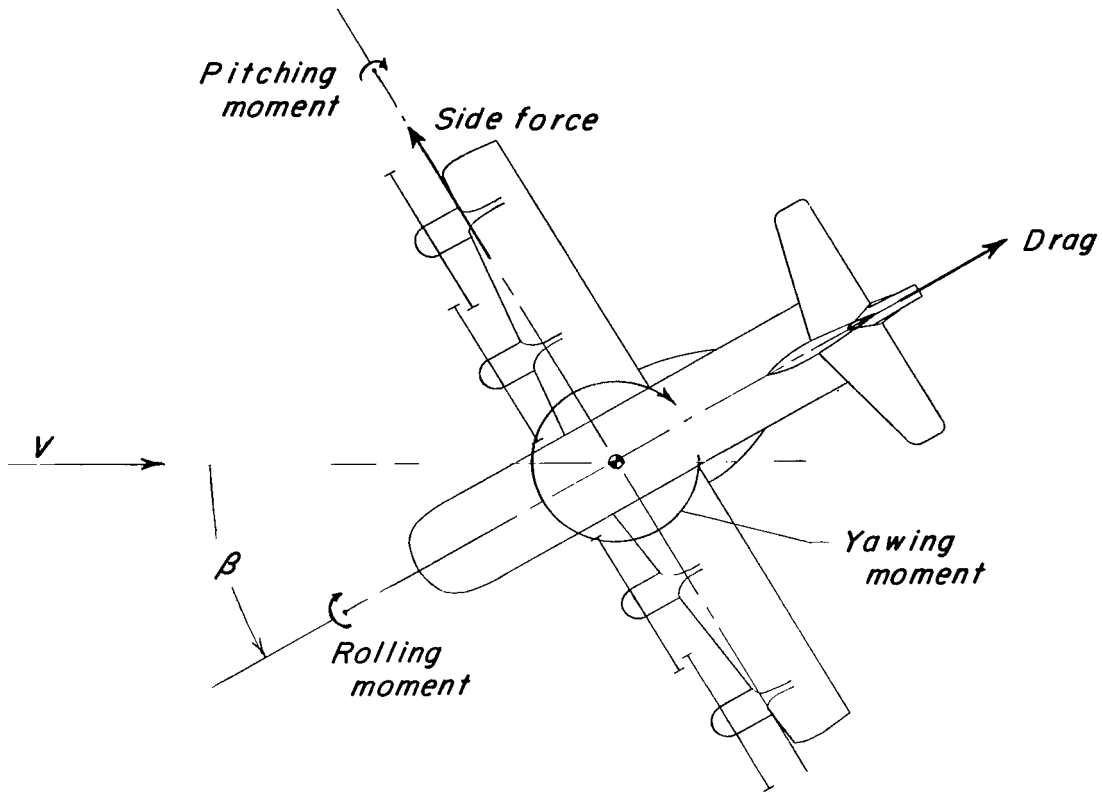
Physical quantity	U.S. Customary Unit	Conversion factor (*)	SI Unit
Area	sq inch	6.4516	square meters ( $m^2$ )
	sq foot	0.0929	square meters ( $m^2$ )
Density	slugs/cu foot	515.379	kilogram/cubic meter ( $kg/m^3$ )
Force	lbf	4.4482	newtons (N)
Length	inch	2.54	centimeters (cm)
	inch	0.0254	meters (m)
	foot	0.3048	meters (m)
Moment	foot-pound	1.3558	meter-newton (m-N)
Pressure	lb/sq ft	47.8803	newtons/sq meter ( $N/m^2$ )
Velocity	mi/hr (U.S. Statute)	0.44704	meters/second (m/s)
	knot (Int.)	0.51444	meters/second (m/s)

\* Multiply value given in U.S. Customary Unit by conversion factor to obtain equivalent value in SI Unit.

## REFERENCES

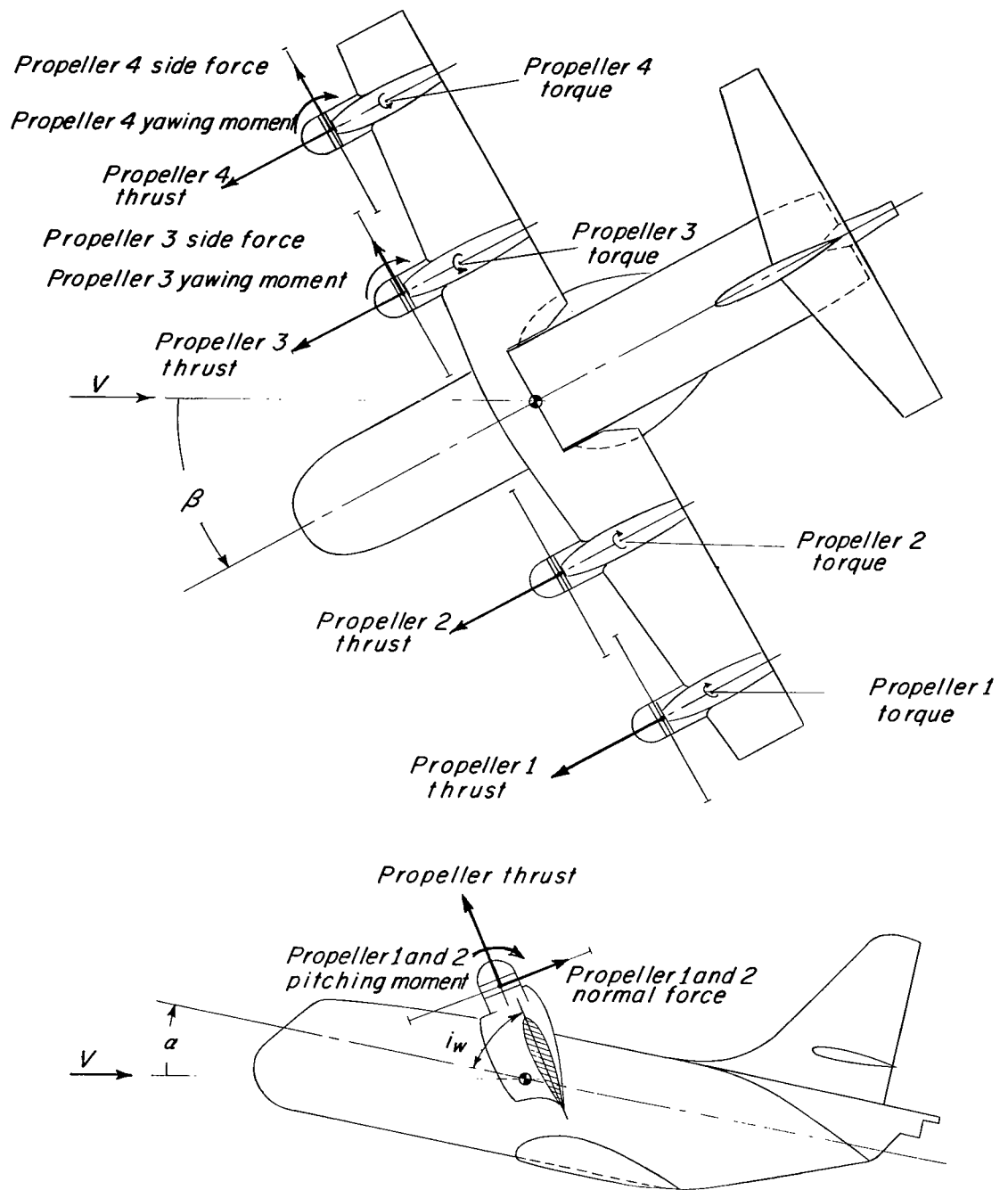
1. Kuhn, Richard E.; and Draper, John W.: Investigation of the Aerodynamic Characteristics of a Model Wing-Propeller Combination and of the Wing and Propeller Separately at Angles of Attack up to  $90^{\circ}$ . NACA Rept. 1263, 1956. (Supersedes NACA TN 3304 by Draper and Kuhn.)
2. Kuhn, Richard E.; and Hayes, William C., Jr.: Wind-Tunnel Investigation of Longitudinal Aerodynamic Characteristics of Three Propeller-Driven VTOL Configurations in the Transition Speed Range, Including Effects of Ground Proximity. NASA TN D-55, 1960.
3. Newsom, William A., Jr.; and Tosti, Louis P.: Force-Test Investigation of the Stability and Control Characteristics of a 1/4-Scale Model of a Tilt-Wing Vertical-Take-Off-and-Landing Aircraft. NASA MEMO 11-3-58L, 1959.
4. Tosti, Louis P.: Flight Investigation of the Stability and Control Characteristics of a 1/4-Scale Model of a Tilt-Wing Vertical-Take-Off-and-Landing Aircraft. NASA MEMO 11-4-58L, 1959.
5. Tosti, Louis P.: Aerodynamic Characteristics of a 1/4-Scale Model of a Tilt-Wing VTOL Aircraft at High Angles of Wing Incidence. NASA TN D-390, 1960.
6. Tosti, Louis P.: Longitudinal Stability and Control of a Tilt-Wing VTOL Aircraft Model With Rigid and Flapping Propeller Blades. NASA TN D-1365, 1962.
7. Newsom, William A., Jr.; and Tosti, Louis P.: Slipstream Flow Around Several Tilt-Wing VTOL Aircraft Models Operating Near the Ground. NASA TN D-1382, 1962.
8. Spreemann, Kenneth P.: Investigation of a Semispan Tilting-Propeller Configuration and Effects of Ratio of Wing Chord to Propeller Diameter on Several Small-Chord Tilting-Wing Configurations at Transonic Speeds. NASA TN D-1815, 1963.
9. Newsom, William A., Jr.: Effect of Ground Proximity on the Aerodynamic Characteristics of a Four-Engine Vertical-Take-Off-and-Landing Transport-Airplane Model With Tilting Wing and Propellers. NACA TN 4124, 1957.
10. Pegg, Robert J.: Summary of Flight-Test Results of the VZ-2 Tilt-Wing Aircraft. NASA TN D-989, 1962.
11. Mitchell, Robert G.: Full-Scale Wind-Tunnel Test of the VZ-2 VTOL Airplane With Particular Reference to the Wing Stall Phenomena. NASA TN D-2013, 1963.
12. Schade, Robert O.: Ground Interference Effects. NASA TN D-727, 1961.

13. Tosti, Louis P.: Force-Test Investigation of the Stability and Control Characteristics of a 1/8-Scale Model of a Tilt-Wing Vertical-Take-Off-and-Landing Airplane. NASA TN D-44, 1960.
14. Schade, Robert O.; and Kirby, Robert H.: Effect of Wing Stalling in Transition on a 1/4-Scale Model of the VZ-2 Aircraft. NASA TN D-2381, 1964.
15. Kirby, Robert H.; Schade, Robert O.; and Tosti, Louis P.: Force-Test Investigation of a 1/4-Scale Model of the Modified VZ-2 Aircraft. NASA TN D-2382, 1964.
16. Kirby, Robert H.: Aerodynamic Characteristics of Propeller-Driven VTOL Aircraft. NASA TN D-730, 1961.
17. Newsom, William A., Jr.; and Kirby, Robert H.: Flight Investigation of Stability and Control Characteristics of a 1/9-Scale Model of a Four-Propeller Tilt-Wing V/STOL Transport. NASA TN D-2443, 1964.
18. Deckert, Wallace H.; Page, V. Robert; and Dickinson, Stanley O.: Large-Scale Wind-Tunnel Tests of Descent Performance of an Airplane Model With a Tilt Wing and Differential Propeller Thrust. NASA TN D-1857, 1964.
19. Mechtly, E. A.: The International System of Units - Physical Constants and Conversion Factors. NASA SP-7012, 1964.
20. Staff of Powered-Lift Aerodynamics Section, NASA Langley Res. Center: Wall Effects and Scale Effects in V/STOL Model Testing. AIAA Aerodynamic Testing Conf., Mar. 1964.
21. Heyson, Harry H.: Linearized Theory of Wind-Tunnel Jet-Boundary Corrections and Ground Effect for VTOL-STOL Aircraft. NASA TR R-124, 1962.



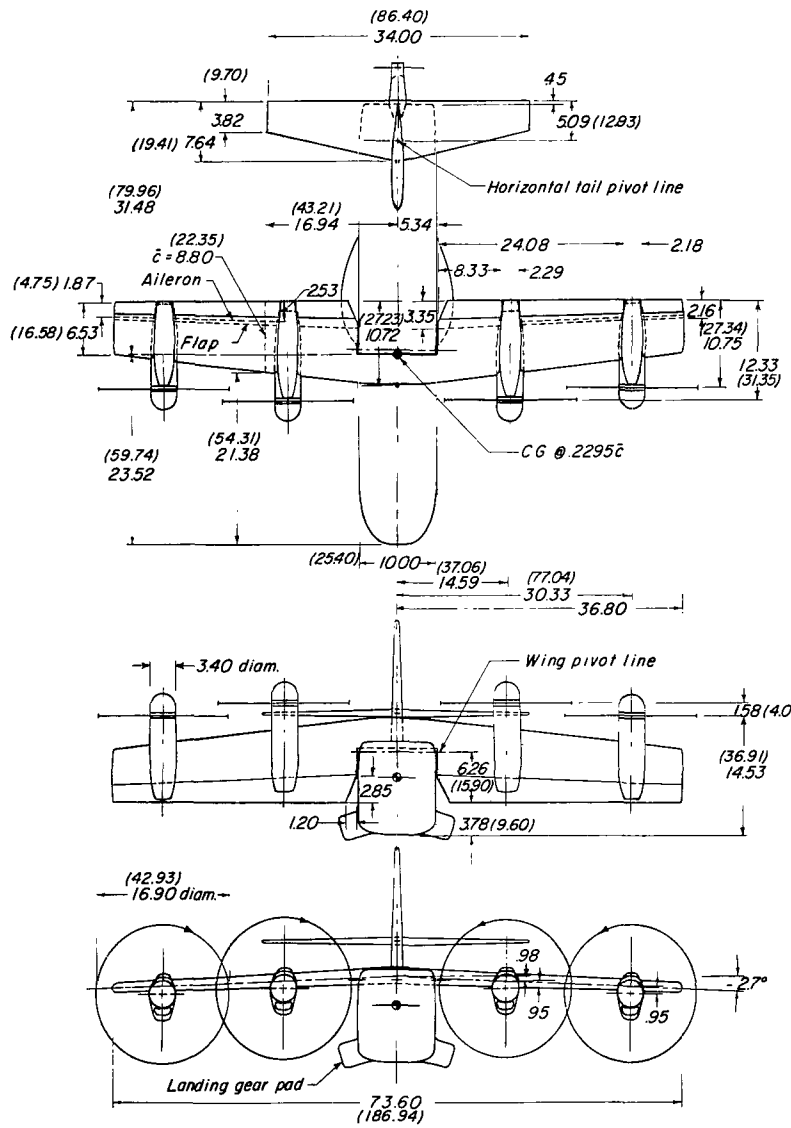
(a) Complete model.

Figure 1.- System of axes. Positive directions of forces, moments, and angles are indicated by arrows.



(b) Propellers.

Figure 1.- Concluded.



*Geometric Characteristics*

<i>Wing</i>	
Area, sq ft (sq meters)	4.42 (0.41)
Mean geometric chord, inches (cm)	8.80 (22.34)
Span, inches (cm)	73.60 (186.94)
Dihedral, deg	-2.70
Airfoil	NACA 63-318
<i>Horizontal tail</i>	
Area, sq ft (sq meter)	1.33 (0.12)
Airfoil	NACA 0015
<i>Vertical tail</i>	
Area, sq ft (sq meter)	0.86 (0.08)
Airfoil	
Root	NACA 0018
At 28.6% span	NACA 0012
Tip	NACA 0012
<i>Propeller</i>	
Disk, sq ft (sq meter)	1.56 (0.14)
Diameter, ft (meter)	1.41 (0.43)

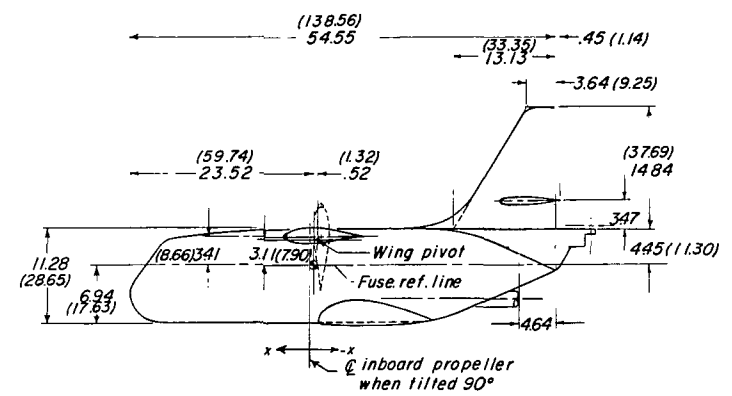


Figure 2.- Geometric characteristics of a 1/11-scale four-propeller tilt-wing VTOL model. Dimensions are given first in inches and parenthetically in centimeters; because of space limitations conversion to the International System of Units is not given for all dimensions.

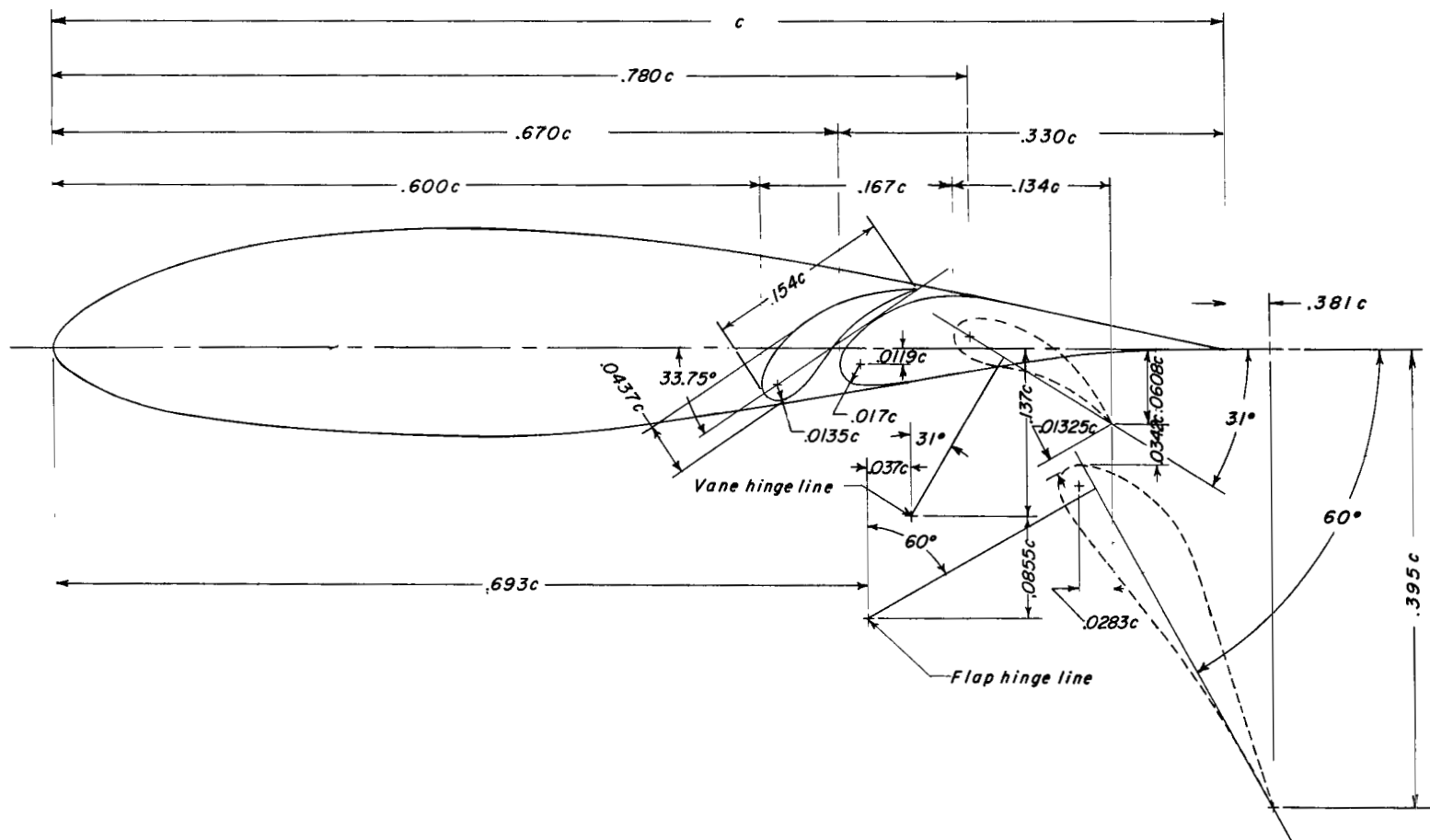


Figure 3.- Details of the flap system of the 1/11-scale tilt-wing VTOL model.

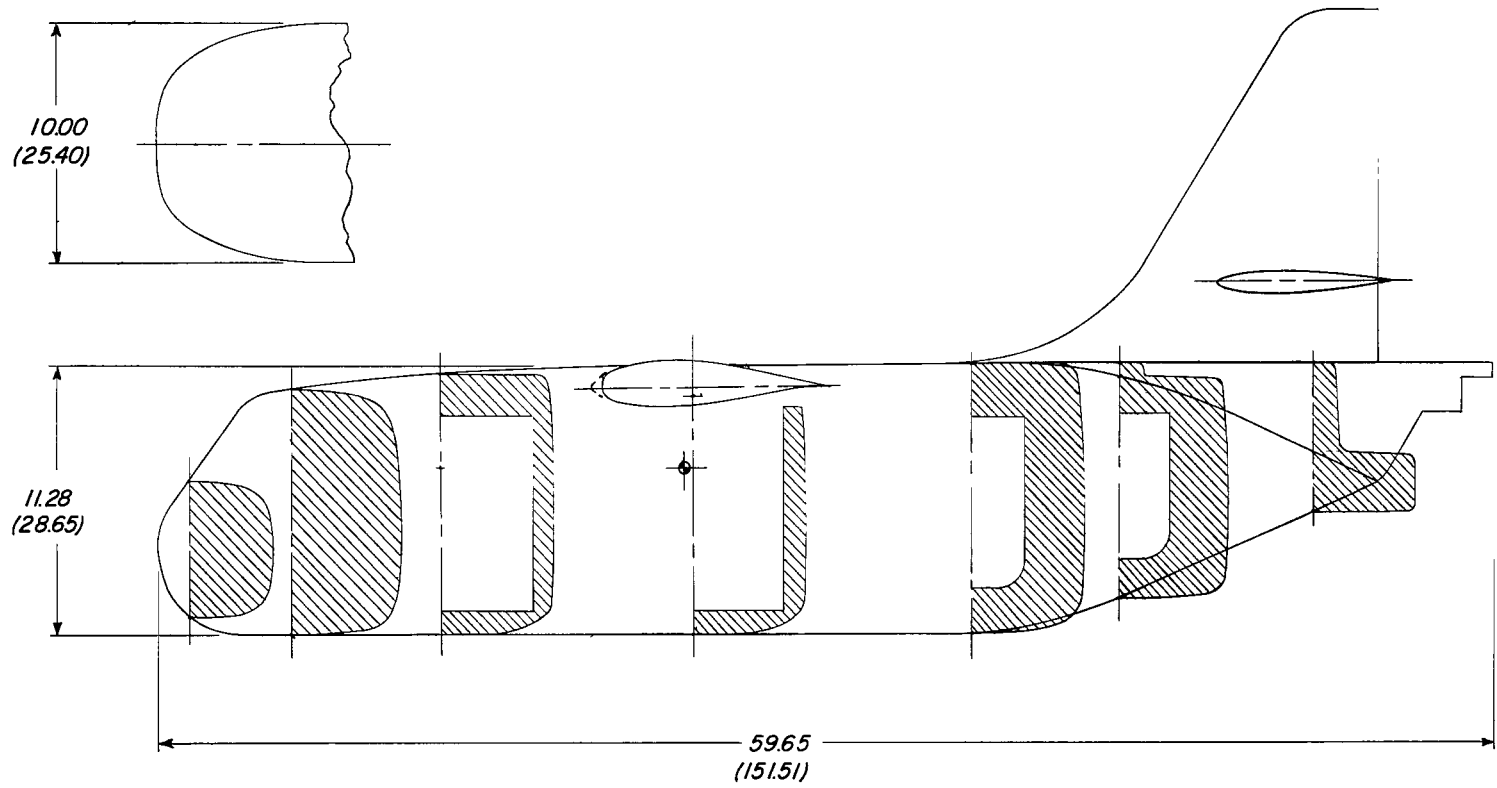


Figure 4.- Fuselage cross sections of a 1/11-scale tilt-wing VTOL model. Dimensions are given first in inches and parenthetically in centimeters.

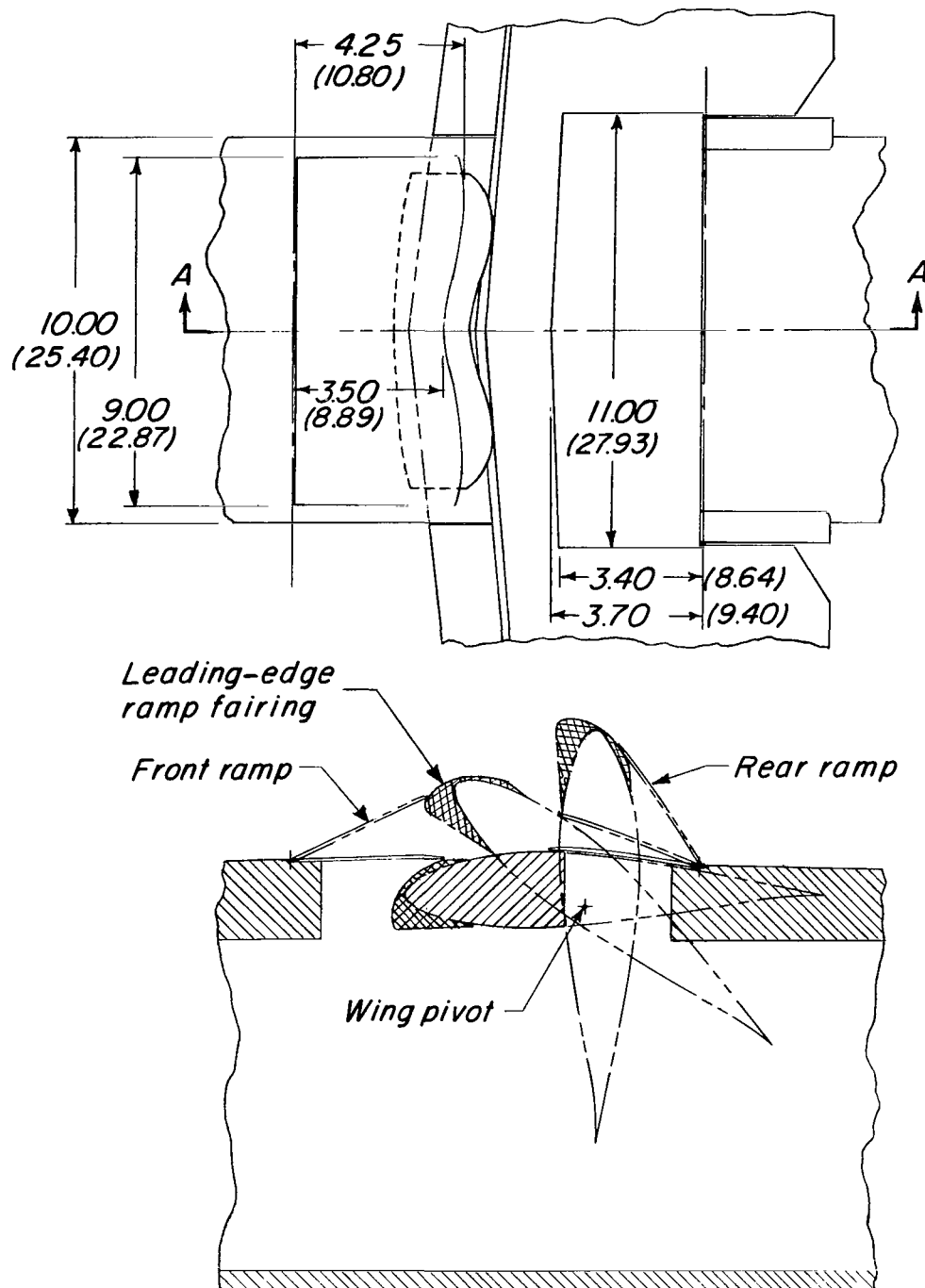


Figure 5.- Wing-fuselage ramps of the 1/11-scale tilt-wing VTOL model. Dimensions are given first in inches and parenthetically in centimeters.

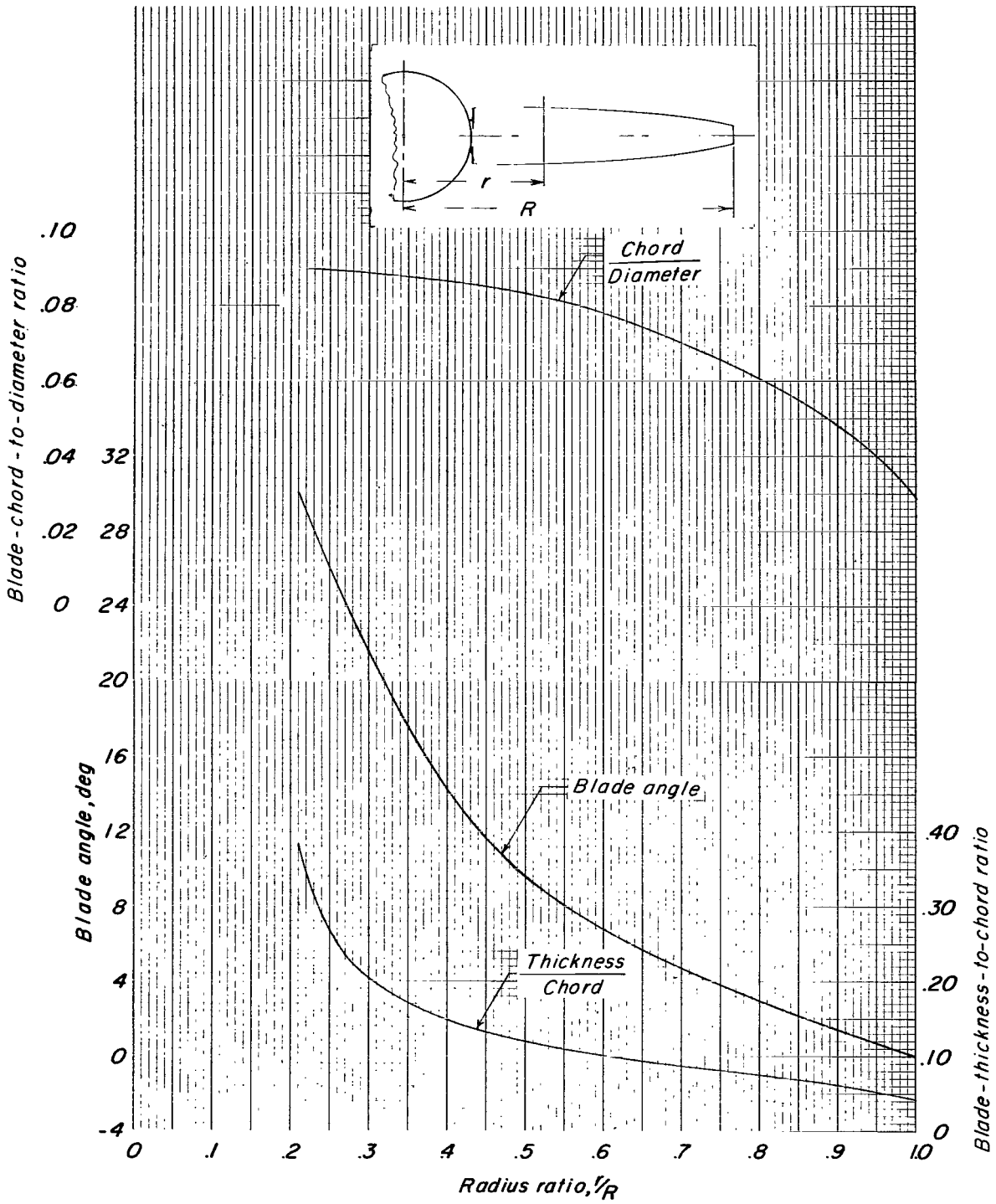
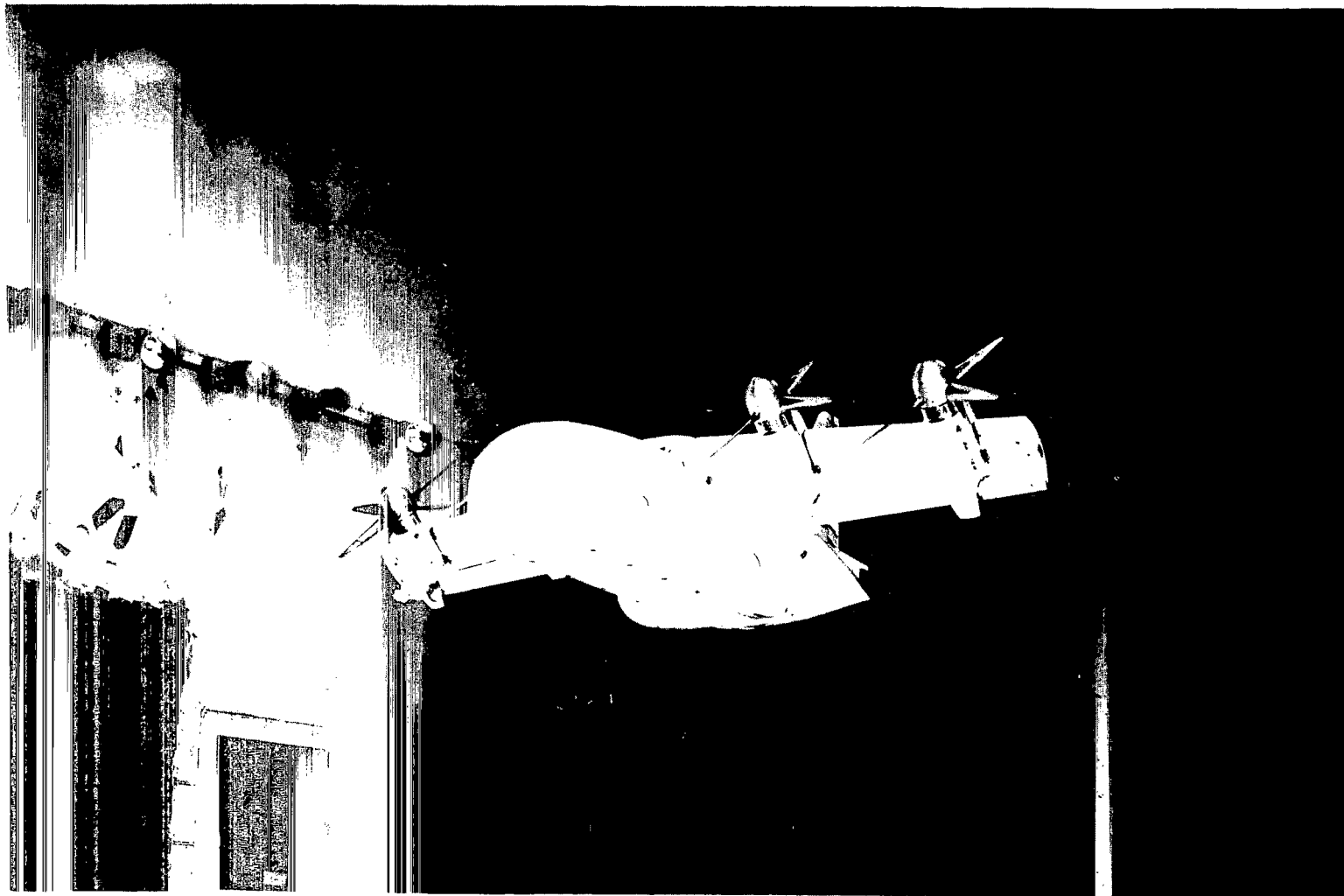


Figure 6.- Geometric characteristics of propeller blade of a 1/11-scale tilt-wing VTOL model.



(a) Model out of ground effect.

L-64-9853

Figure 7.- Photographs of model in 17-foot test section of the Langley 300-MPH 7- by 10-foot tunnel.



(b) Model over fixed ground board.

L-65-7961

Figure 7.- Concluded.

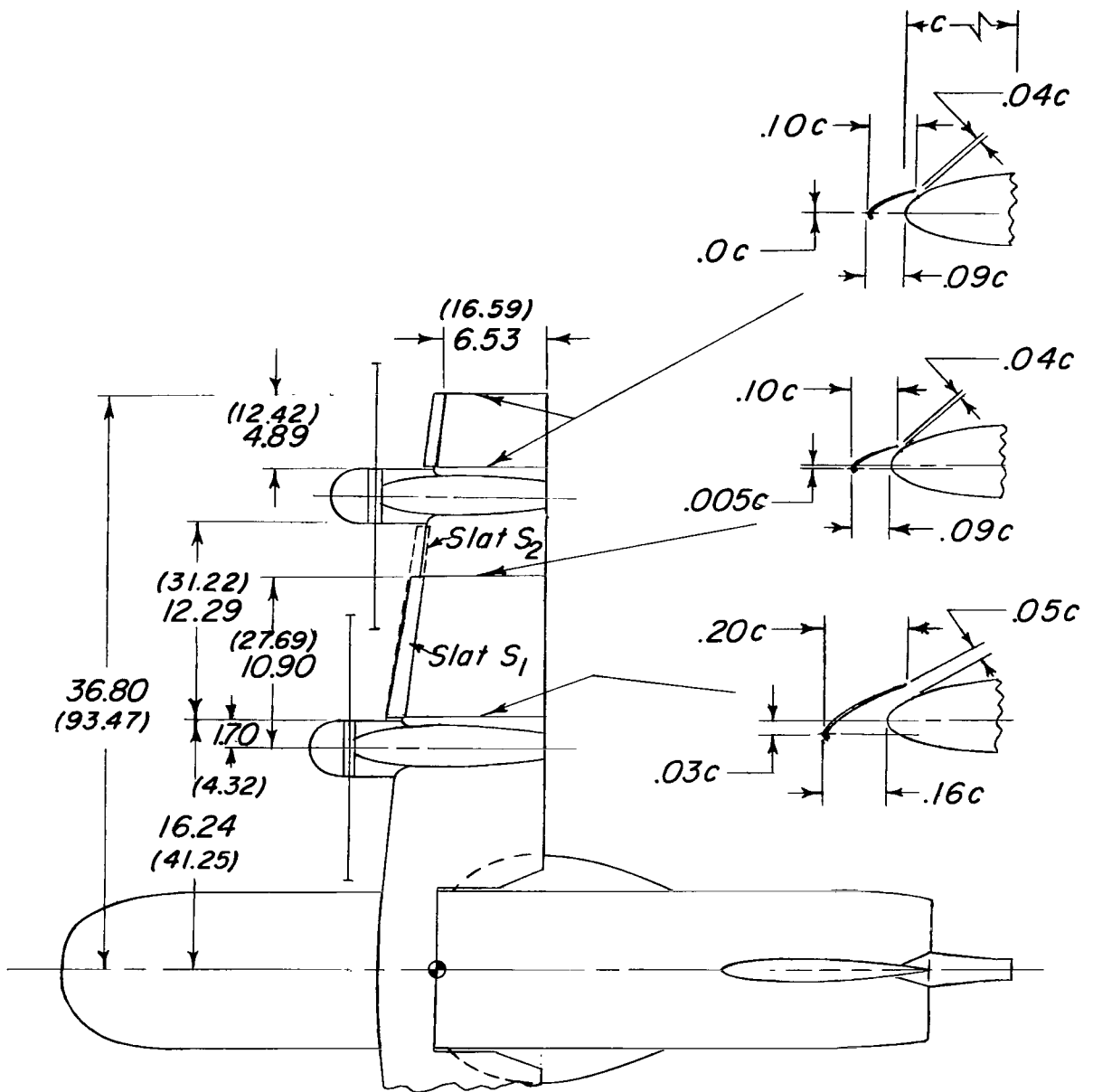


Figure 8.- Details of wing leading-edge slats of 1/11-scale tilt-wing VTOL model. Dimensions are given first in inches and parenthetically in centimeters.

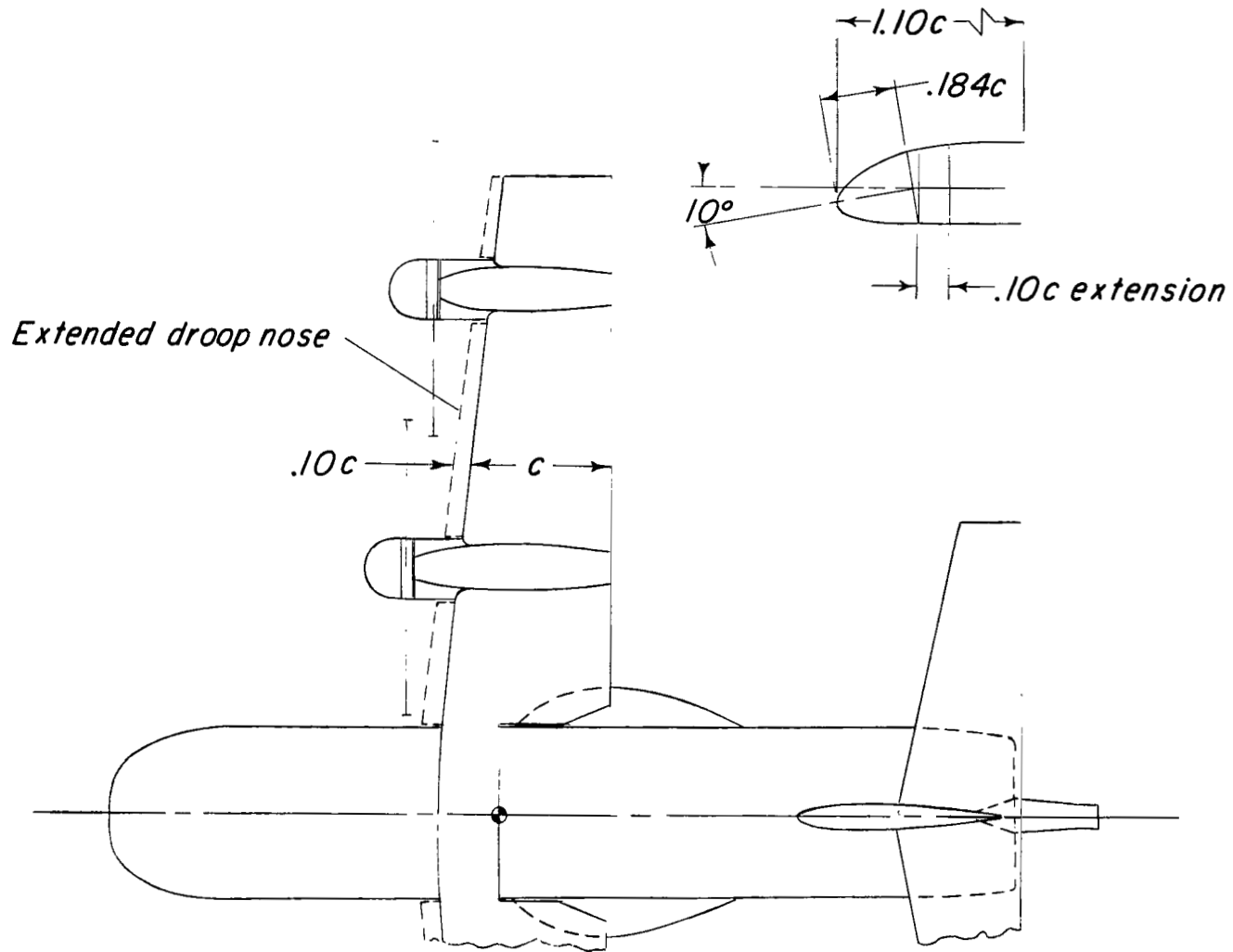


Figure 9.- Details of extended chord, drooped nose of 1/11-scale tilt-wing VTOL model.

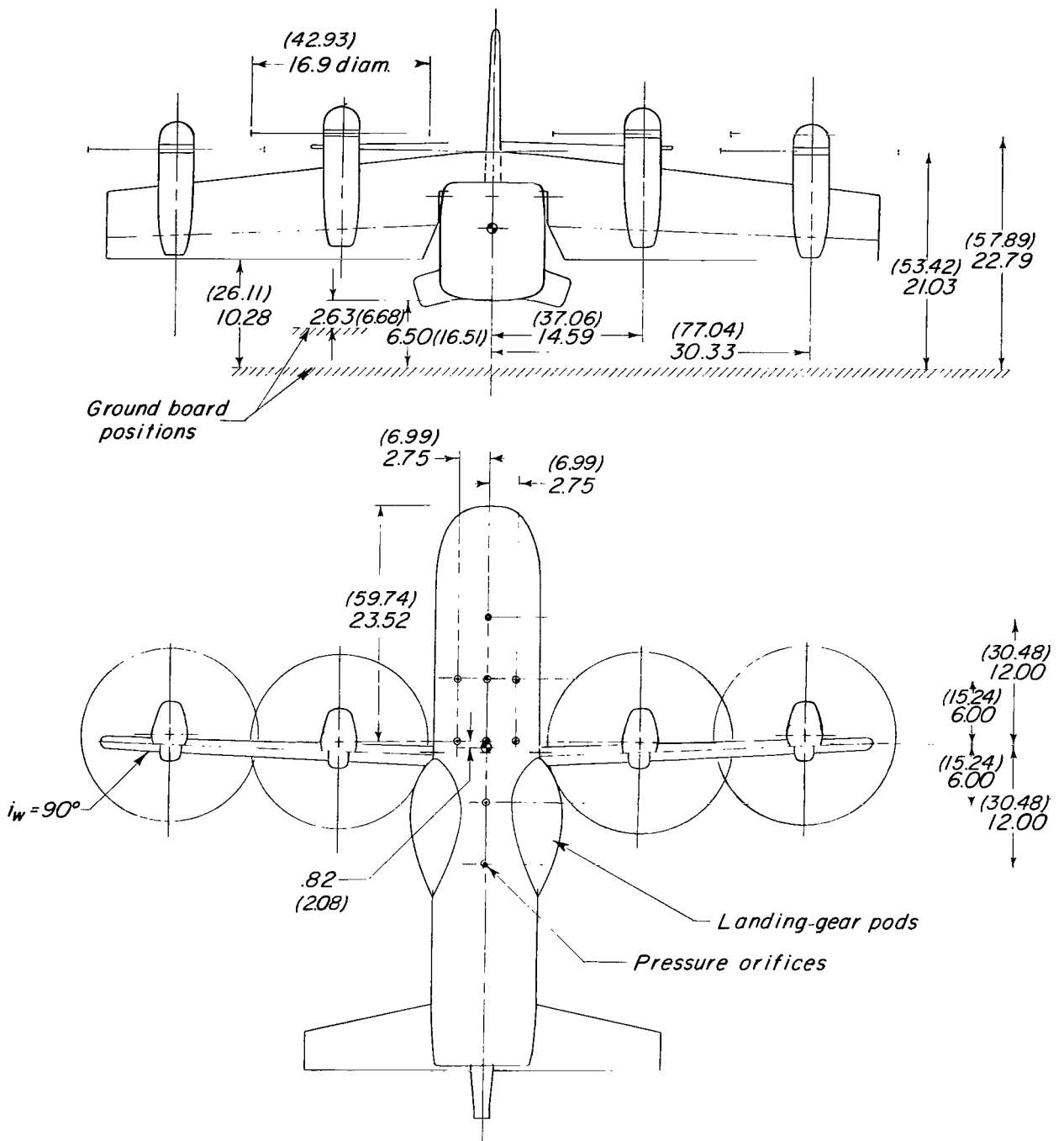


Figure 10.- Location of pressure orifices on fuselage bottom of 1/11-scale tilt-wing VTOL model. Dimensions are given first in inches and parenthetically in centimeters.

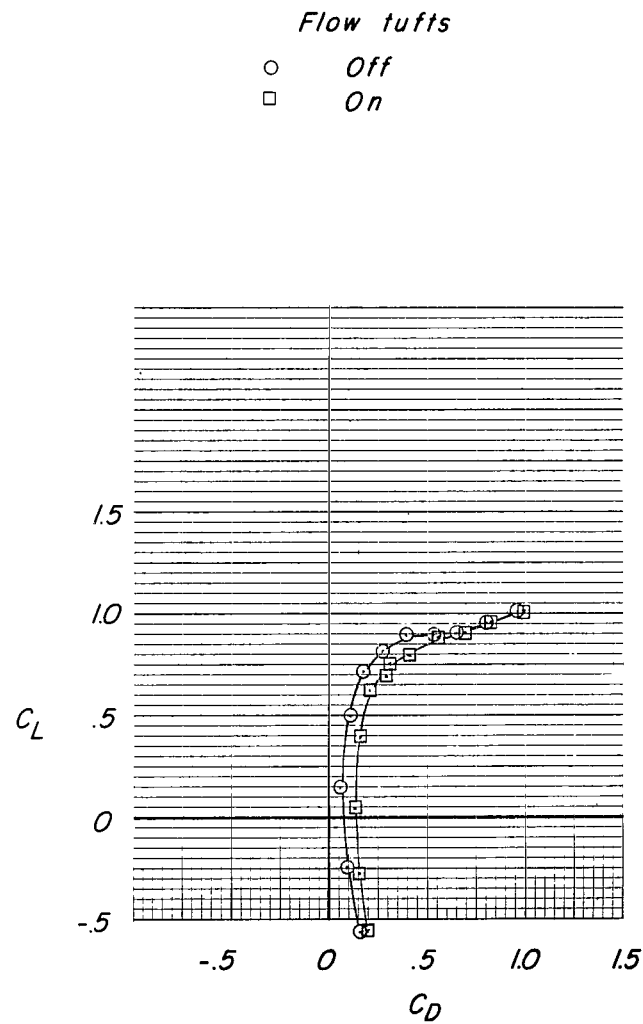
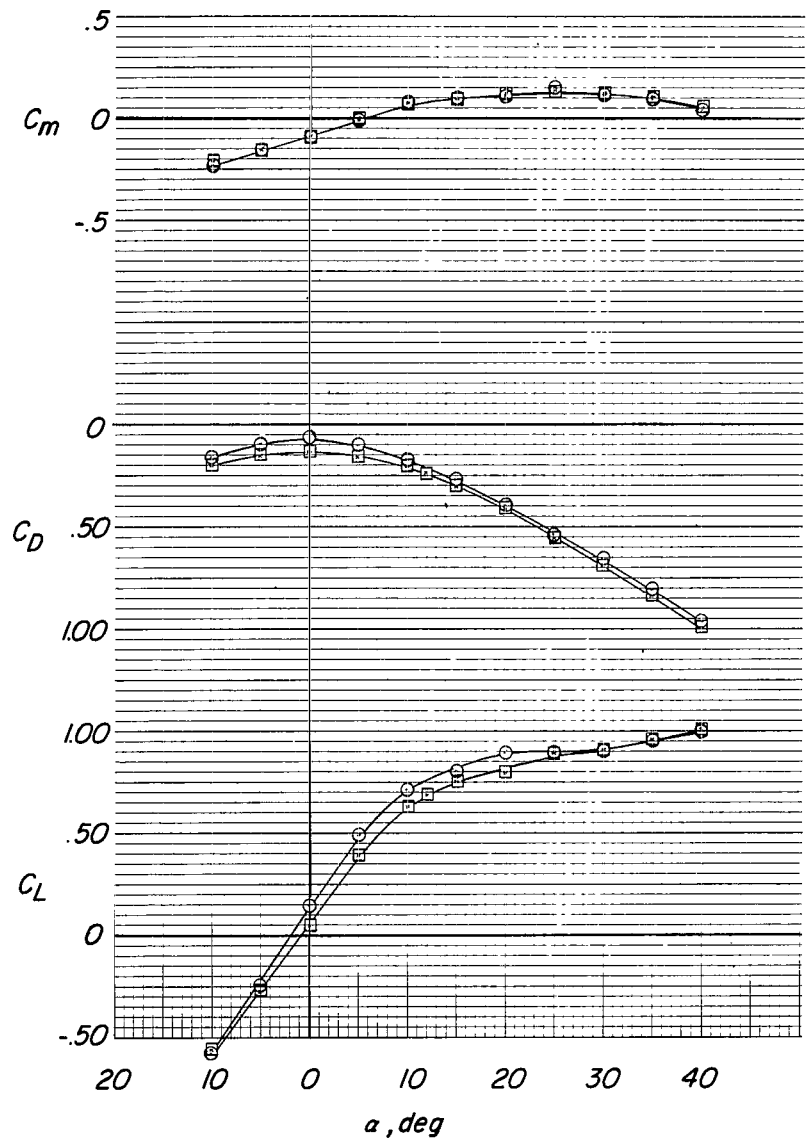


Figure 11.- Comparison of aerodynamic characteristics of tilt-wing VTOL model with and without tufts. (See photo, fig. 7.)  $i_w = 0^\circ$ ;  $\delta_f = 0^\circ$ ; tail-off; propellers off;  $h/\bar{c} = \infty$ .

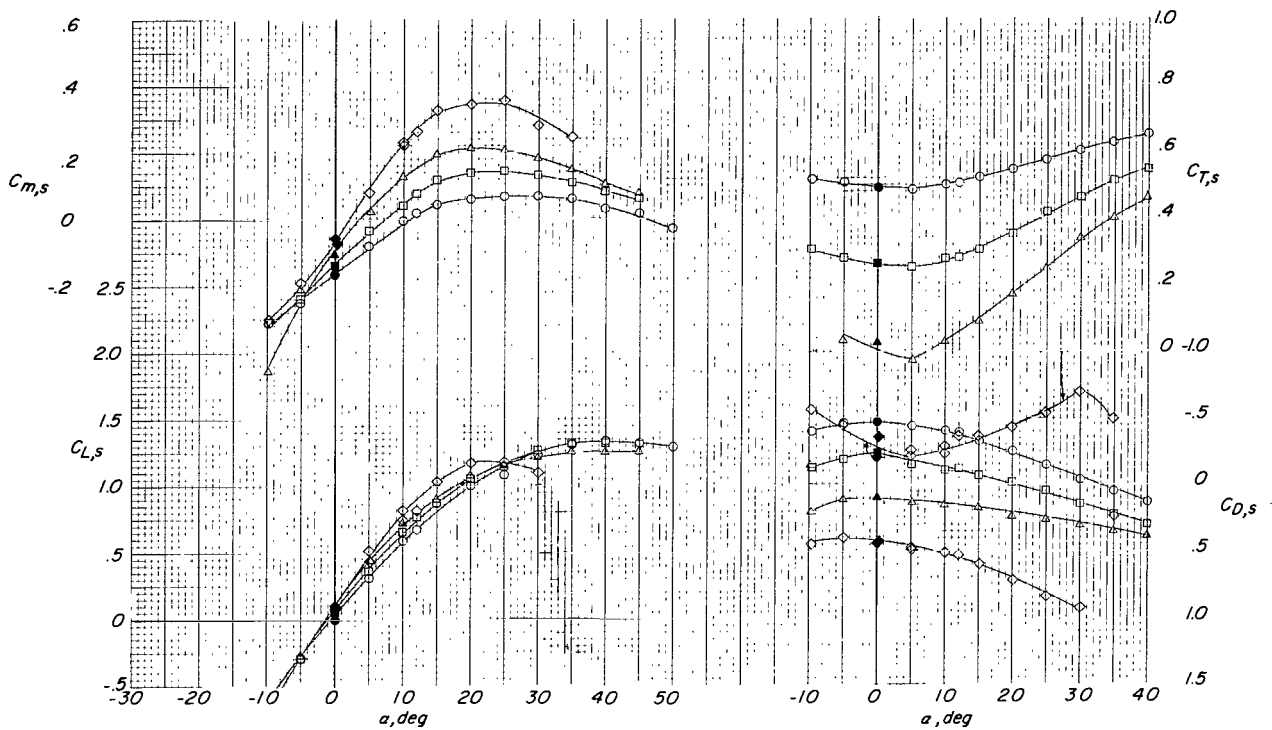
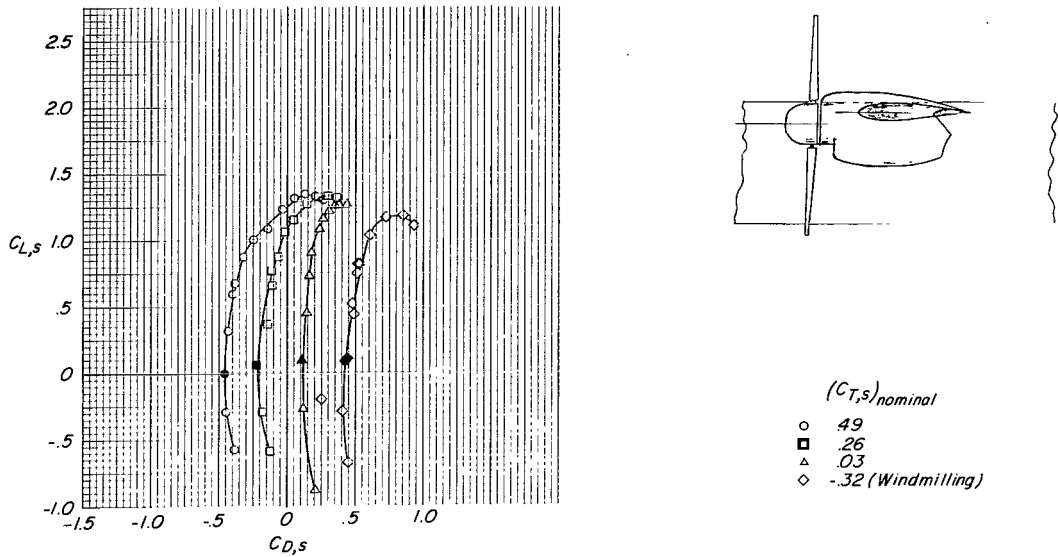
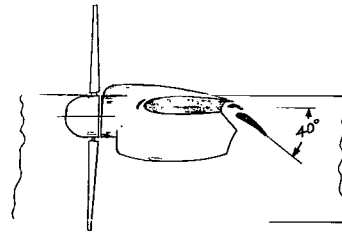
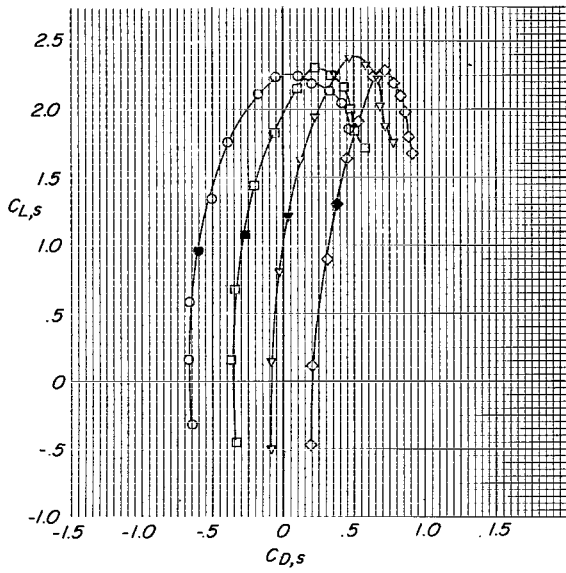
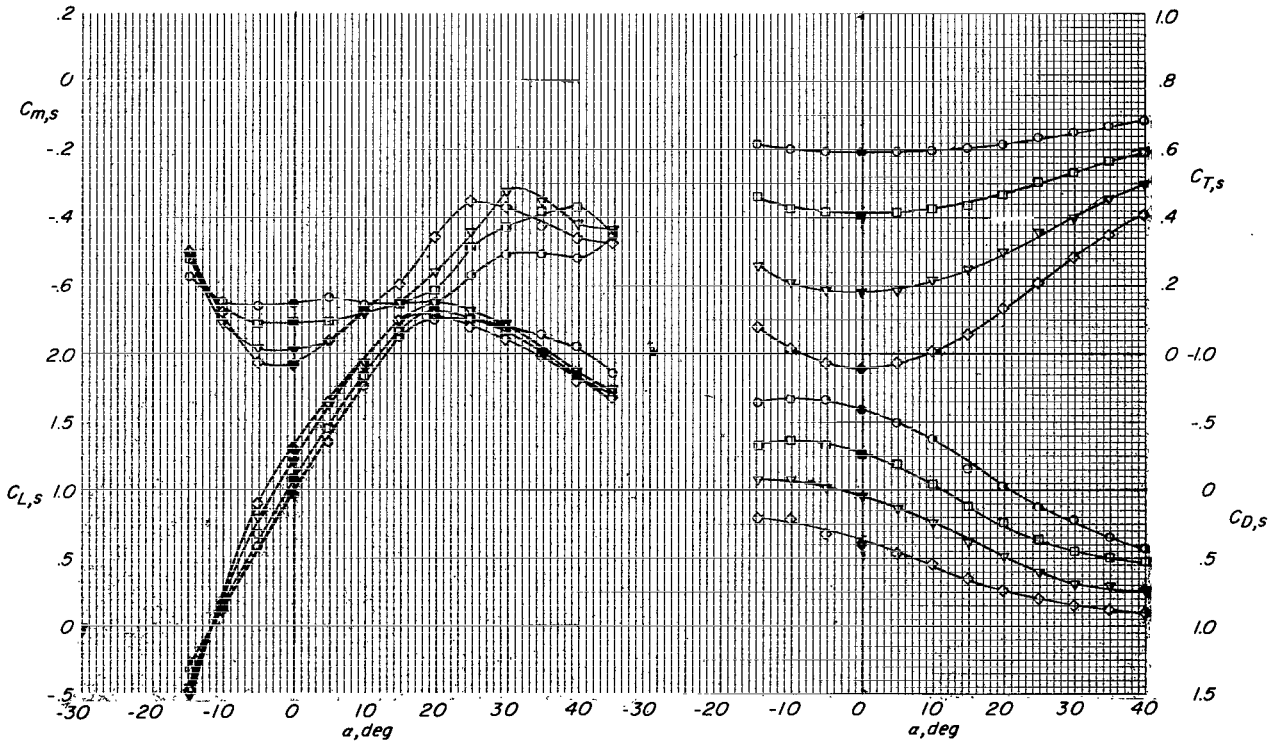


Figure 12.- Aerodynamic characteristics of tilt-wing VTOL model for zero wing incidence at various nominal thrust coefficients.  $i_t = \text{off}$ ; slat off;  $\beta_{.75R} = 12^\circ$ ; 7000 rpm;  $h/\bar{c} = \infty$ ;  $\delta_f = 0^\circ$ .

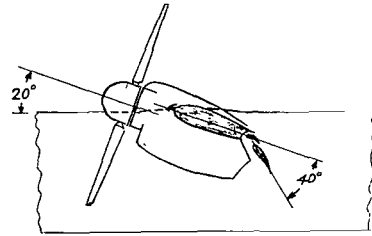
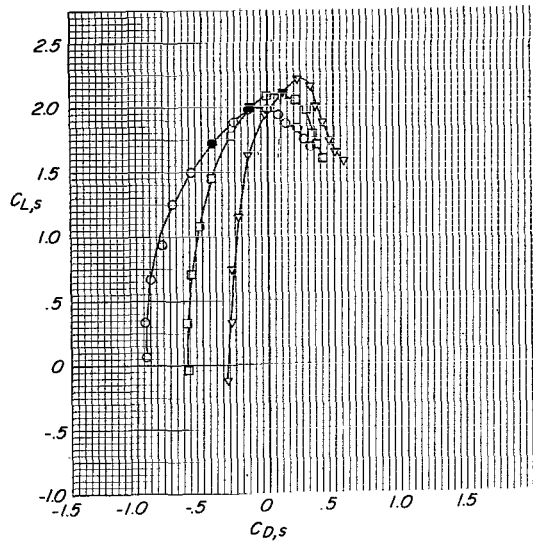


- $(C_{T,s})_{nominal}$
- .59
  - .41
  - ▽ .18
  - ◇ -.04



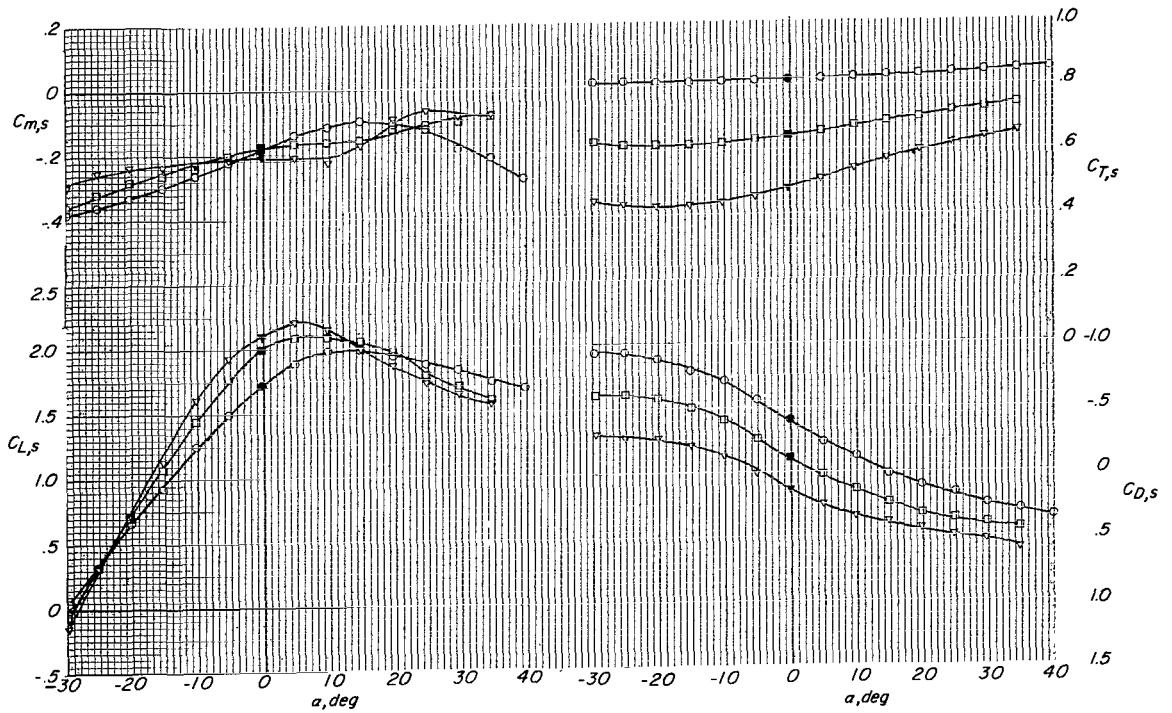
(a)  $i_w = 0^\circ$ .

Figure 13.- Aerodynamic characteristics of tilt-wing VTOL model for several wing incidence angles at various nominal thrust coefficients.  $i_t = 20^\circ$ ;  $S_1$  slat;  $\beta_{.75R} = 12^\circ$ ; 7000 rpm;  $h/\bar{c} = \infty$ ;  $\delta_f = 40^\circ$ .



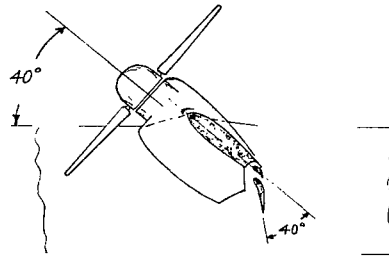
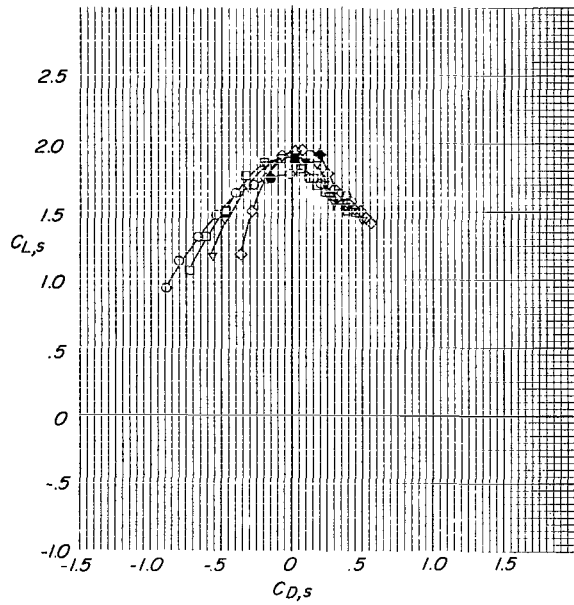
$(C_{T,s})_{nominal}$

- .82
- .64
- ▽ .48

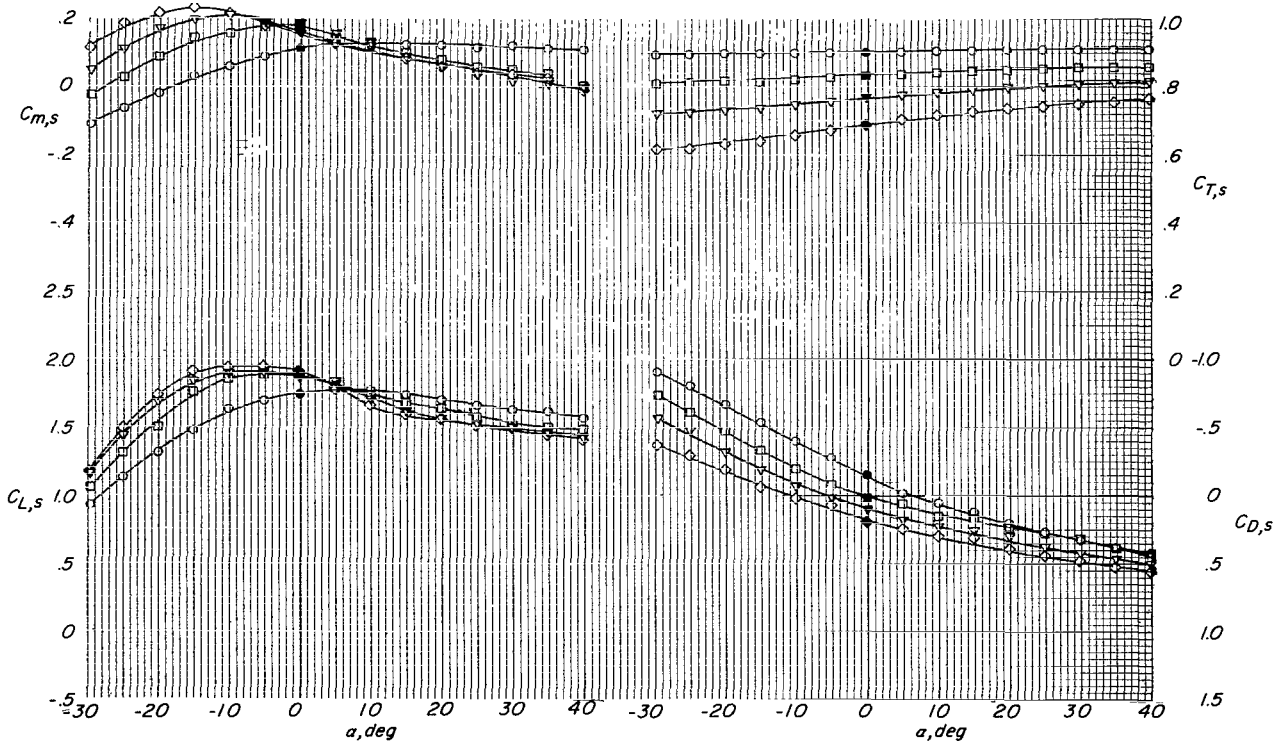


(b)  $i_w = 20^\circ$ .

Figure 13.- Continued.

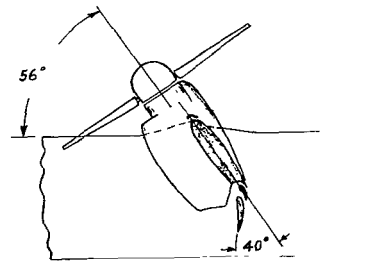
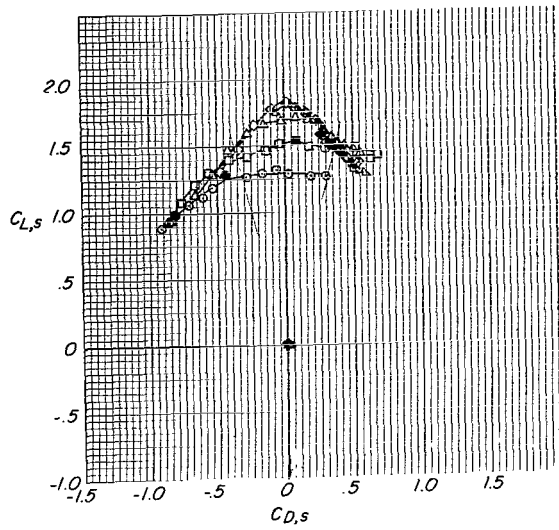


- $(C_{T,s})_{nominal}$
- .90
  - .84
  - ▽ .77
  - ◇ .69

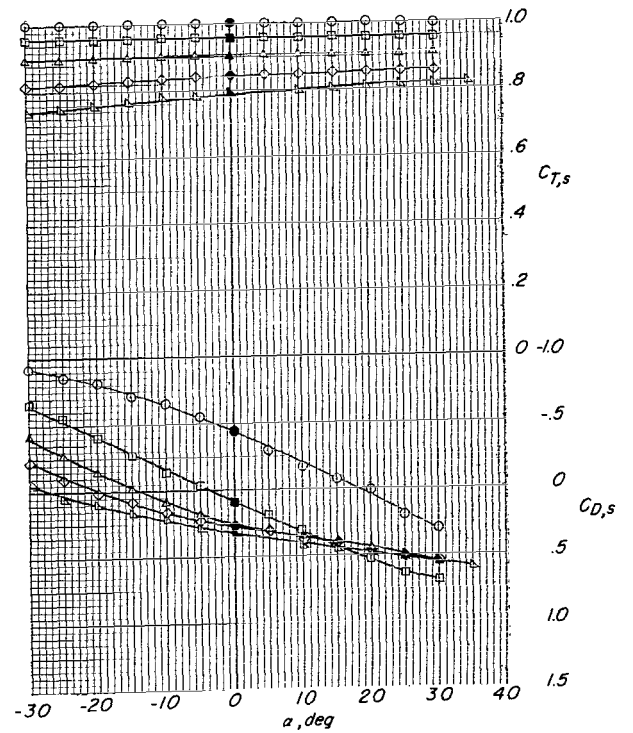
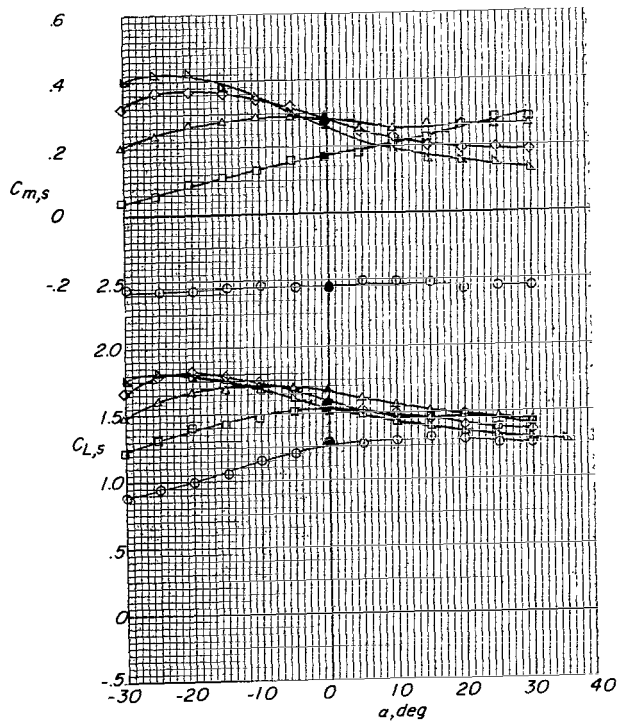


(c)  $i_w = 40^\circ$ .

Figure 13.- Continued.

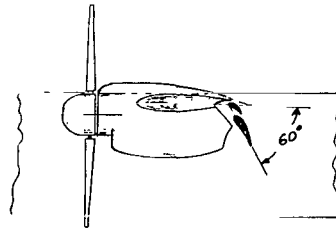
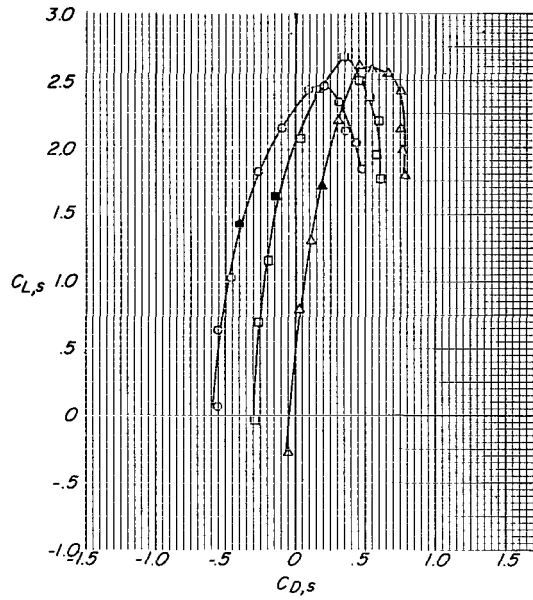


- $(C_{T,s})_{nominal}$
- 1.00
  - .96
  - △ .90
  - ◇ .84
  - ▽ .79



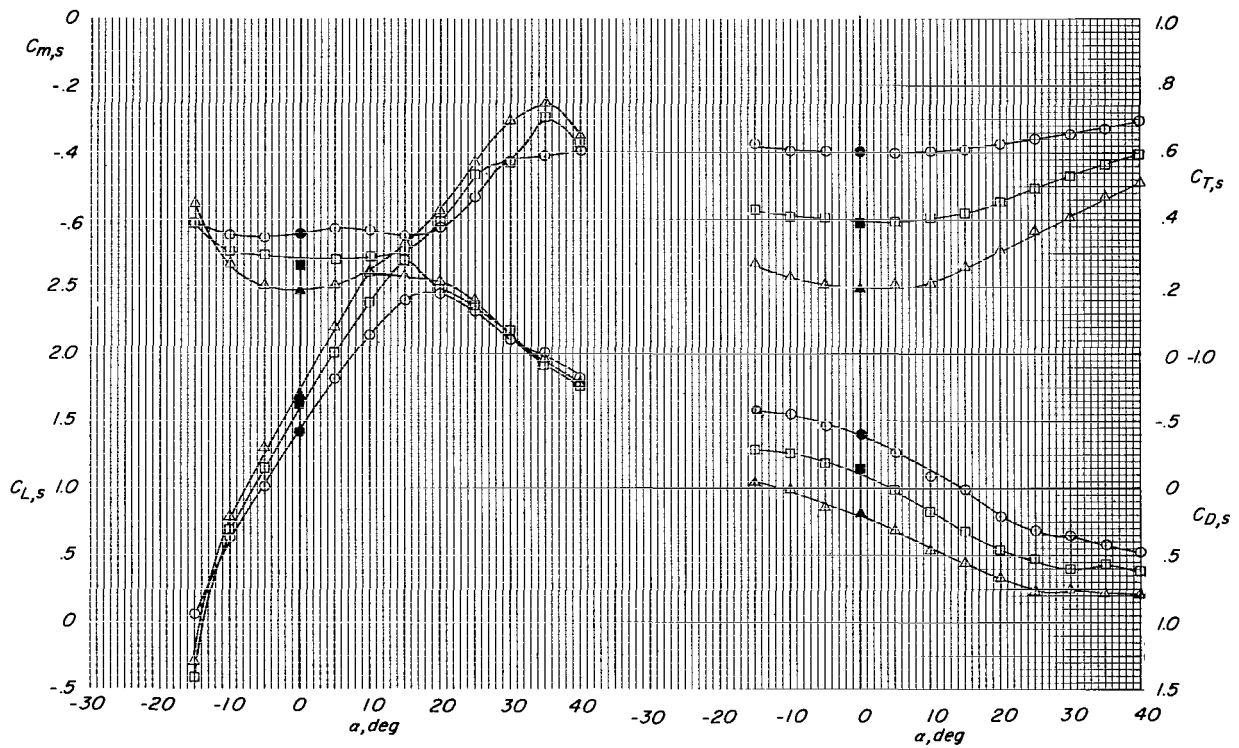
(d)  $i_w = 56^\circ$ .

Figure 13.- Concluded.



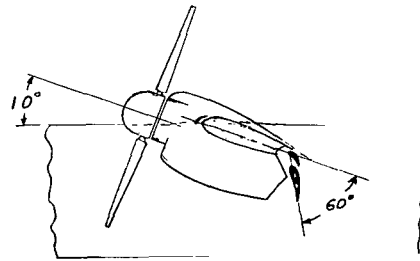
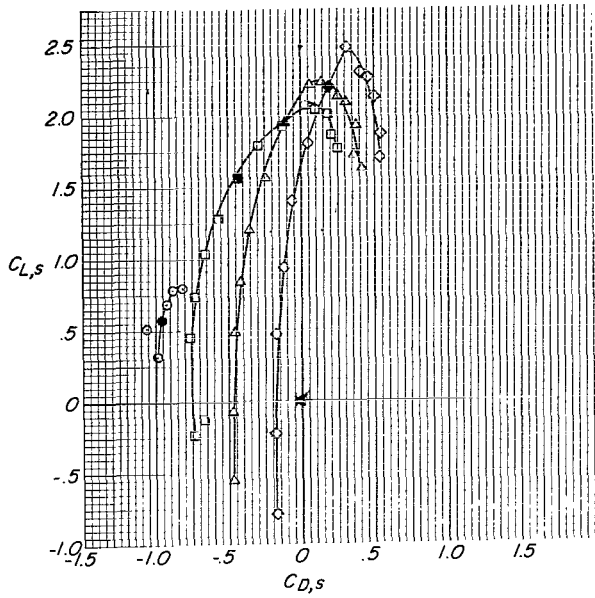
$(C_{T,s})_{nominal}$

- 0.60
- 0.39
- △ 0.20



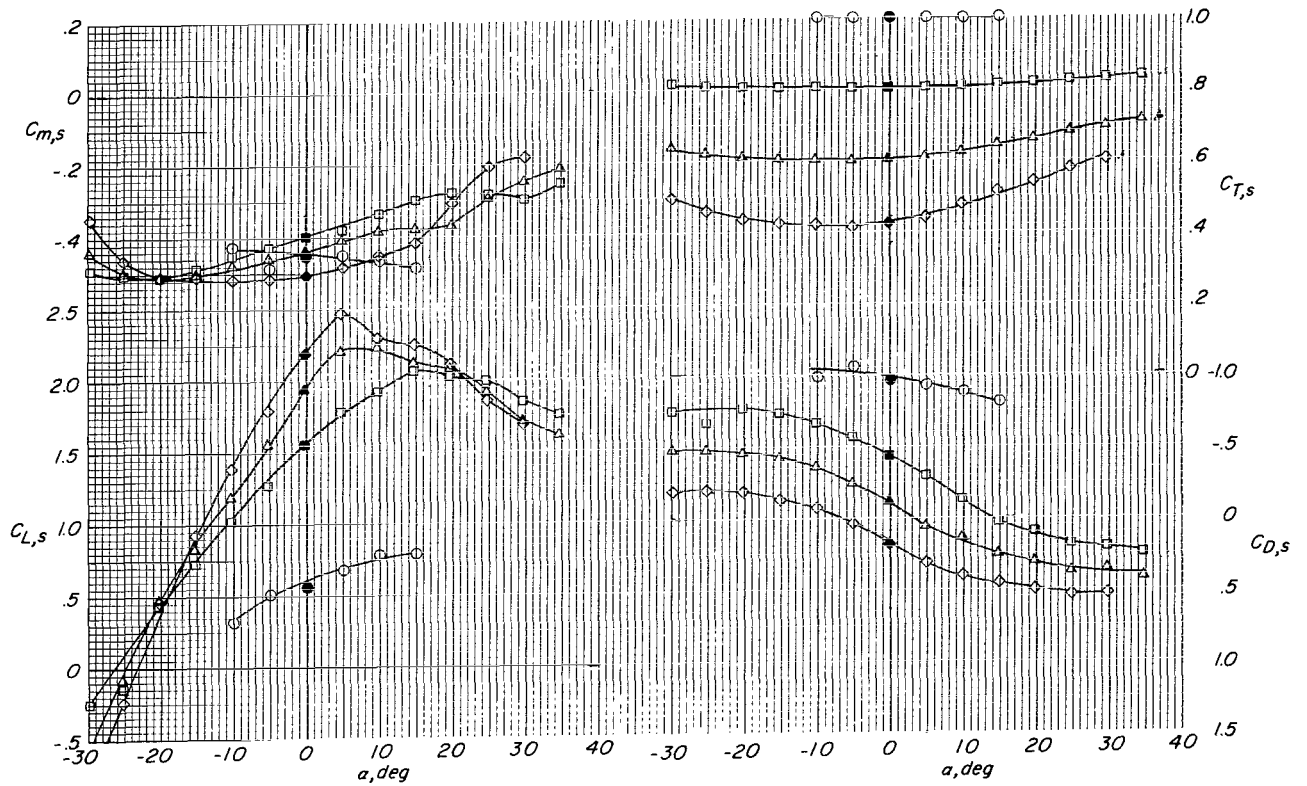
(a)  $i_w = 0^\circ$ .

Figure 14.- Aerodynamic characteristics of tilt-wing VTOL model for several wing incidence angles at various nominal thrust coefficients.  $i_t = 20^\circ$ ;  $S_1$  slat;  $\beta_{75R} = 12^\circ$ ; 7000 rpm;  $h/\bar{c} = \infty$ ;  $\delta_f = 60^\circ$ .



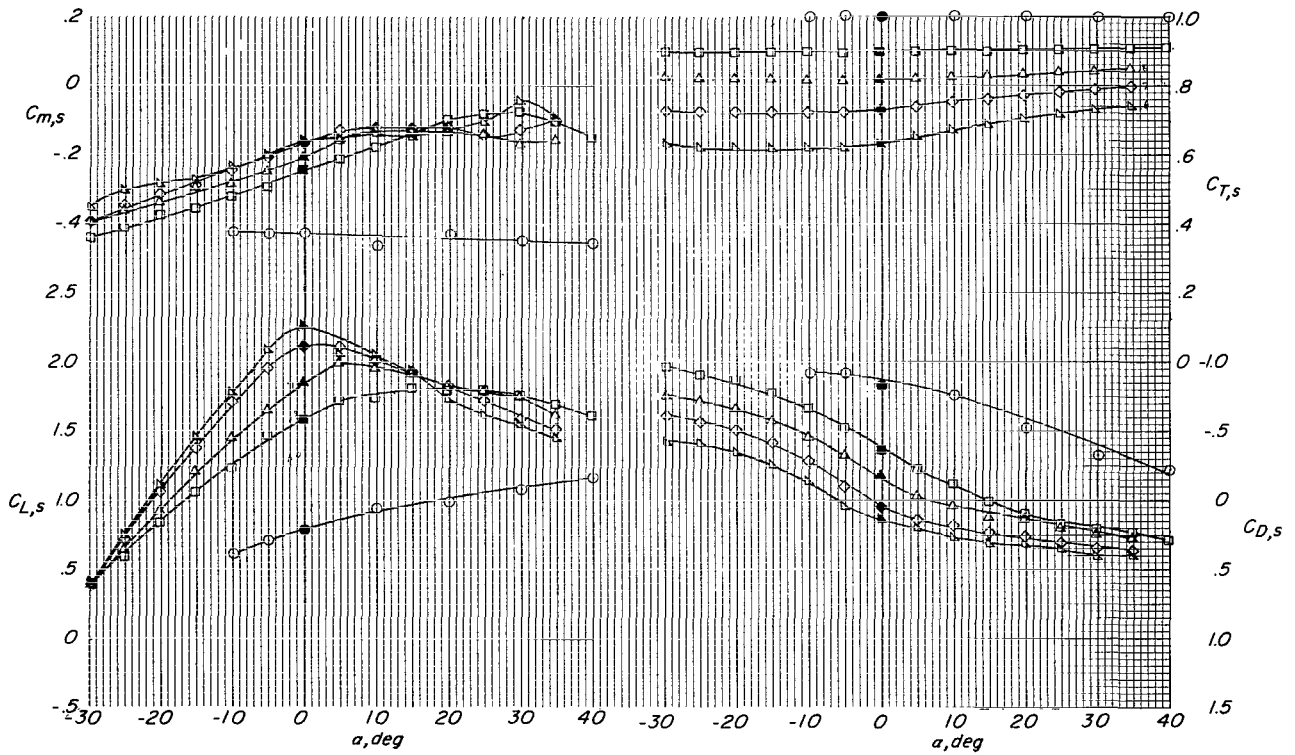
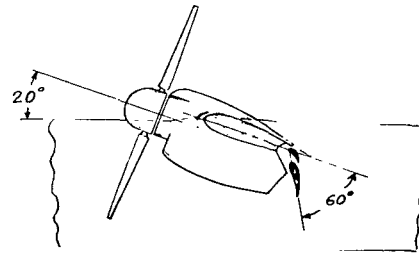
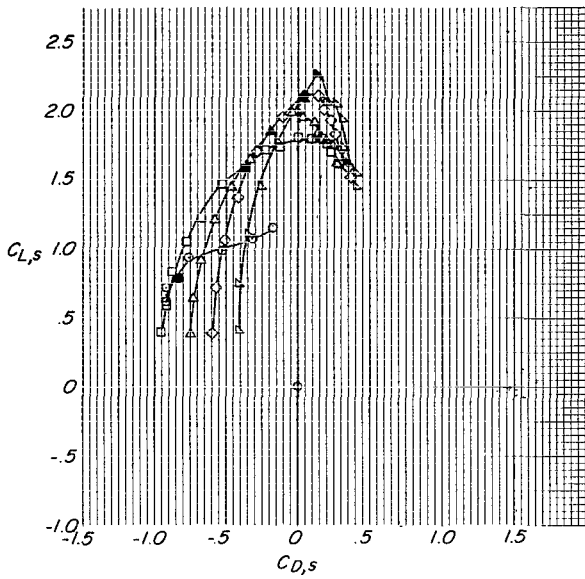
$(C_{T,s})_{nominal}$

- 1.00
- .80
- △ .60
- ◇ .42



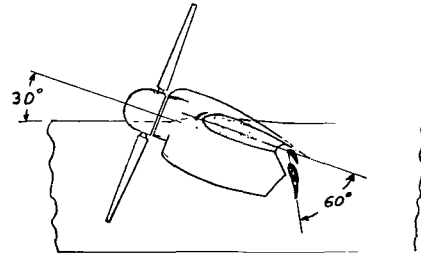
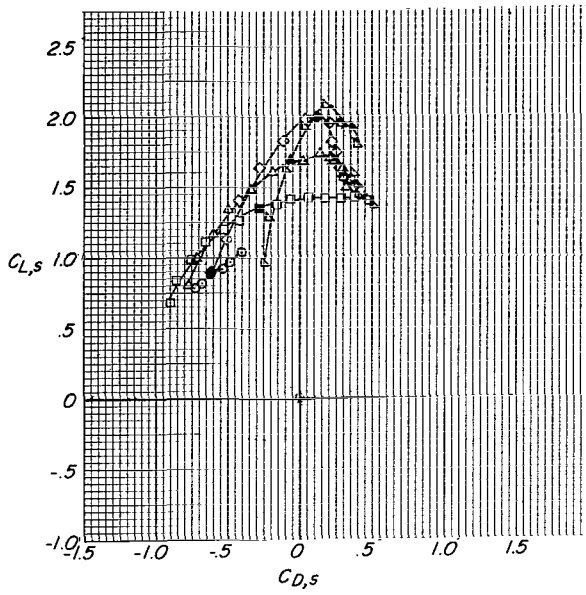
(b)  $i_w = 10^\circ$ .

Figure 14.- Continued.

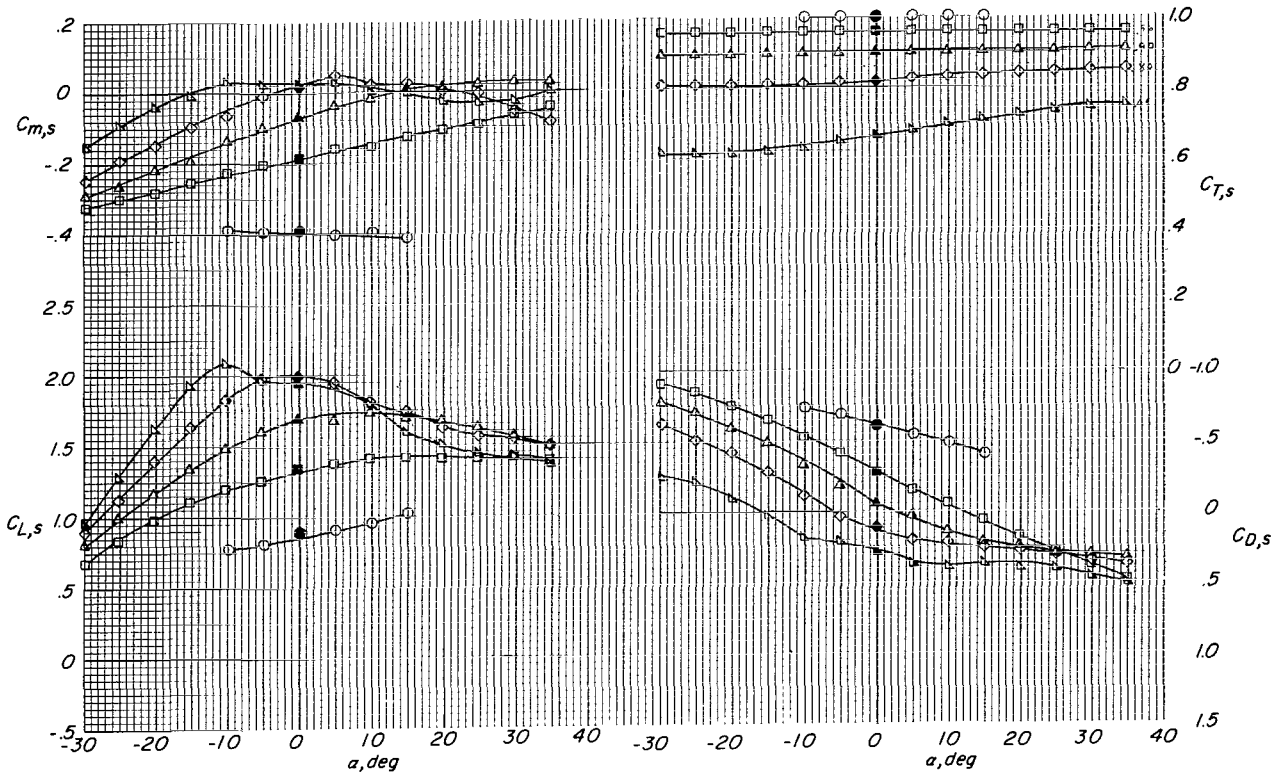


(c)  $i_w = 20^\circ$ .

Figure 14.- Continued.

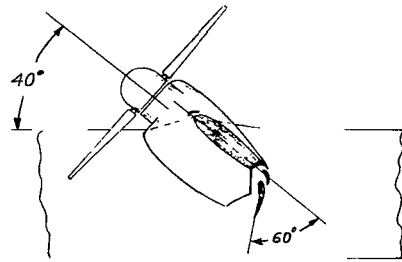
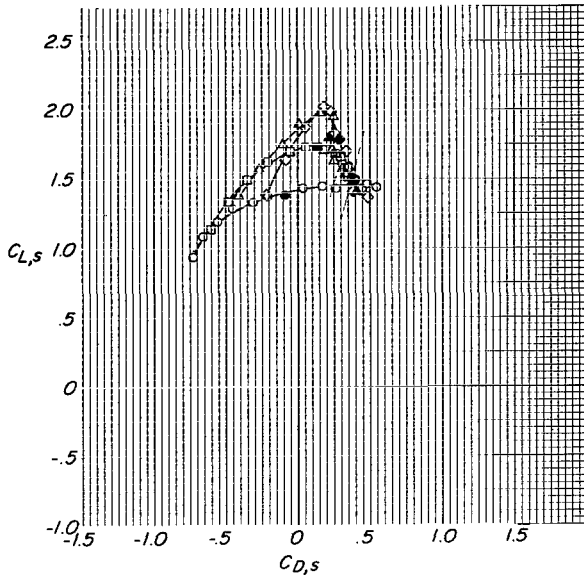


- $(C_{T,s})_{nominal}$
- 1.00
  - .96
  - △ .90
  - ◇ .82
  - ▽ .66

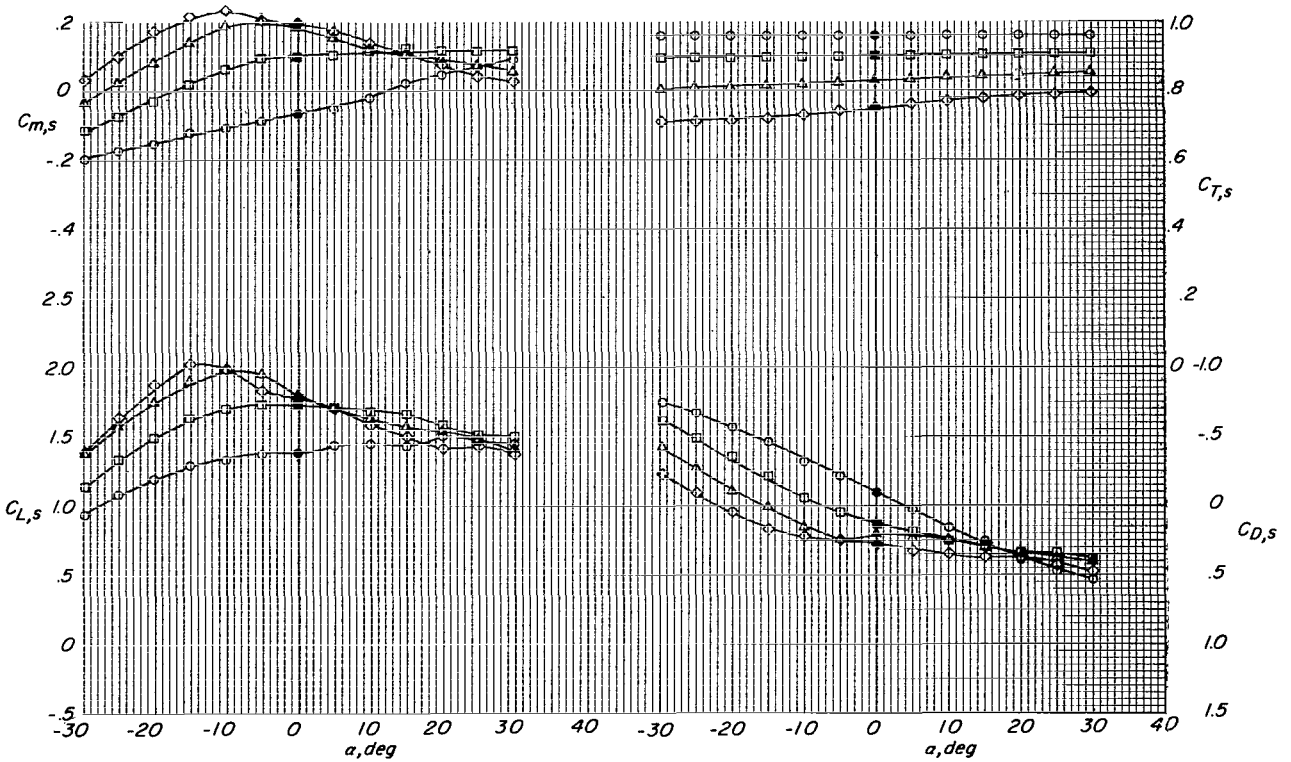


(d)  $i_w = 30^\circ$ .

Figure 14.- Continued.

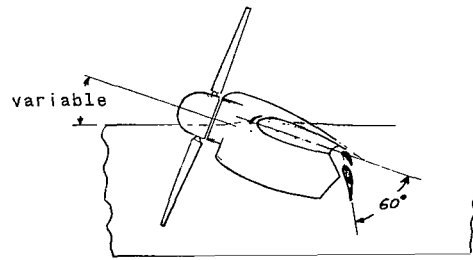
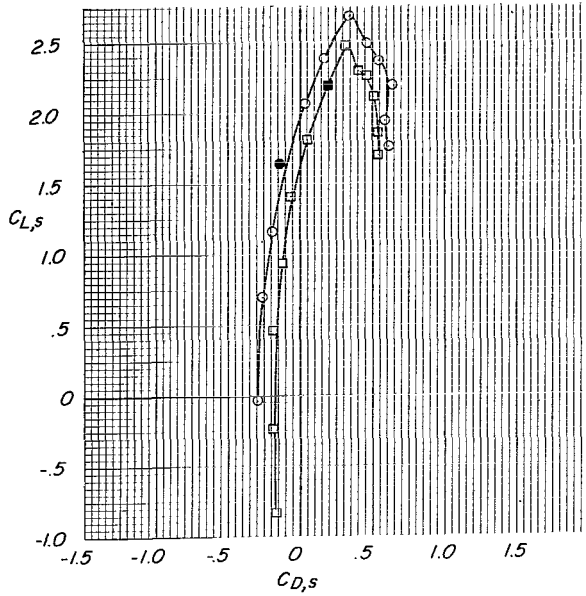


- $(C_{T,s})_{nominal}$
- .96
  - .90
  - △ .83
  - ◇ .75

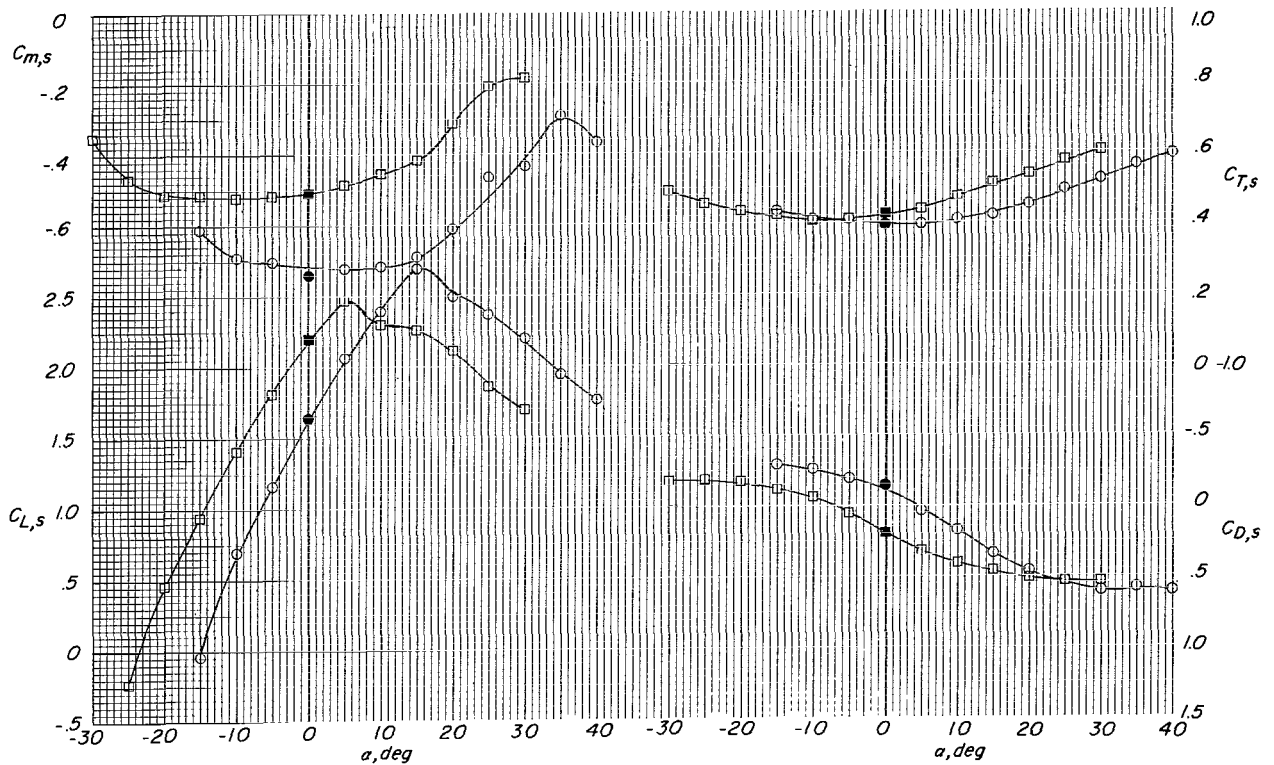


(e)  $i_w = 40^\circ$ .

Figure 14.- Concluded.

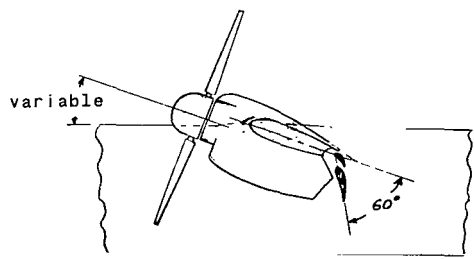
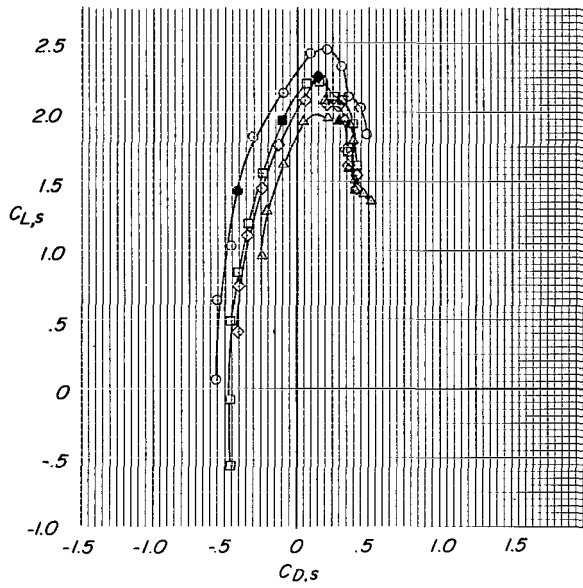


$i_w, deg$   
 ○ 0  
 □ 10

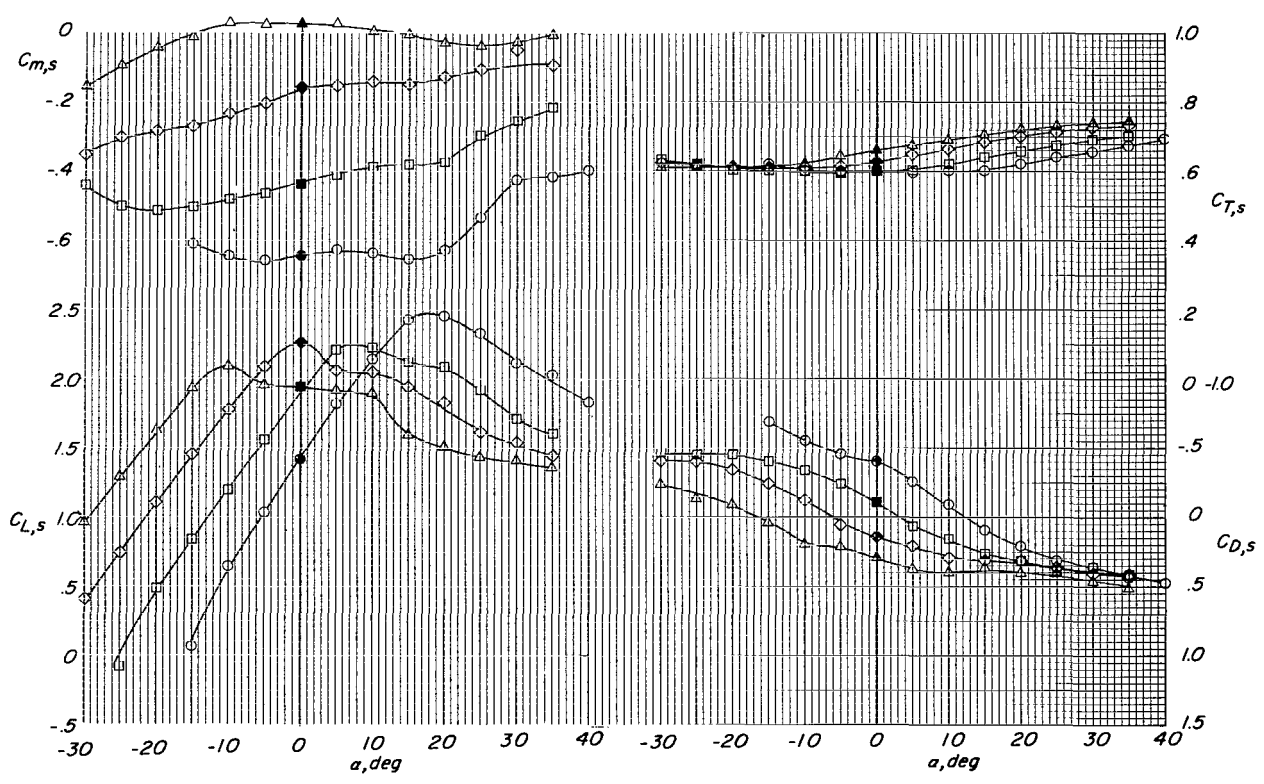


(a)  $(C_{T,s})_{nom} \approx 0.40$ .

Figure 15.- Aerodynamic characteristics of tilt-wing VTOL model for various nominal thrust coefficients at several wing-incidence angles.  $i_t = 20^\circ$ ;  $S_1$  slat;  $\beta_{75R} = 12^\circ$ ; 7000 rpm;  $h/\bar{c} = \infty$ ;  $\delta_f = 60^\circ$ .

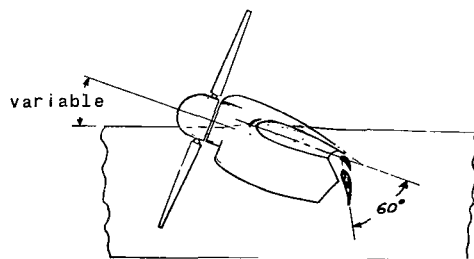
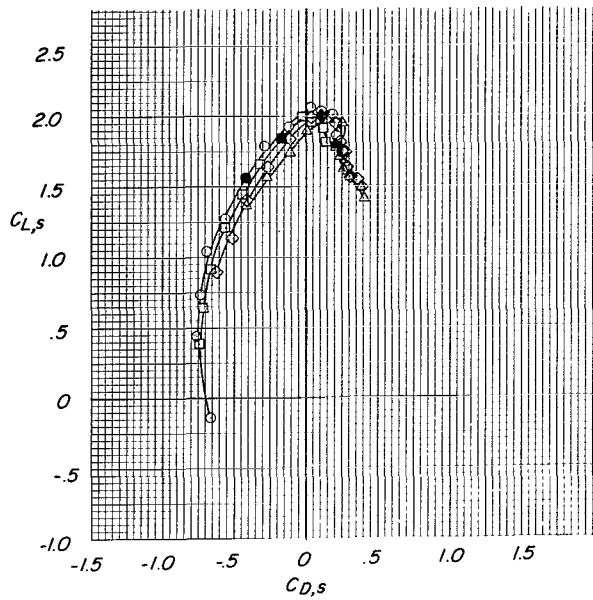


- $i_w, \text{deg}$
- 0
  - 10
  - ◇ 20
  - △ 30

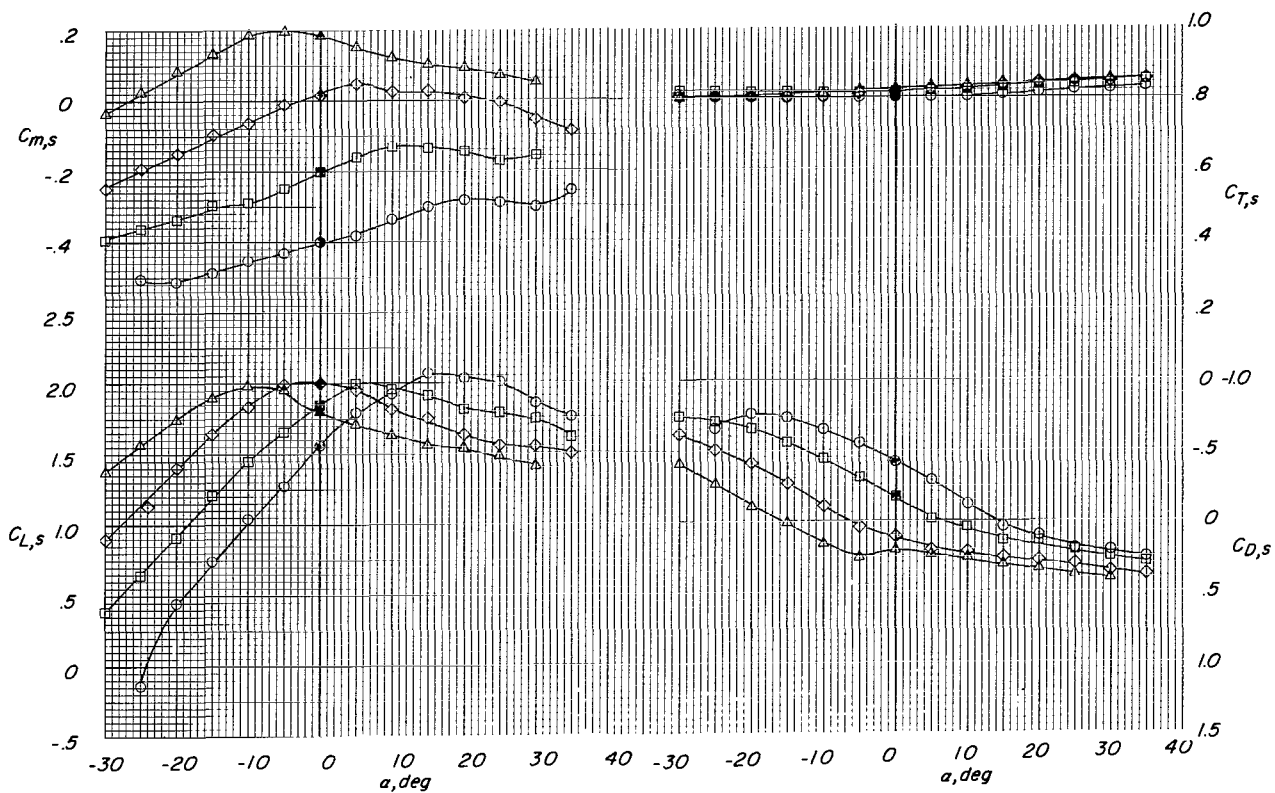


(b)  $(C_{T,s})_{\text{nom}} \approx 0.60$ .

Figure 15.- Continued.

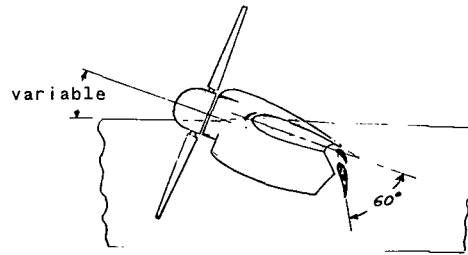
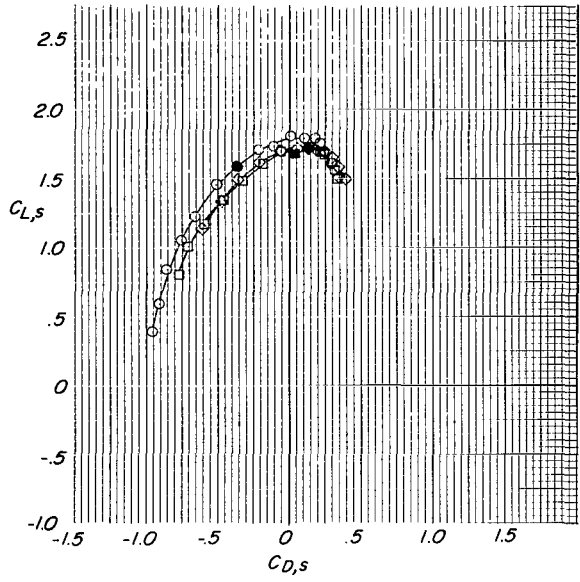


- $i_w, \text{deg}$
- 10
  - 20
  - ◇ 30
  - △ 40

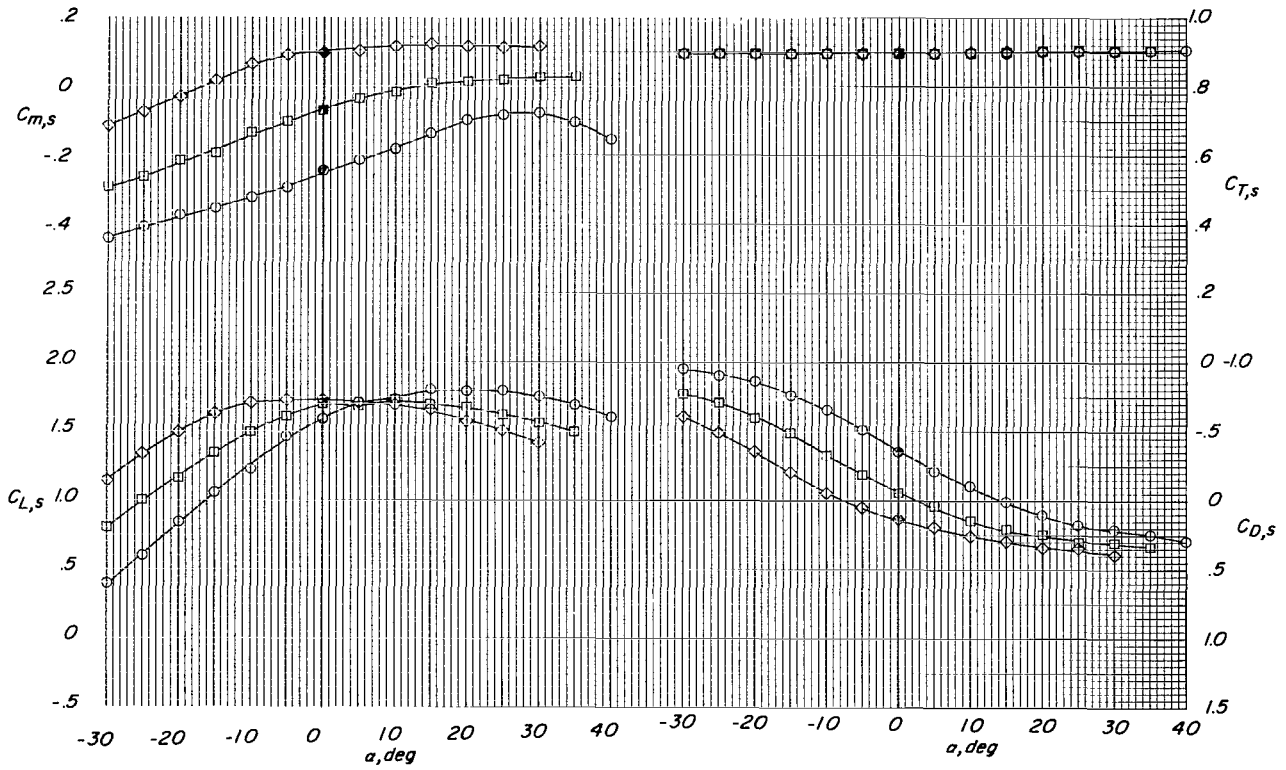


(c)  $(C_{T,s})_{\text{nom}} \approx 0.80$ .

Figure 15.- Continued.

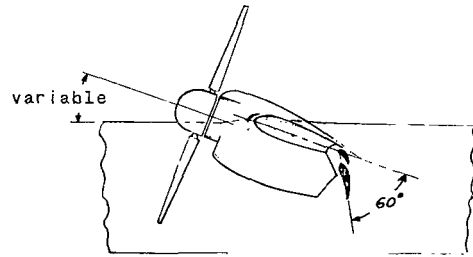
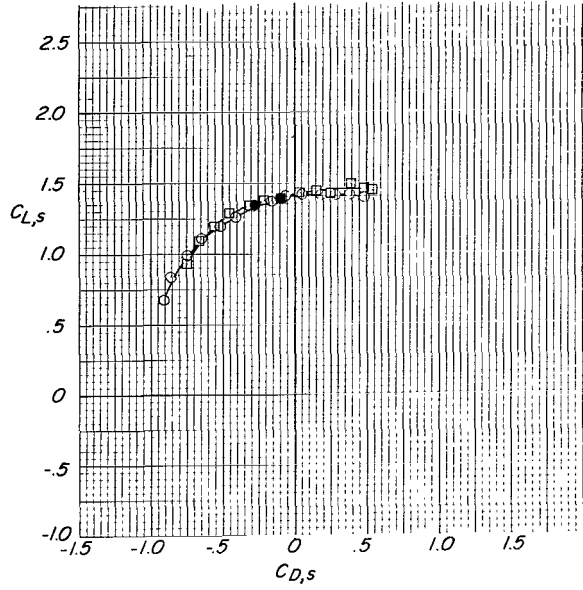


- $i_w, deg$
- 20
  - 30
  - ◇ 40

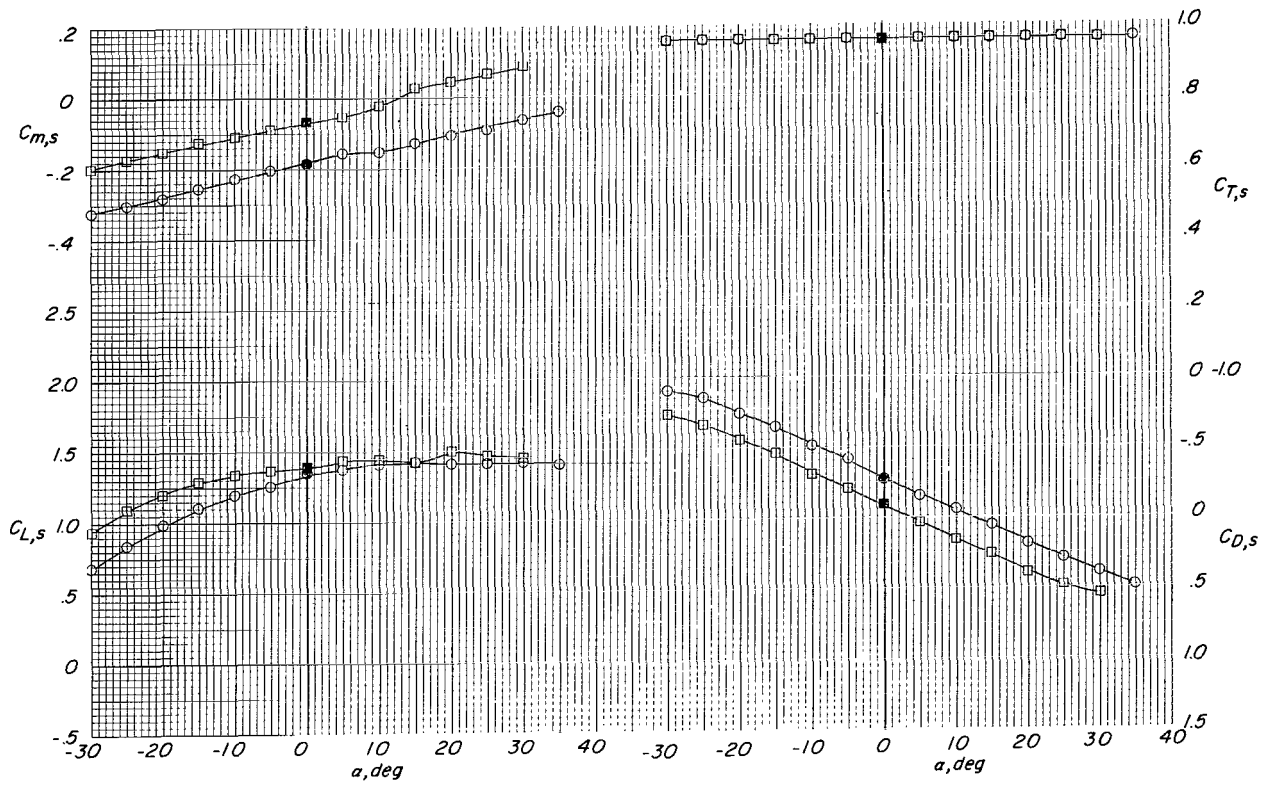


(d)  $(C_{T,s})_{nom} \approx 0.90$ .

Figure 15.- Continued.

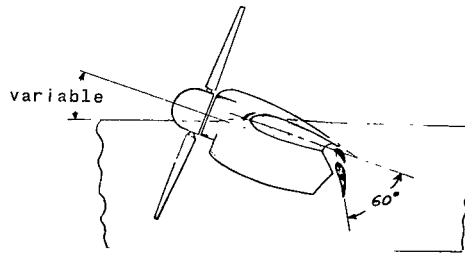
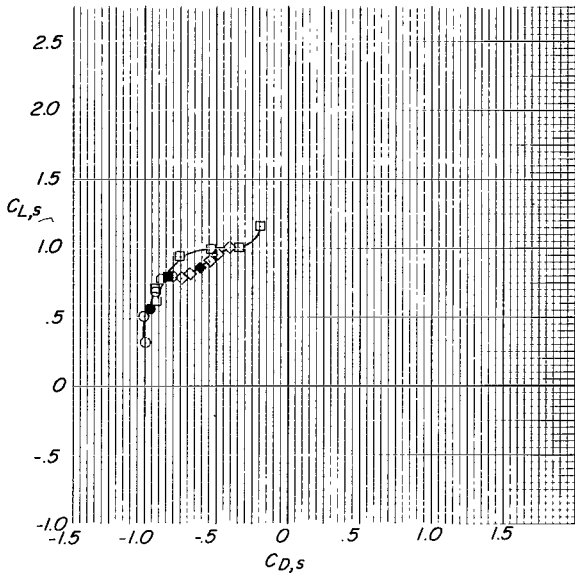


$i_w, \text{deg}$   
 ○ 30  
 □ 40

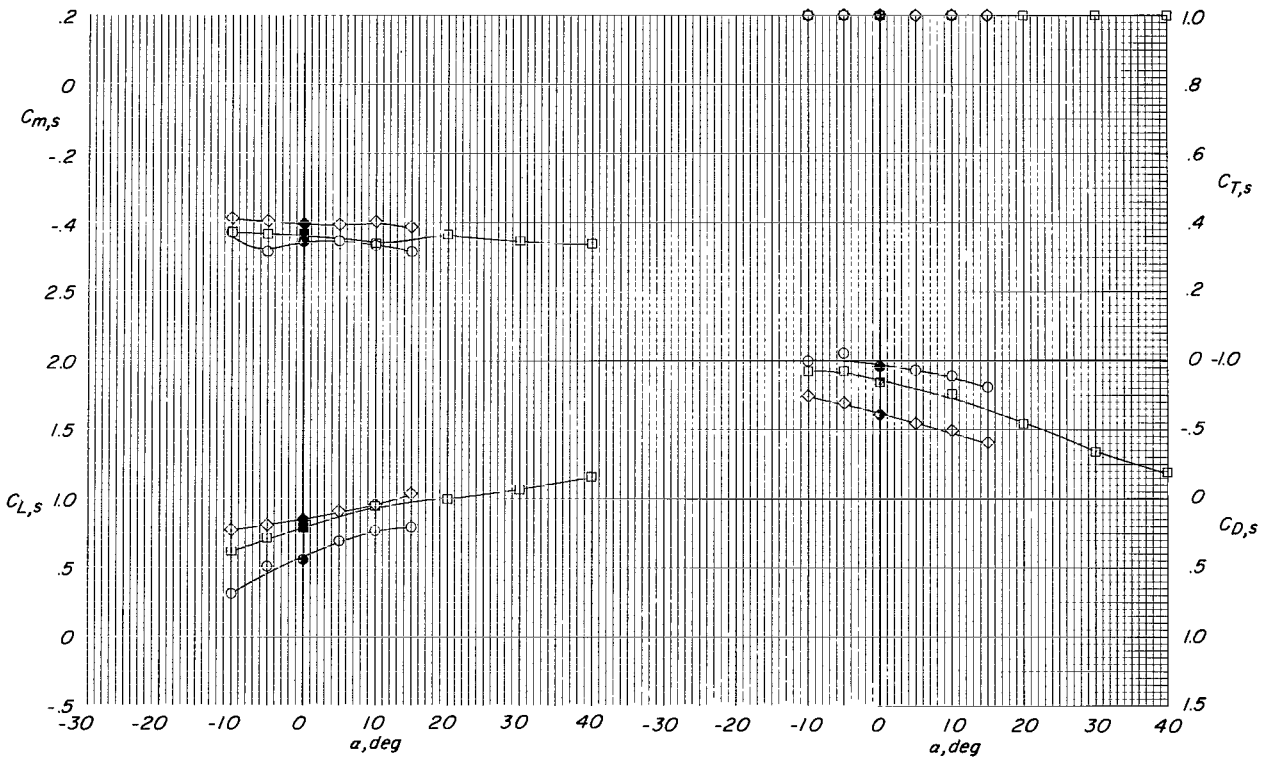


(e)  $(C_{T,s})_{\text{nom}} \approx 0.96$ .

Figure 15.- Continued.

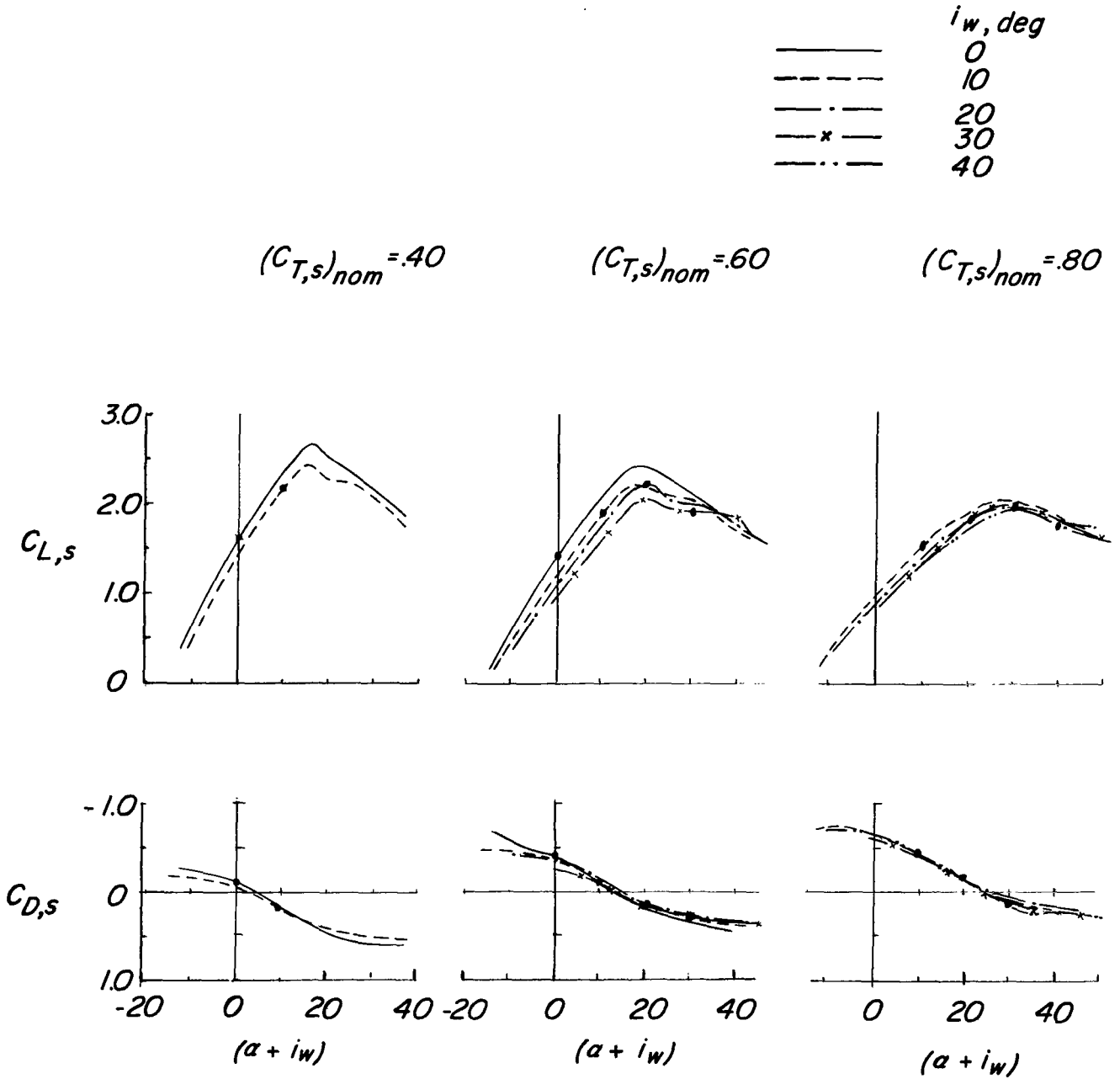


$i_w, \text{deg}$   
 ○ 10  
 □ 20  
 ◇ 30



(f)  $(C_{T,s})_{\text{nom}} \approx 1.00$ .

Figure 15.- Concluded.



(a)  $(C_{T,s})_{nom} = 0.40, 0.60, \text{ and } 0.80.$

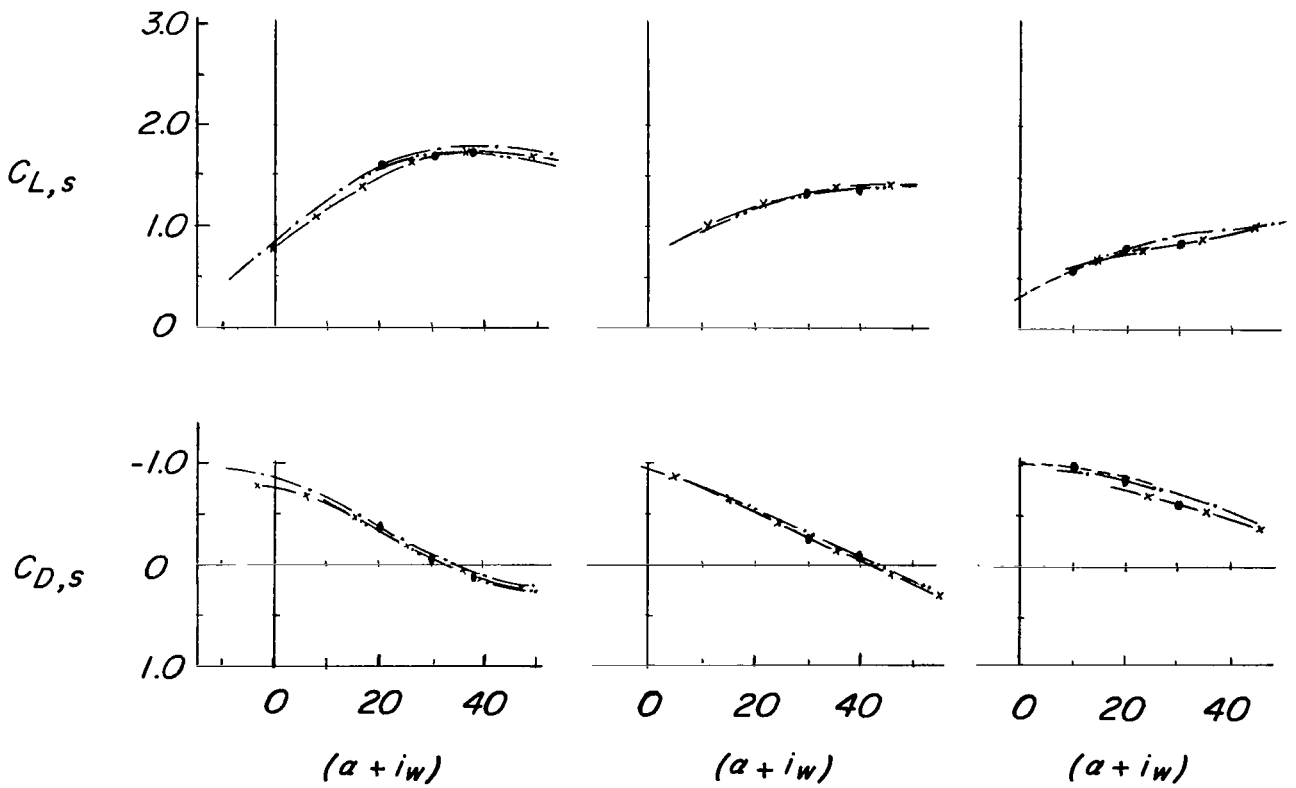
Figure 16.- Variation of lift and drag characteristics with total wing angle of attack  $(\alpha + i_w)$  for various wing-incidence angles.  $i_t = 20^\circ$ ;  $S_1$  slat;  $\beta_{.75R} = 12^\circ$ ; 7000 rpm;  $h/\bar{c} = \infty$ ;  $\delta_f = 60^\circ$ .

	$i_w, \text{deg}$
————	0
- - - - -	10
- · - · -	20
— x —	30
- · · - ·	40

$(C_{T,s})_{nom} = 0.90$

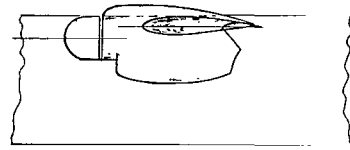
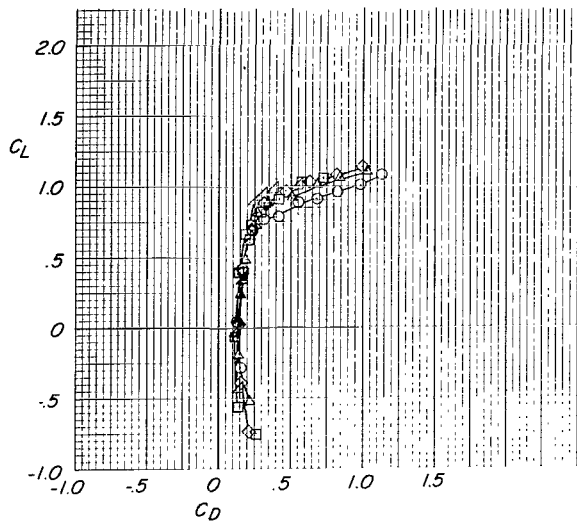
$(C_{T,s})_{nom} = 0.96$

$(C_{T,s})_{nom} = 1.00$

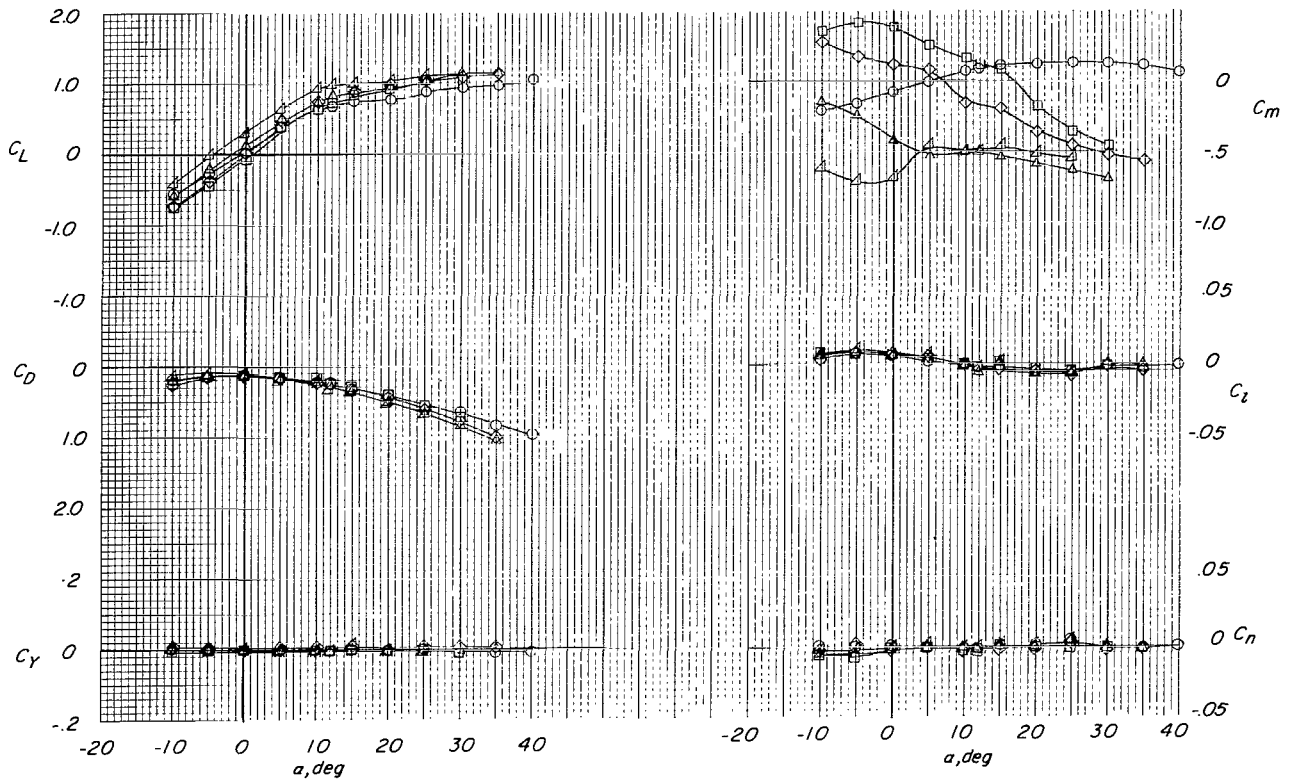


(b)  $(C_{T,s})_{nom} = 0.90, 0.96, \text{ and } 1.00.$

Figure 16.- Concluded.

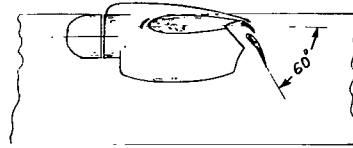
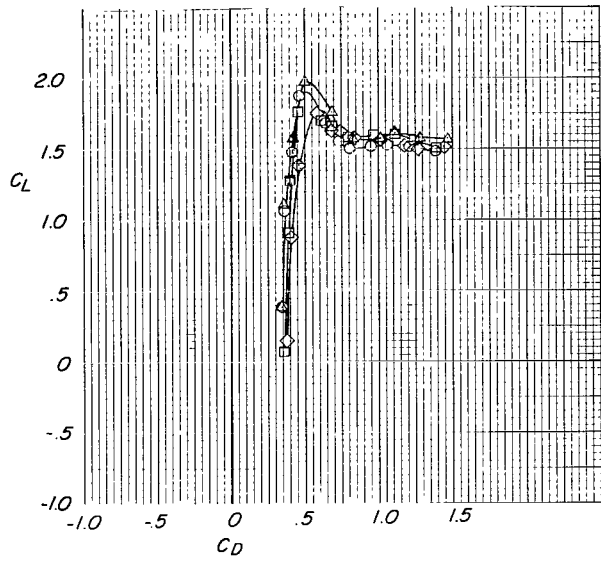


- $i_t, \text{deg}$
- Off
  - -5
  - ◇ 0
  - △ 10
  - △ 20

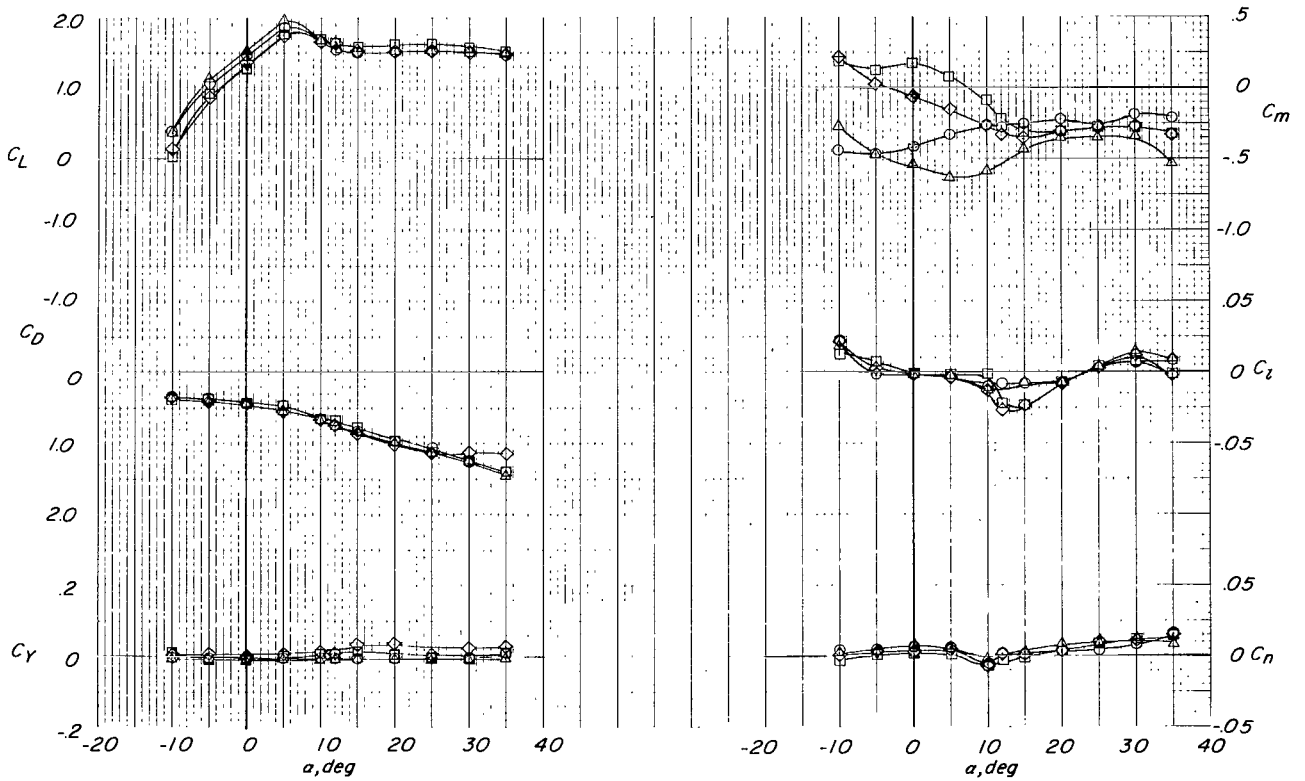


(a)  $\delta_f = 0^\circ$ ; slat off.

Figure 17.- Power-off aerodynamic characteristics of a tilt-wing VTOL model at several horizontal-tail incidence angles.  $h/\bar{c} = \infty$ ;  $i_w = 0^\circ$ .

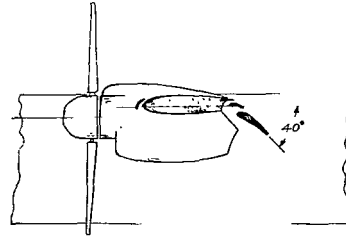
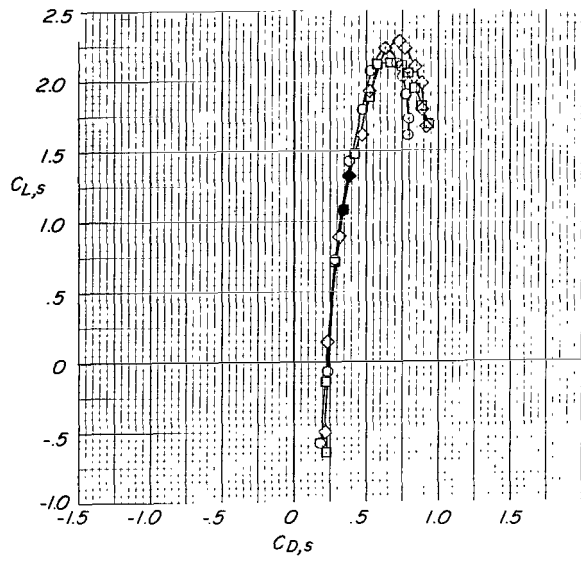


- $i_t, \text{deg}$
- Off
  - ◇ -5
  - 0
  - △ 10

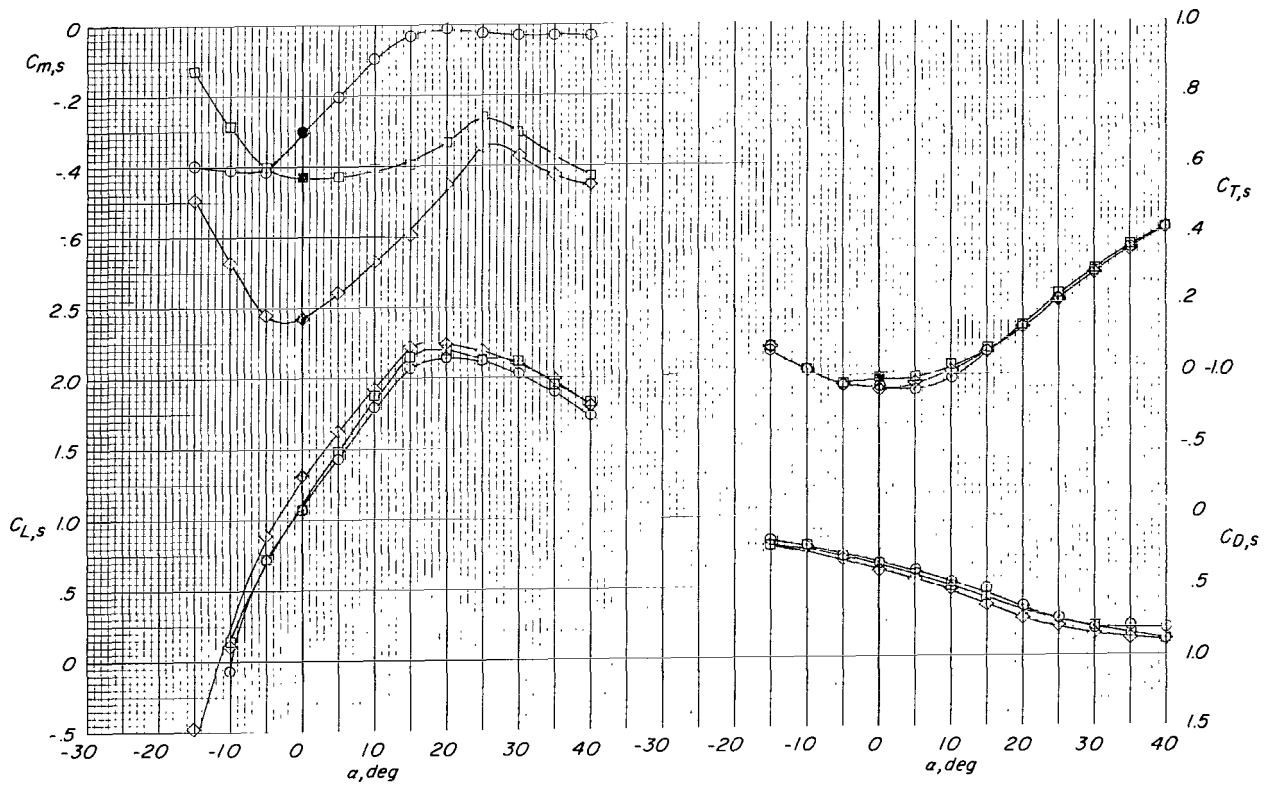


(b)  $\delta_f = 60^\circ$ ;  $S_1$  slat.

Figure 17.- Concluded.

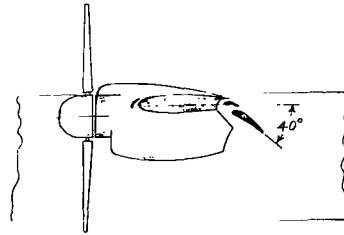
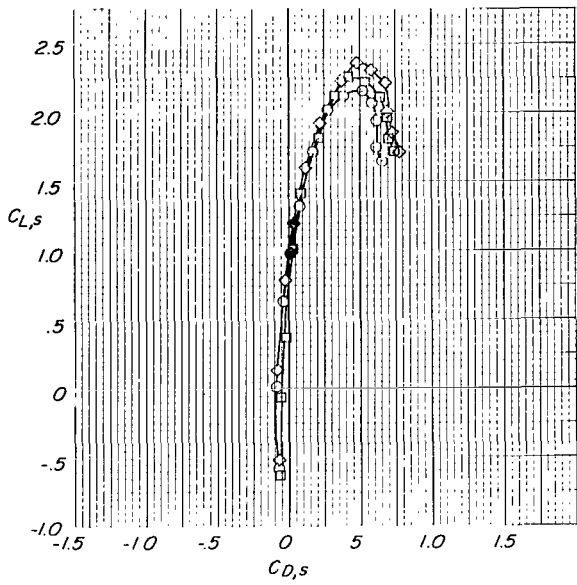


$i_t, \text{deg}$   
 ○ Off  
 □ 10  
 ◇ 20



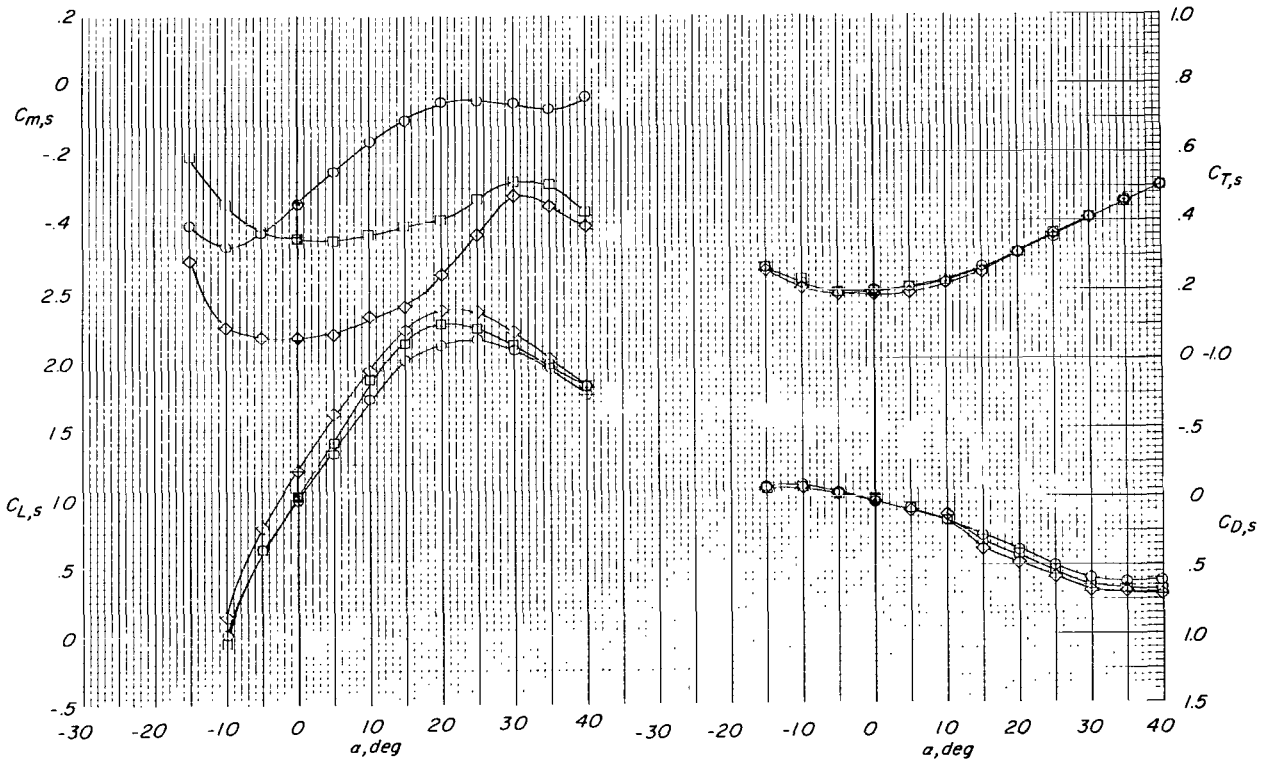
(a)  $(C_{T,s})_{\text{nom}} \approx 0$ .

Figure 18.- Effect of horizontal-tail deflection on aerodynamic characteristics of tilt-wing VTOL model at several nominal thrust coefficients.  $S_1$  slat;  $\beta_{.75R} = 12^\circ$ ; 7000 rpm;  $h/c = \infty$ ;  $i_w = 0^\circ$ ;  $\delta_f = 40^\circ$ .



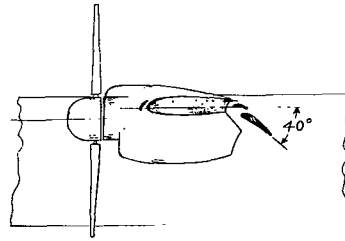
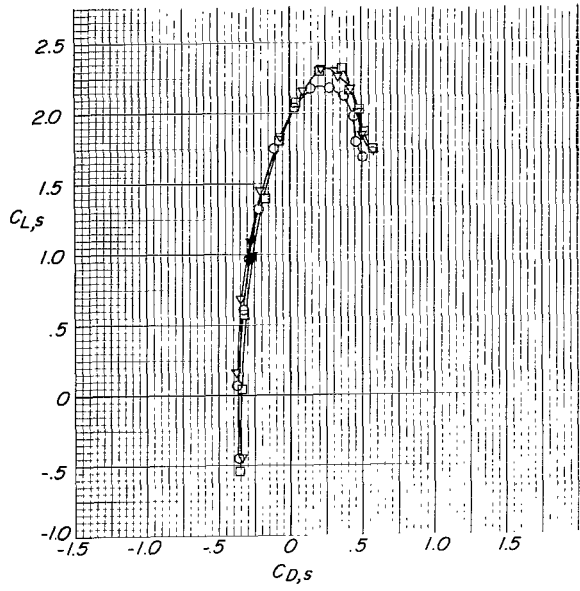
$i_t, \text{deg}$

- Off
- 10
- ◇ 20

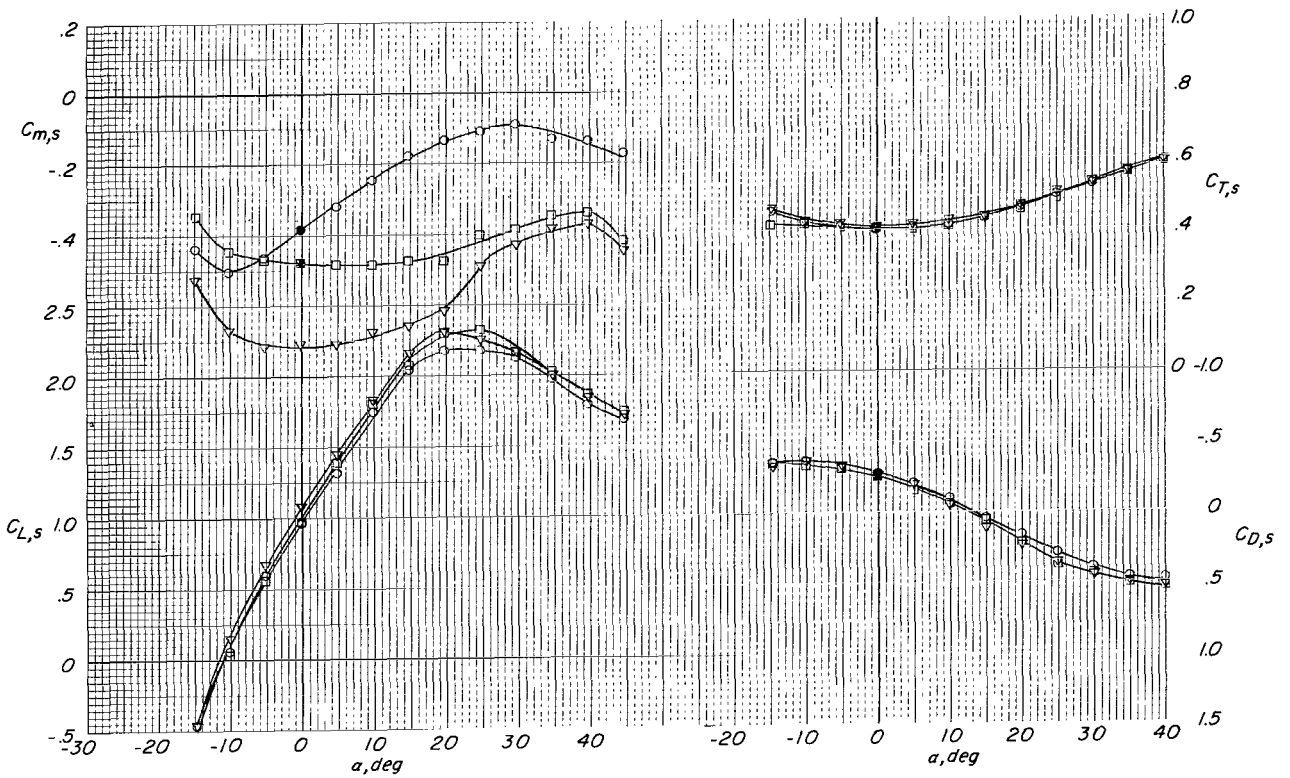


(b)  $(C_{T,s})_{\text{nom}} \approx 0.20$ .

Figure 18.- Continued.

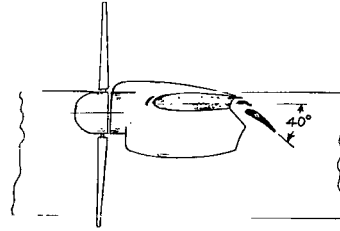
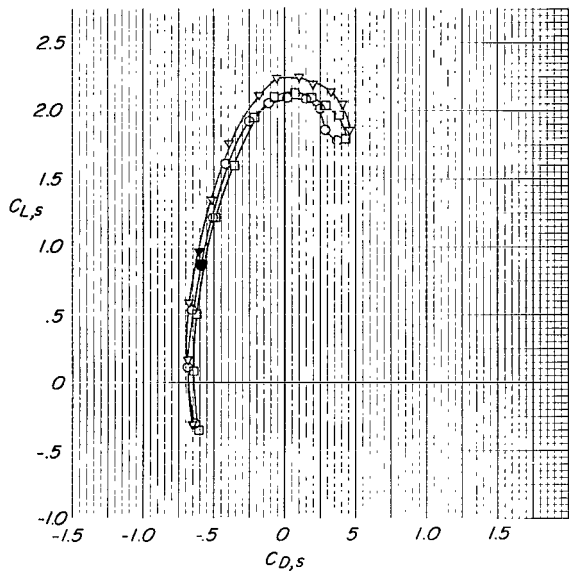


$i_1, \text{deg}$   
 ○ Off  
 □ 10  
 ▽ 20

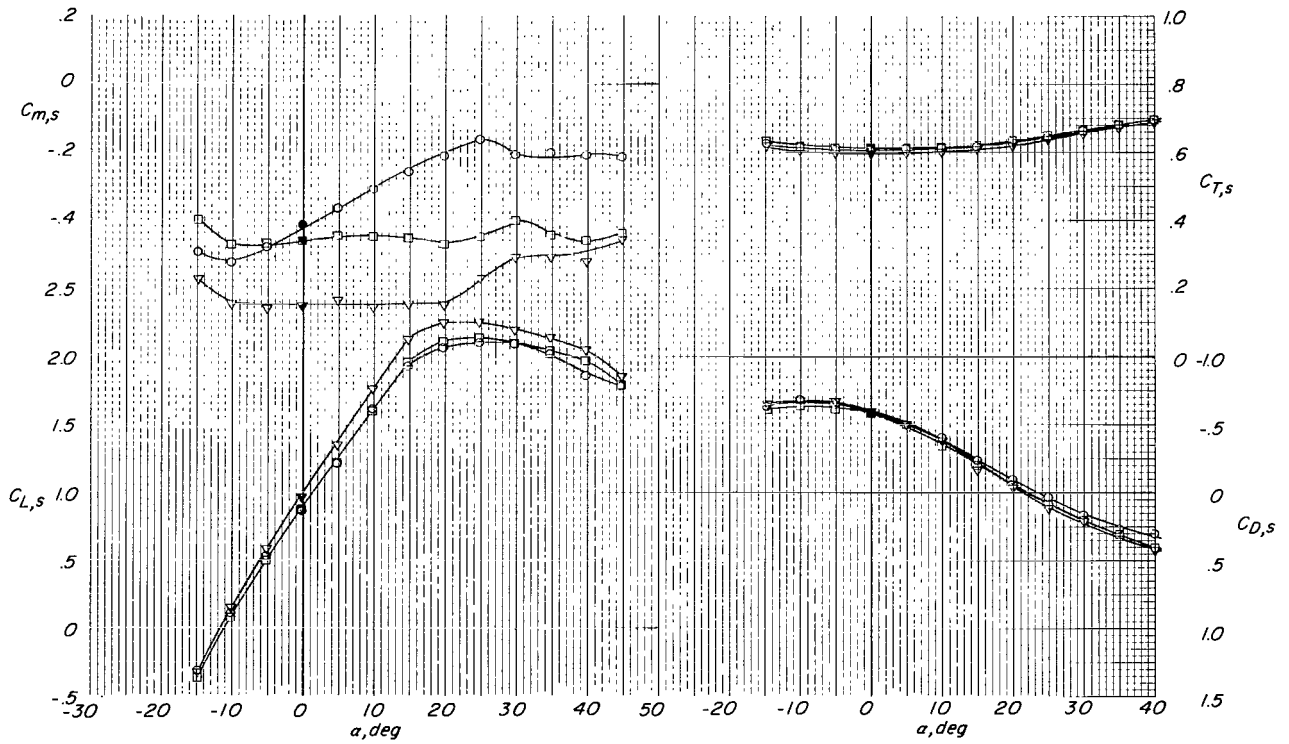


(c)  $(C_{T,s})_{\text{nom}} \approx 0.40$ .

Figure 18.- Continued.

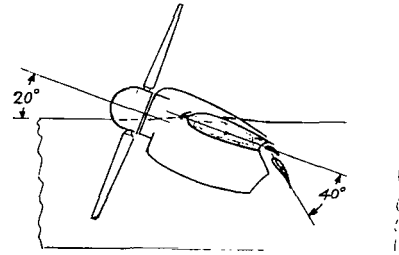
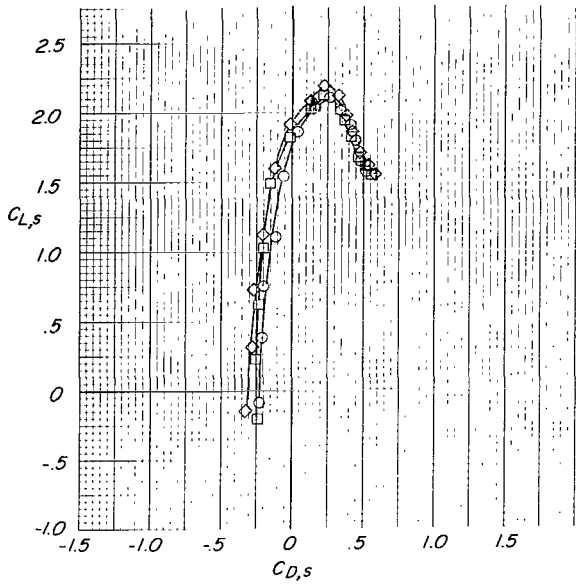


$i_t, \text{deg}$   
 ○ Off  
 □ 10  
 ▽ 20

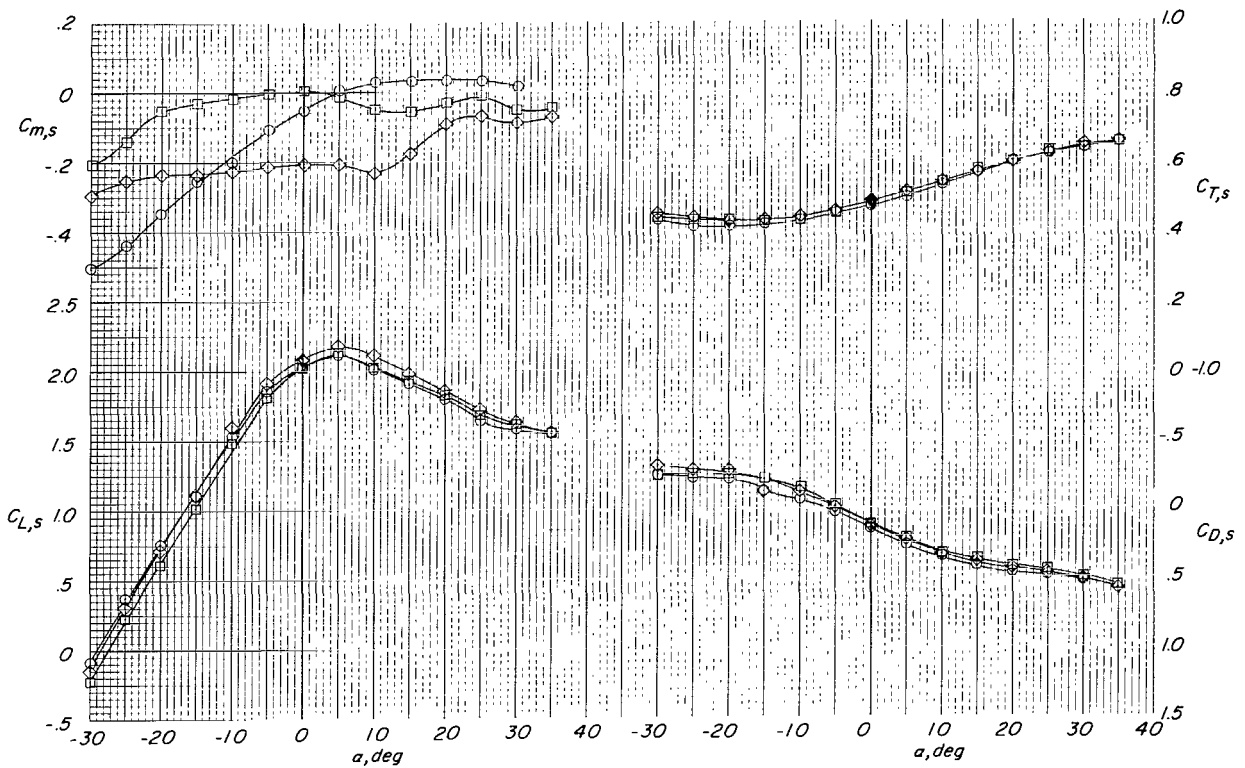


(d)  $(C_{T,s})_{\text{nom}} \approx 0.60$ .

Figure 18.- Concluded.

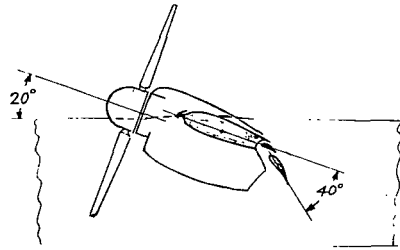
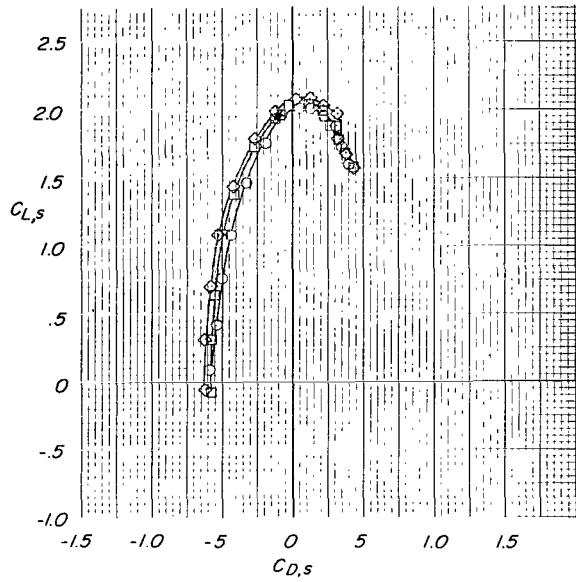


- $i_t, \text{deg}$
- Off
  - 10
  - ◇ 20

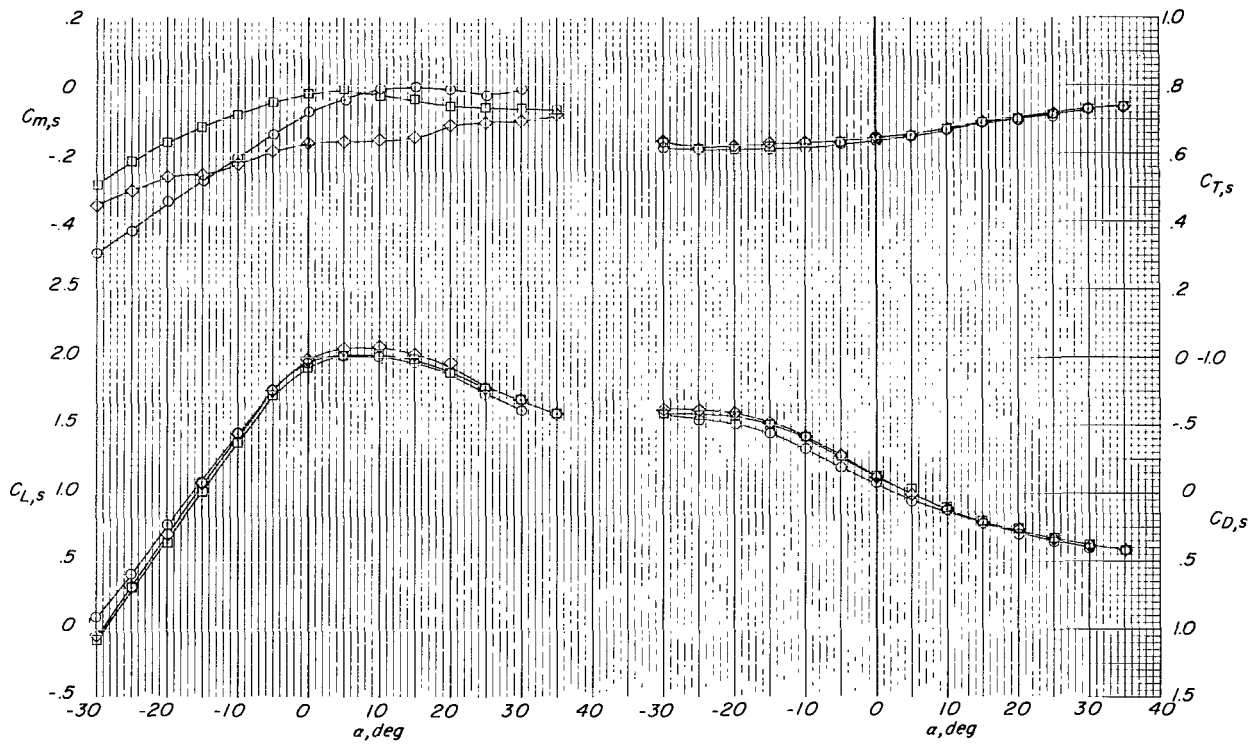


(a)  $(C_{T,s})_{\text{nom}} \approx 0.48$ .

Figure 19.- Effect of horizontal-tail deflection on aerodynamic characteristics of tilt-wing VTOL model at several nominal thrust coefficients.  $S_1$  slat;  $\beta_{75R} = 12^\circ$ ; 7000 rpm;  $h/c = \infty$ ;  $i_w = 20^\circ$ ;  $\delta_f = 40^\circ$ .

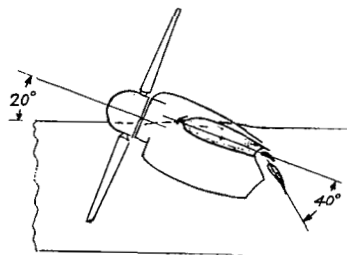
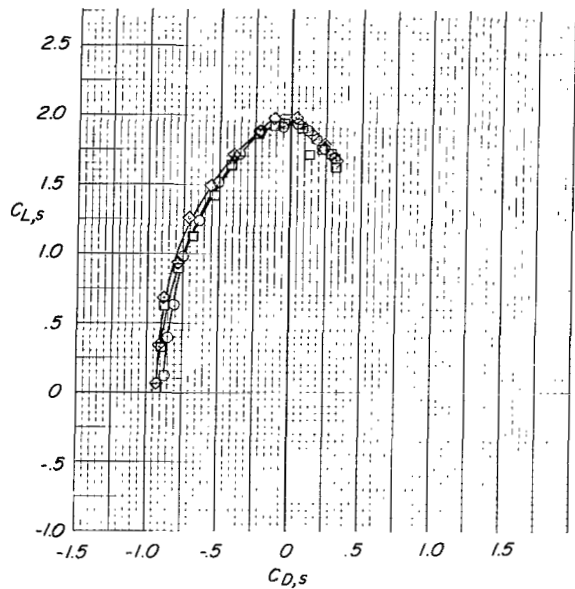


$i_t, \text{deg}$   
 ○ Off  
 □ 10  
 ◇ 20

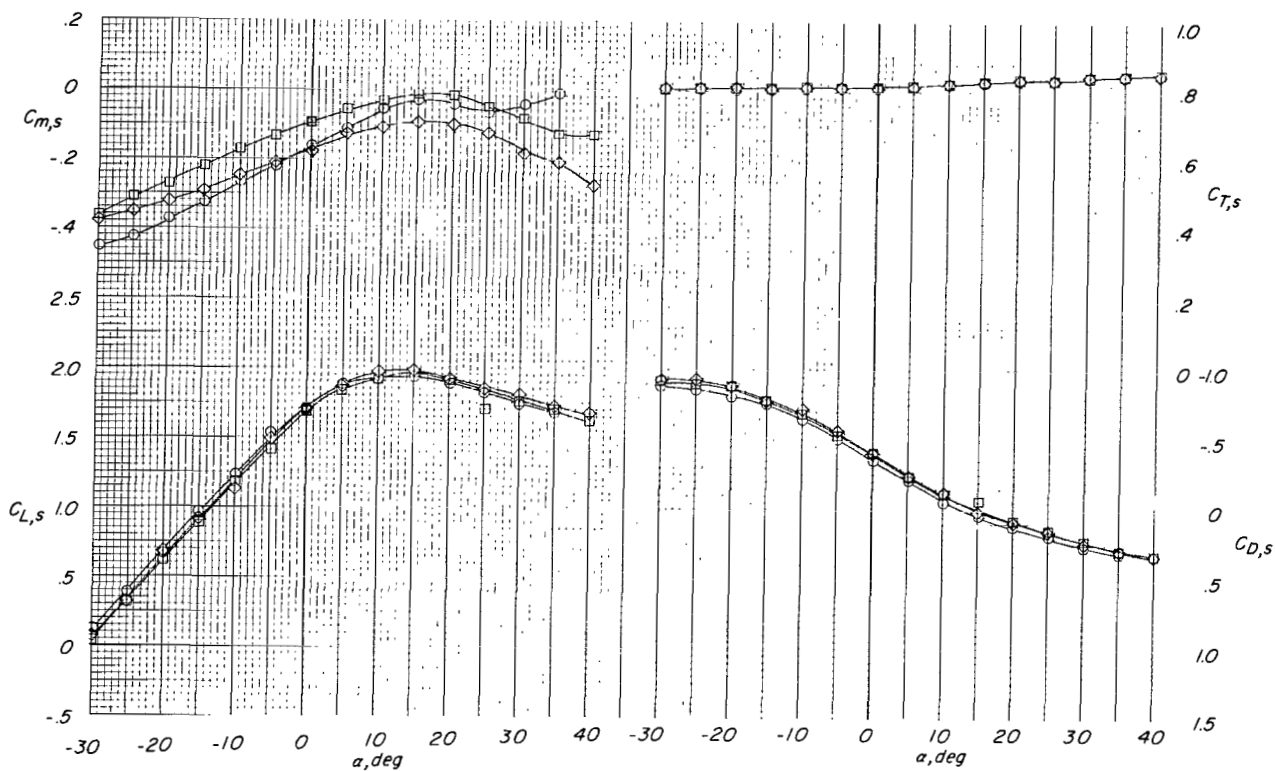


(b)  $(C_{T,s})_{\text{nom}} \approx 0.63$ .

Figure 19.- Continued.

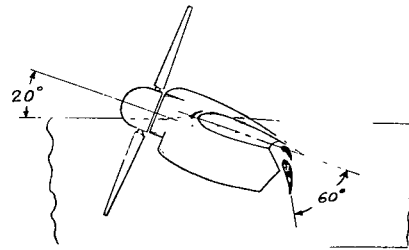
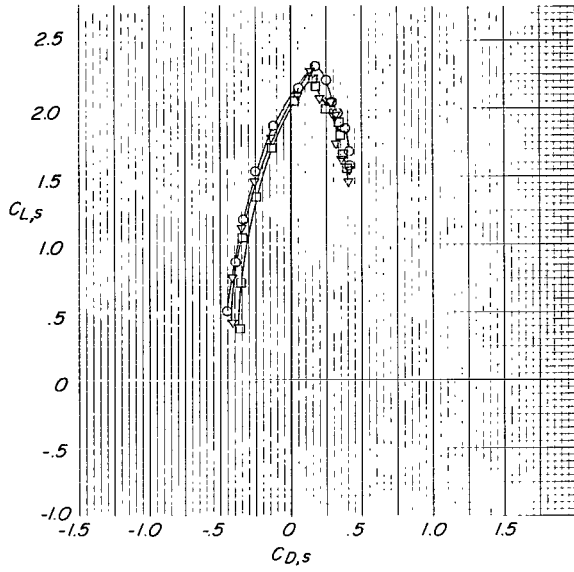


- $i_t, \text{deg}$
- Off
  - 10
  - ◇ 20

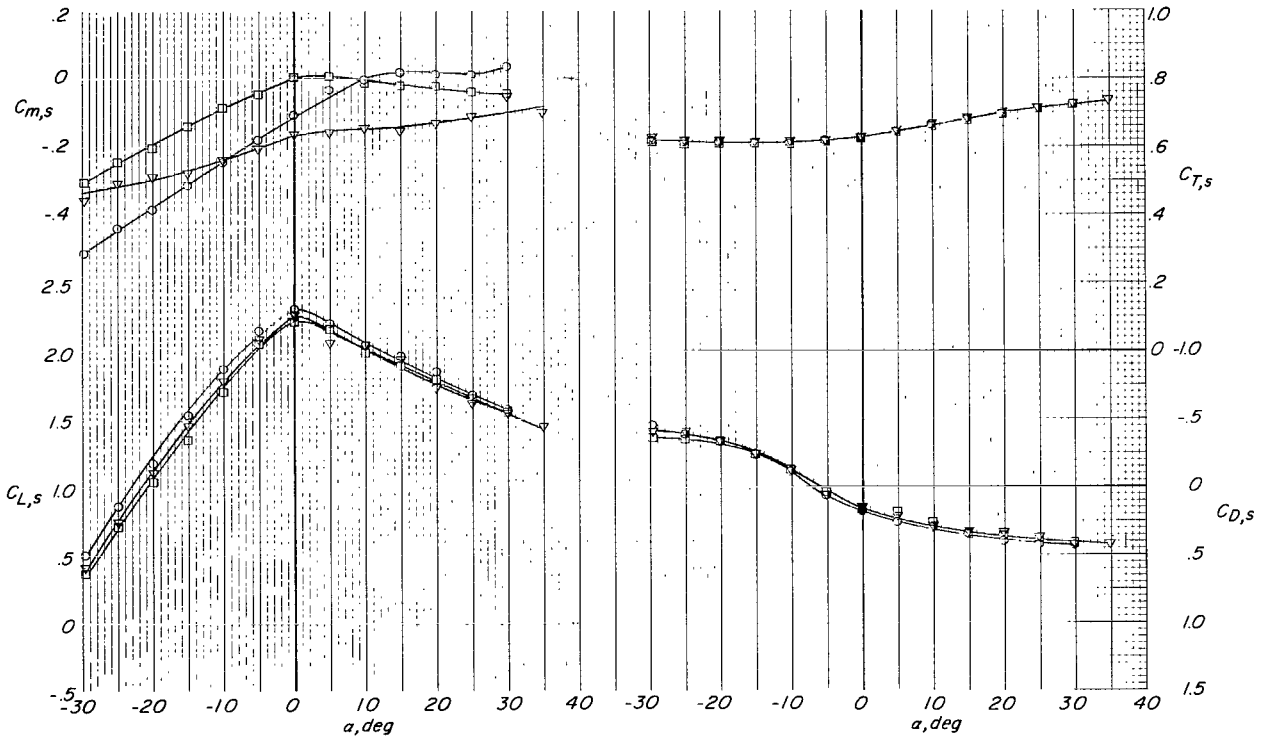


(c)  $(C_{T,s})_{\text{nom}} \approx 0.80$ .

Figure 19.- Concluded.

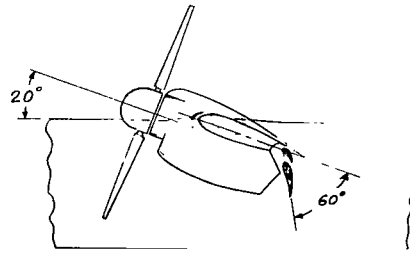
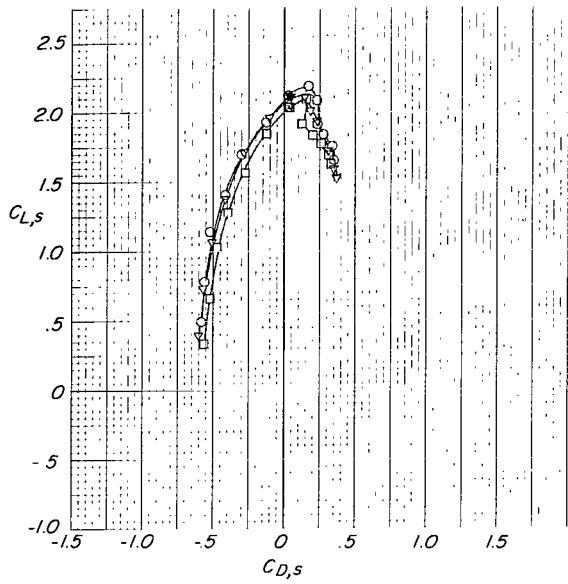


$i_t, \text{deg}$   
 ○ Off  
 □ 10  
 ▽ 20

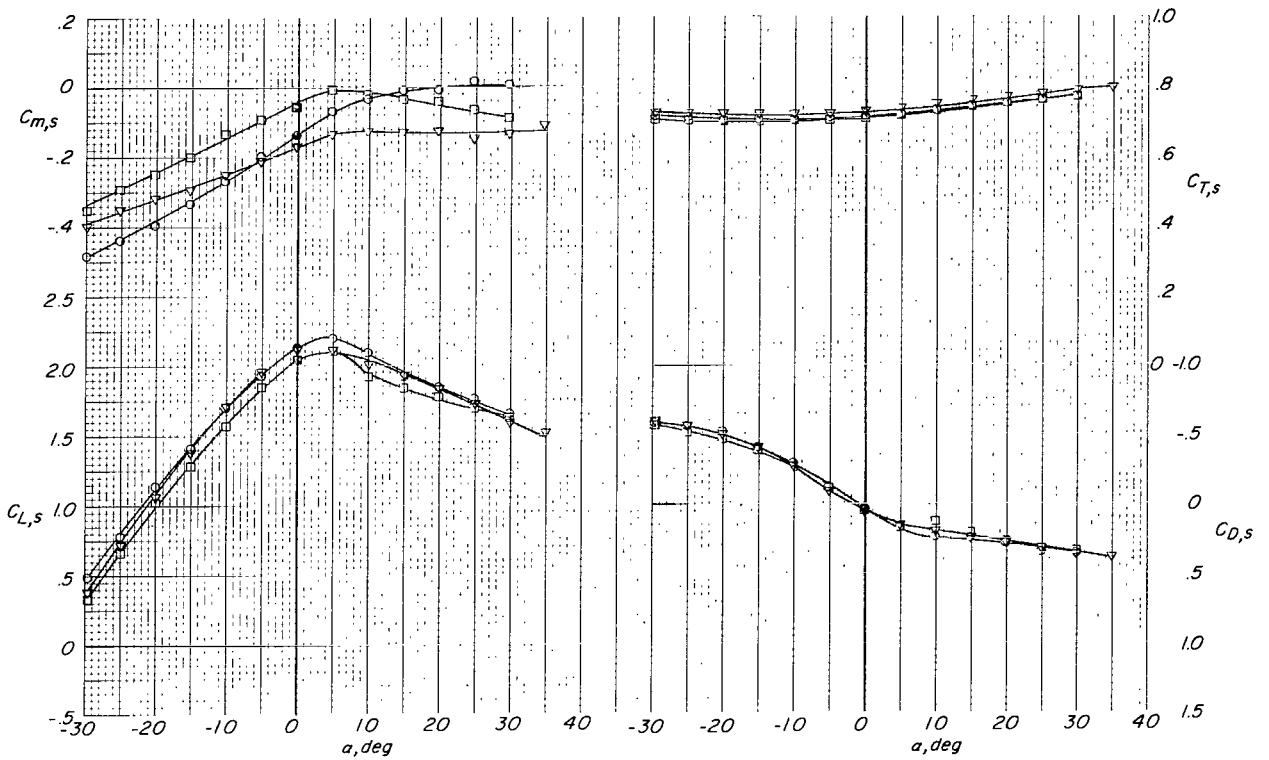


(a)  $(C_{T,s})_{\text{nom}} \approx 0.63$ .

Figure 20.- Effect of horizontal-tail deflection on aerodynamic characteristics of tilt-wing VTOL model at several nominal thrust coefficients.  $S_1$  slat;  $\beta_{.75R} = 12^\circ$ ; 7000 rpm;  $h/\bar{c} = \infty$ ;  $i_w = 20^\circ$ ;  $\delta_f = 60^\circ$ .

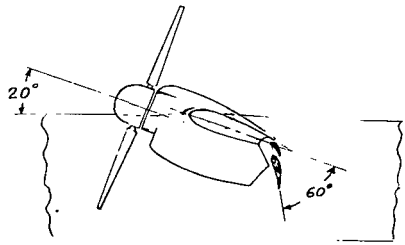
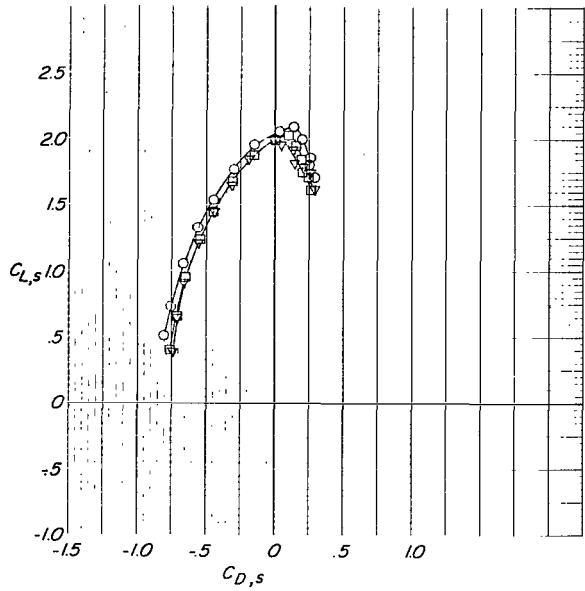


$i_f, \text{deg}$   
 ○ Off  
 □ 10  
 ▼ 20

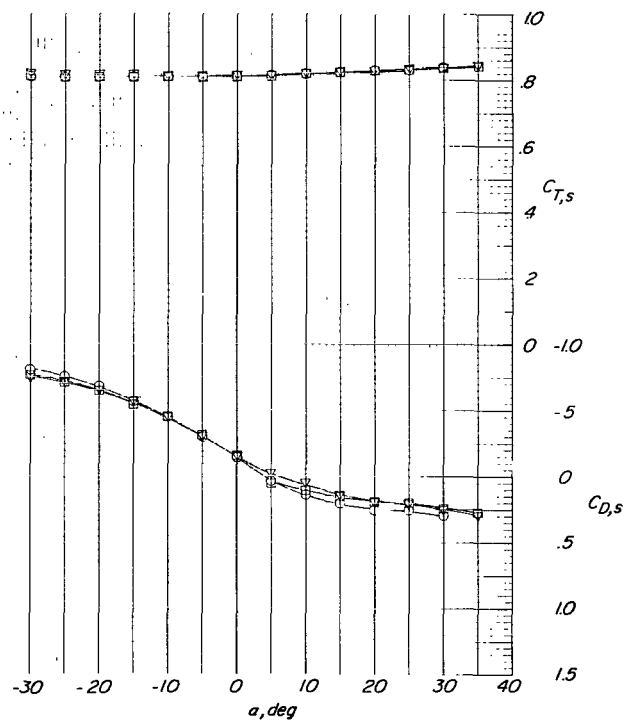
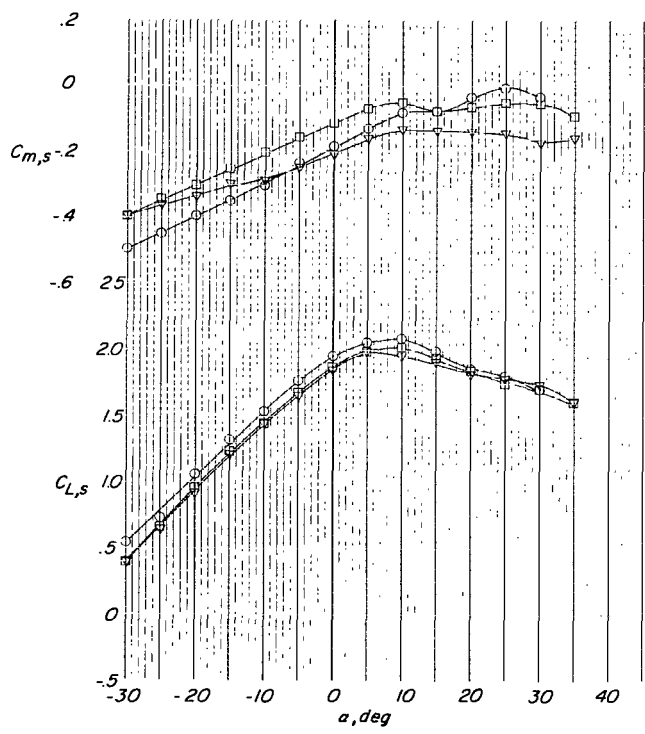


(b)  $(C_{T,s})_{\text{nom}} \approx 0.70$ .

Figure 20.- Continued.

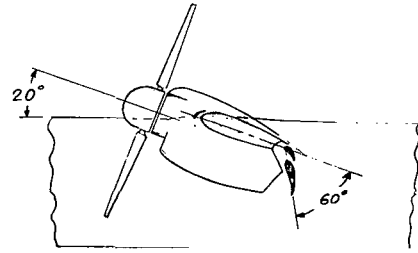
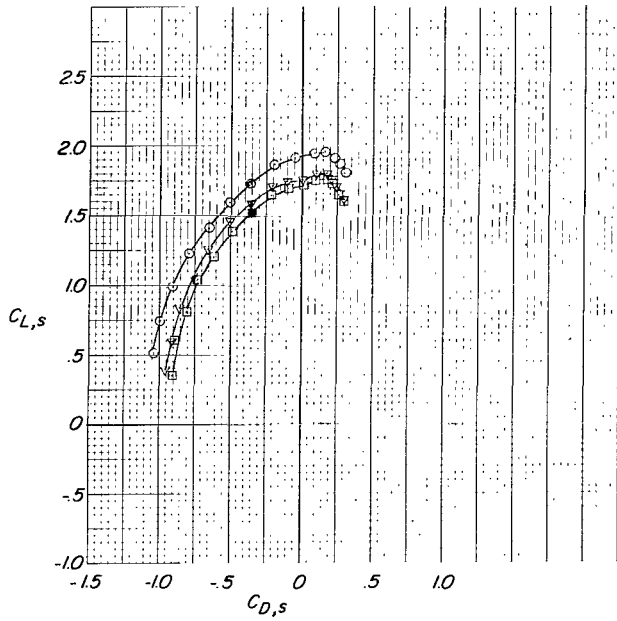


- $i_t, \text{deg}$
- Off
  - 10
  - ▽ 20

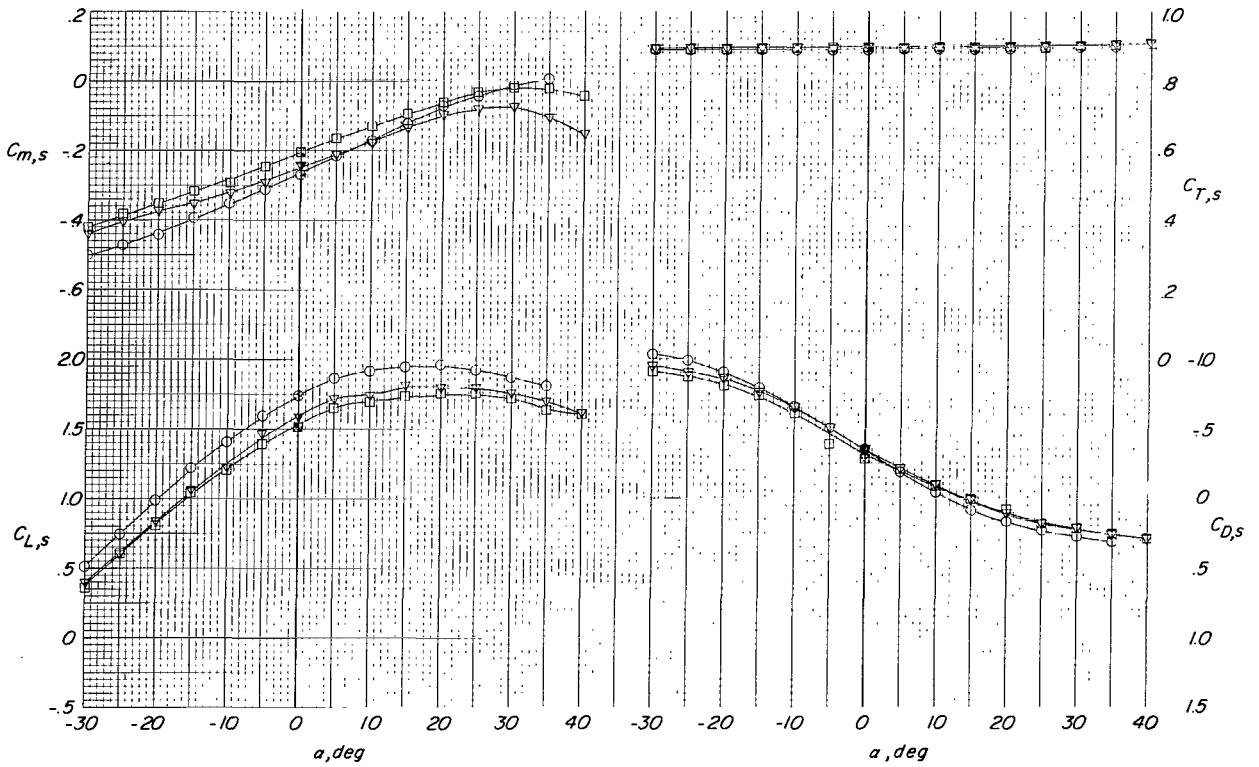


(c)  $(C_{T,s})_{\text{nom}} \approx 0.80$ .

Figure 20.- Continued.

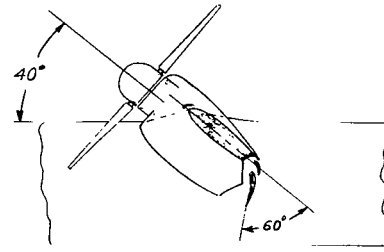
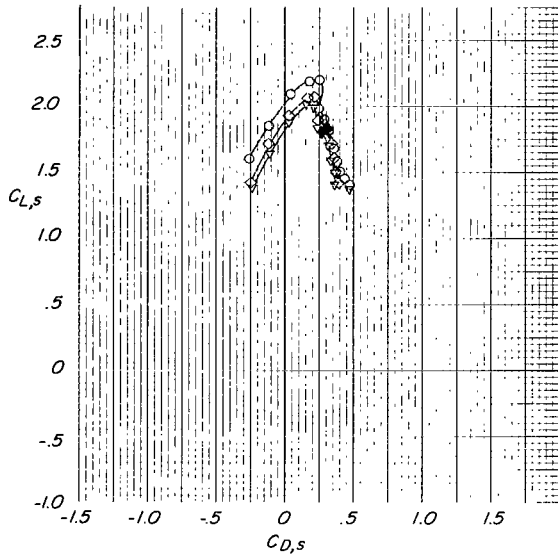


$i_f, \text{deg}$   
 ○ Off  
 □ 10  
 ▼ 20

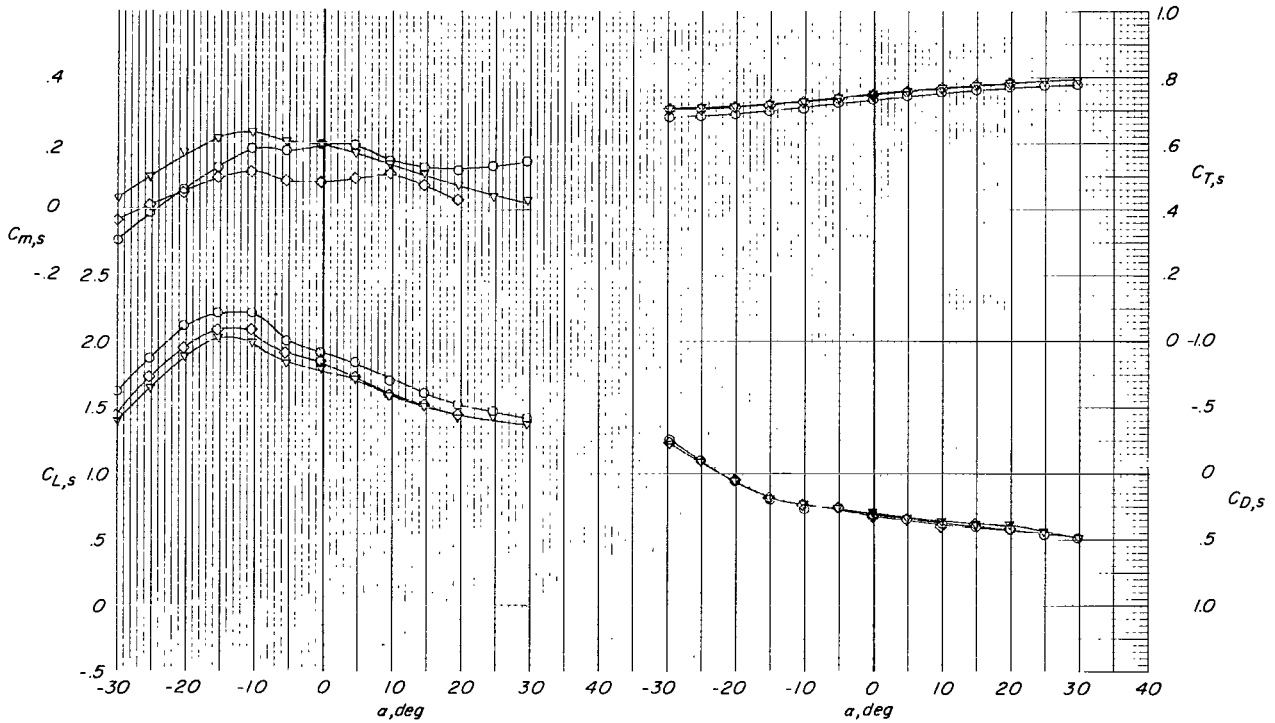


(d)  $(C_{T,s})_{\text{nom}} \approx 0.89$ .

Figure 20.- Concluded.

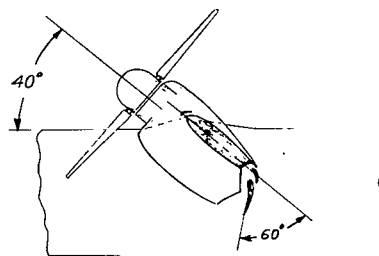
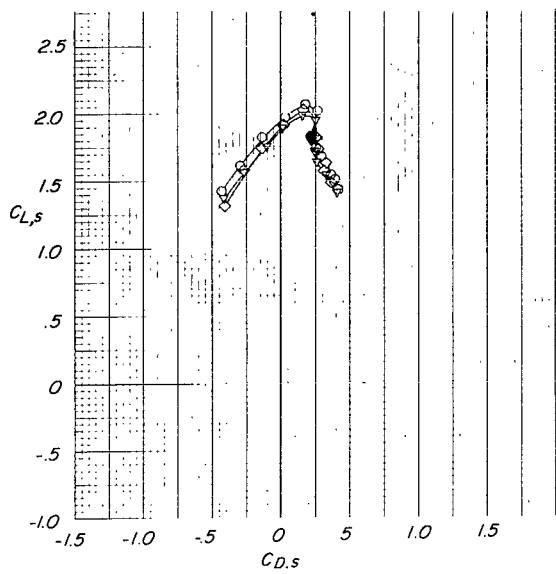


$i_t, \text{deg}$   
 ○ Off  
 ▼ 20  
 ◇ 30

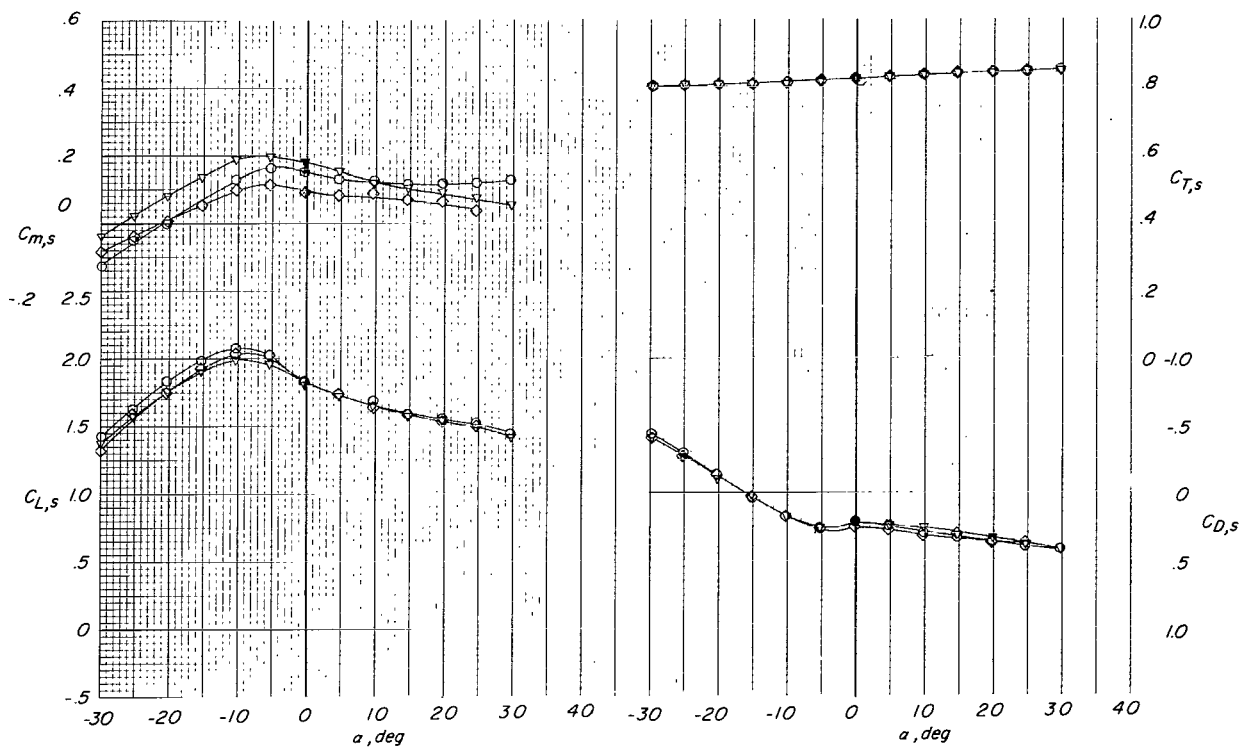


(a)  $(C_{T,s})_{\text{nom}} \approx 0.70$ .

Figure 21.- Effect of horizontal-tail deflection on aerodynamic characteristics of tilt-wing VTOL model at several nominal thrust coefficients.  $S_1$  slat;  $\beta_{.75R} = 12^\circ$ ; 7000 rpm;  $h/\bar{c} = \infty$ ;  $i_w = 40^\circ$ ;  $\delta_f = 60^\circ$ .

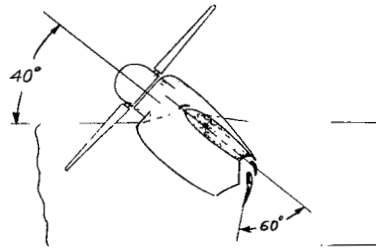
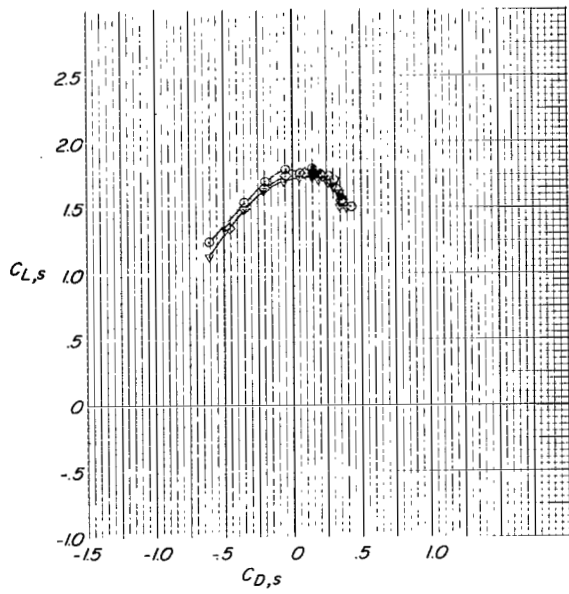


$i_t, \text{deg}$   
 ○ 0  
 ◇ 20  
 ▽ 30

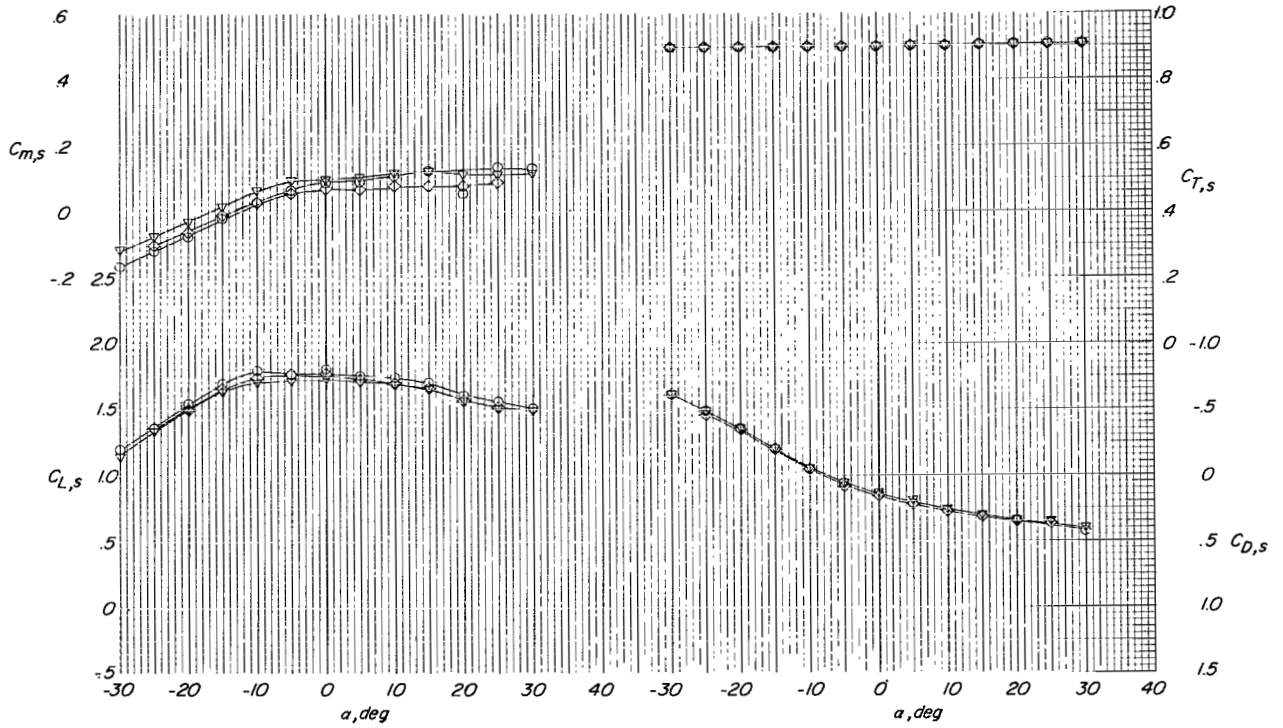


(b)  $(C_{T,s})_{\text{nom}} \approx 0.80$ .

Figure 21.- Continued.

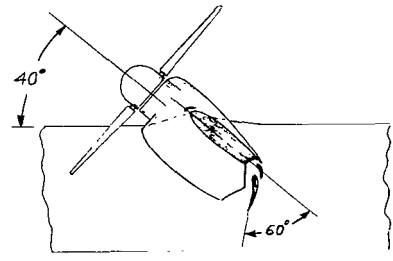
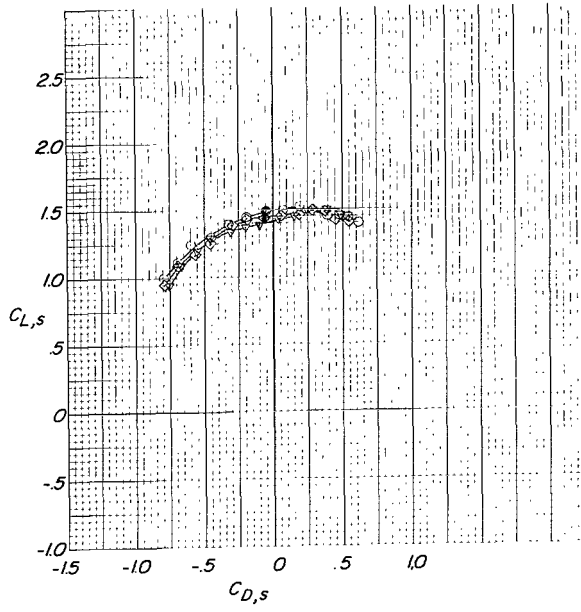


$i_t, \text{deg}$   
 ○ Off  
 ▼ 20  
 ◇ 30

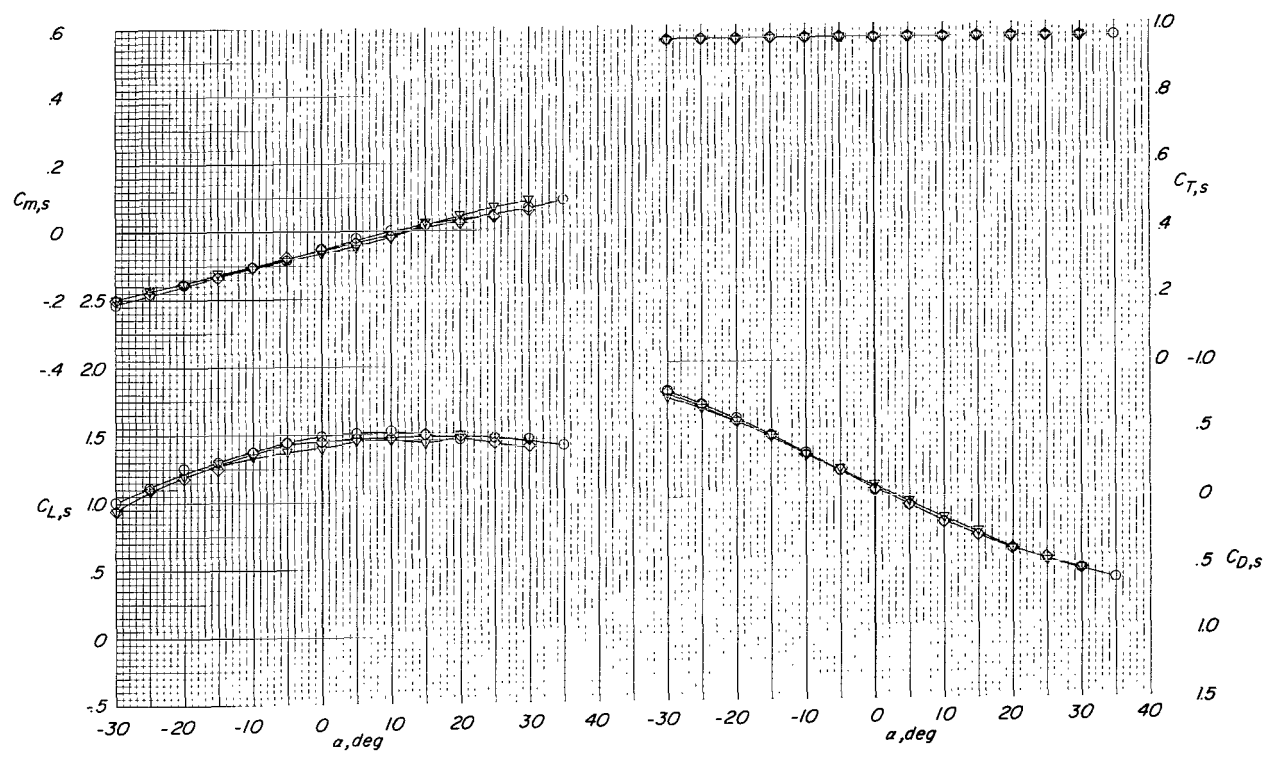


(c)  $(C_{T,s})_{\text{nom}} \approx 0.89$ .

Figure 21.- Continued.

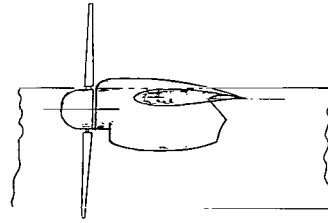
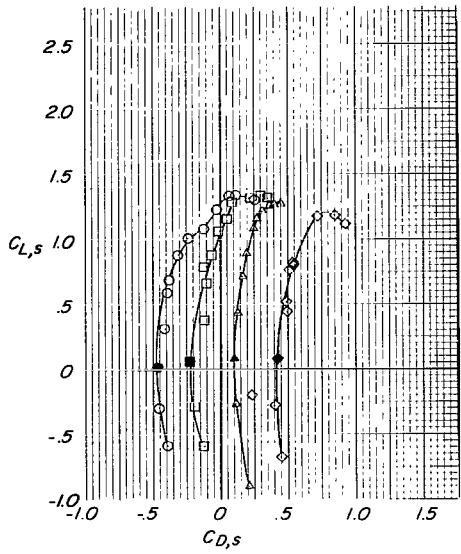


$i_t, \text{deg}$   
 ○ Off  
 ▽ 20  
 ◇ 30



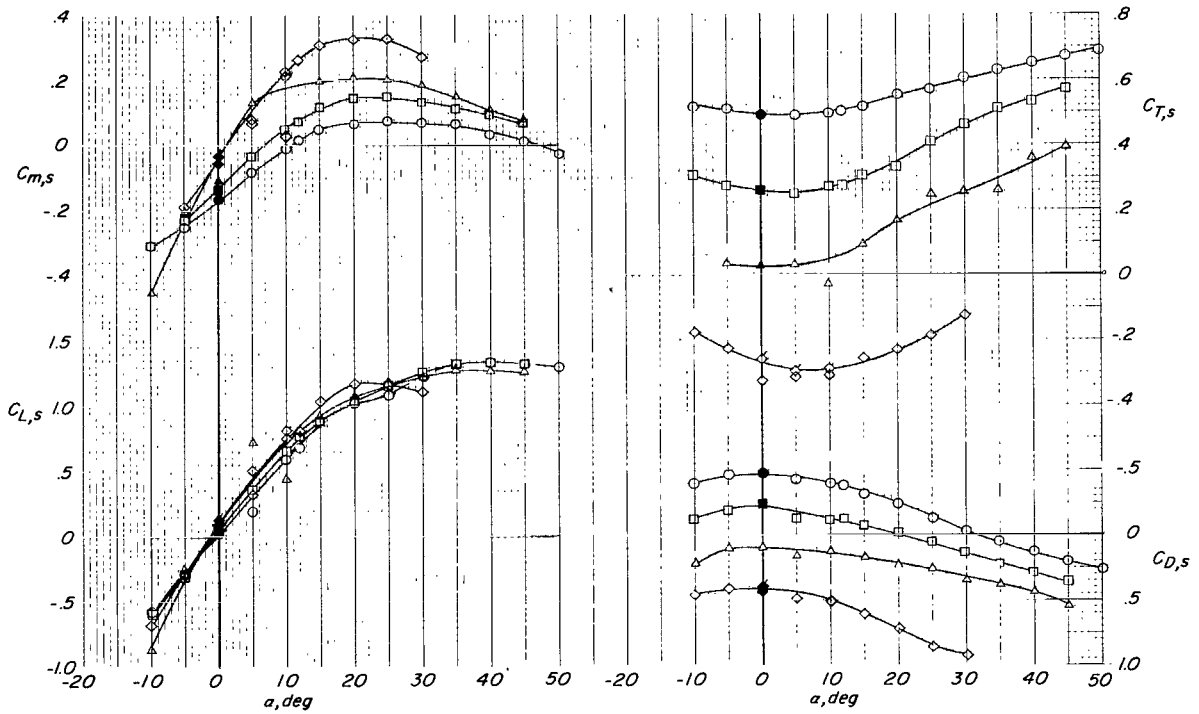
(d)  $(C_{T,s})_{\text{nom}} \approx 0.96$ .

Figure 21.- Concluded.



$(C_{T,s})_{nominal}$

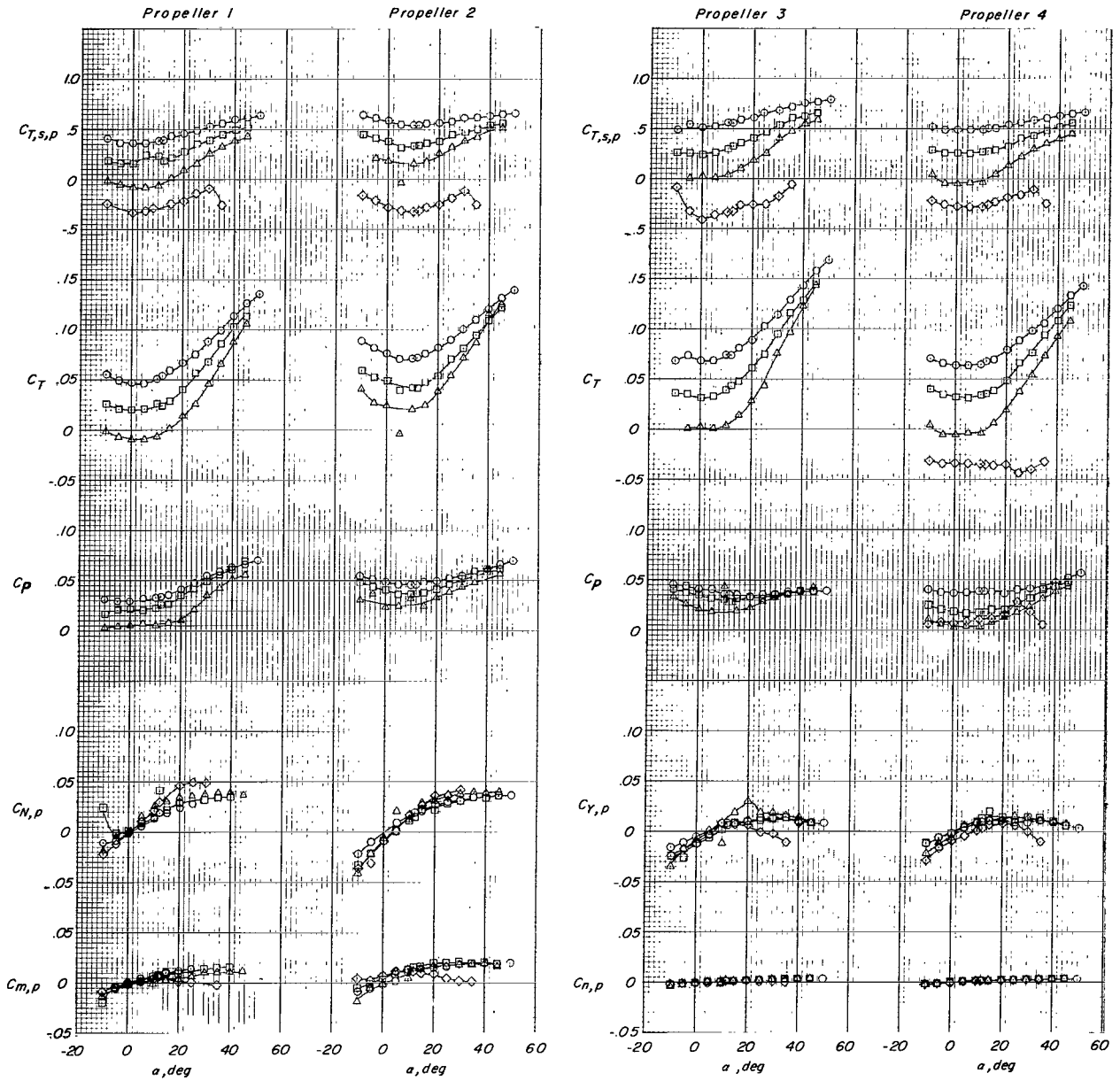
- 49
- 26
- △ 02
- ◇ -26 (Windmilling)



(a)  $i_w = 0^\circ$ ;  $\delta_f = 0^\circ$ ; slat off.

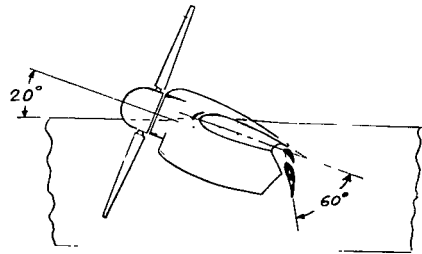
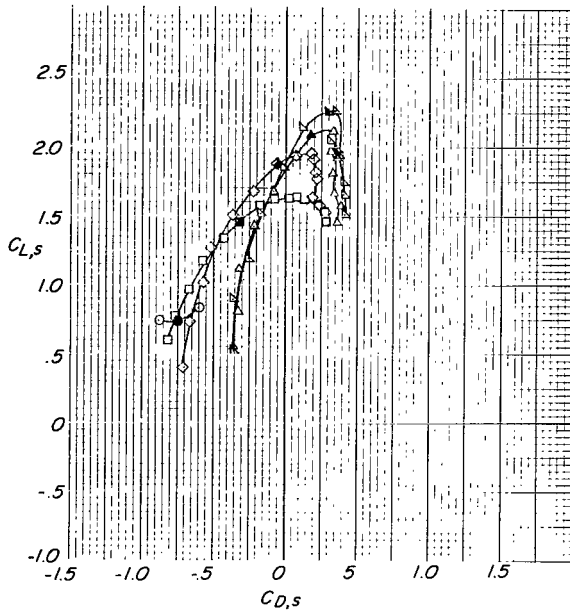
Figure 22.- Aerodynamic characteristics of tilt-wing VTOL model for several wing incidence angles at various nominal thrust coefficients.  $i_t = \text{off}$ ;  $h/\bar{c} = \infty$ ;  $\beta_{.75R} = 12^\circ$ ; 7000 rpm.

- $(C_{T,s})_{nominal}$
- .49
  - .26
  - △ .02
  - ◇ -.26(Windmilling)

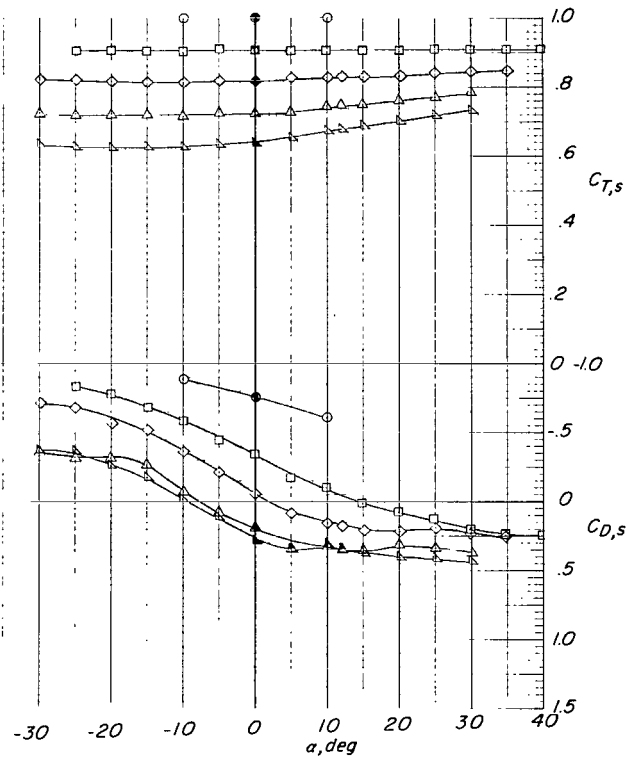
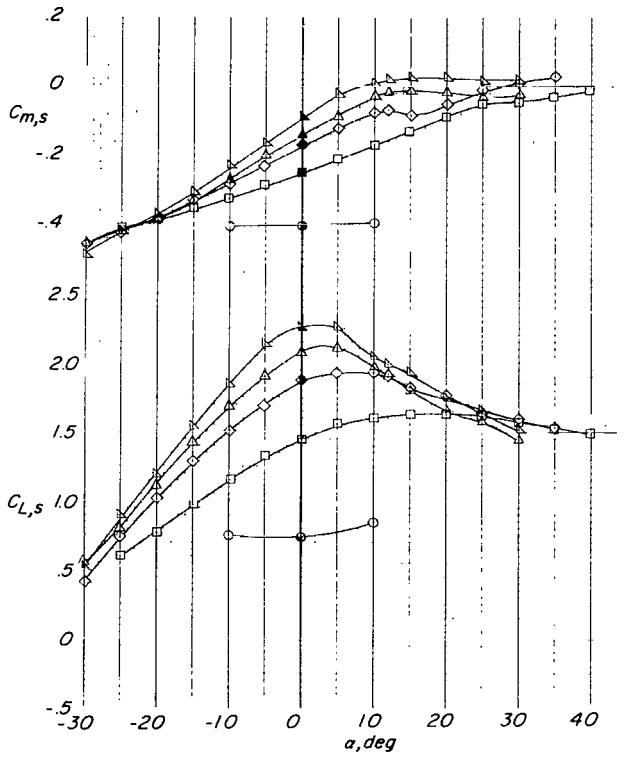


(a) Concluded.

Figure 22.- Continued.

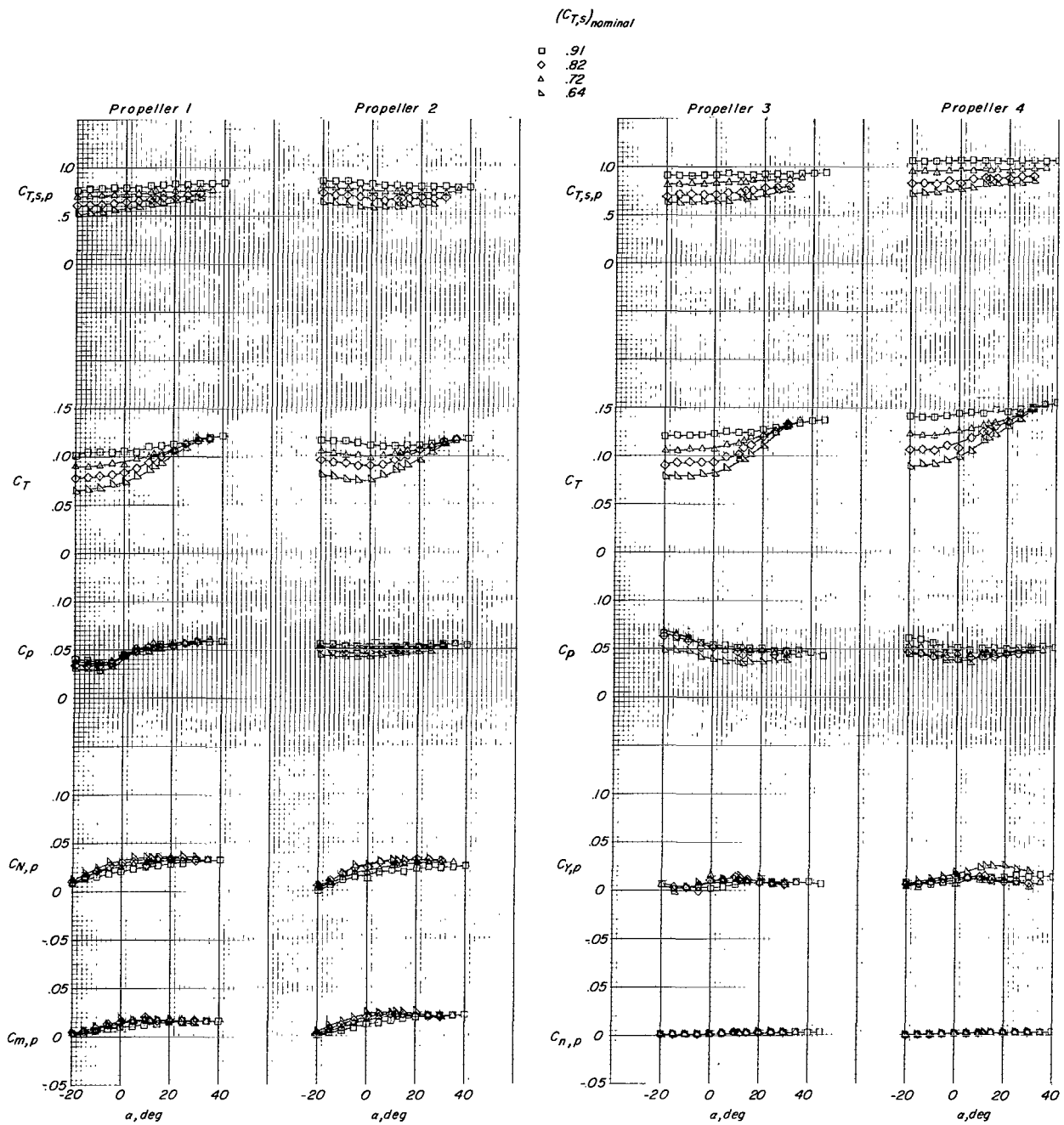


- $(C_{T,s})_{nominal}$
- 1.00
  - .91
  - ◇ .82
  - △ .72
  - ▽ .64



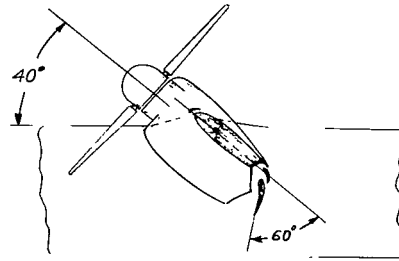
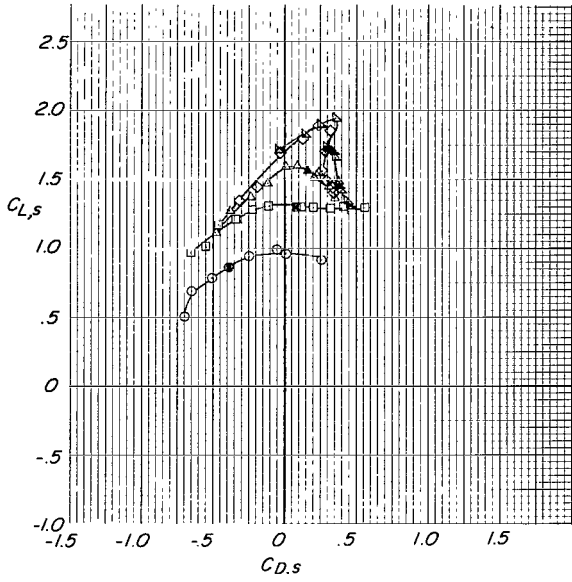
(b)  $i_w = 20^\circ$ ;  $\delta_f = 60^\circ$ ;  $S_1$  slat.

Figure 22.- Continued.

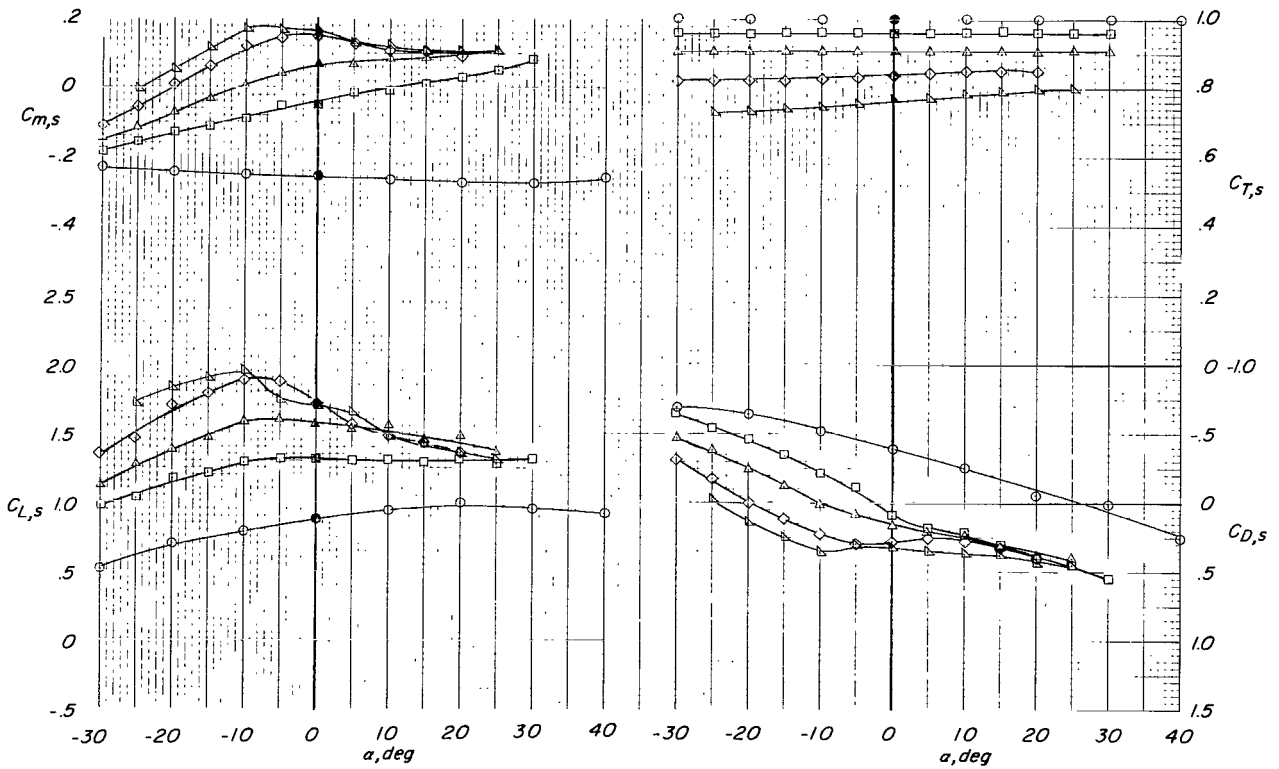


(b) Concluded.

Figure 22.- Continued.



- $(C_{T,s})_{nominal}$
- 1.00
  - .96
  - △ .91
  - ◇ .84
  - ▽ .76

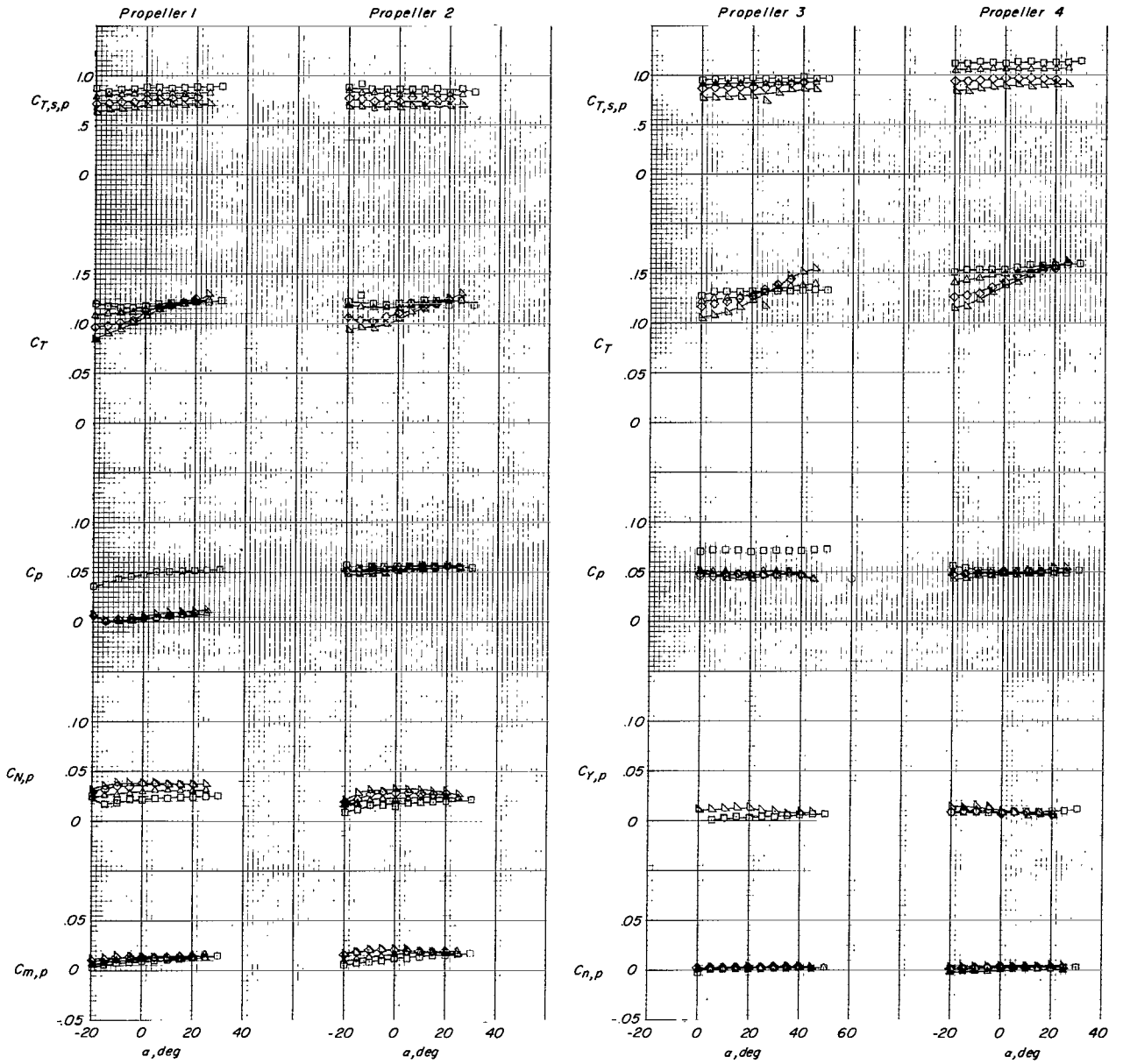


(c)  $i_w = 40^\circ$ ;  $\delta_f = 60^\circ$ ;  $S_1$  slat.

Figure 22.- Continued.

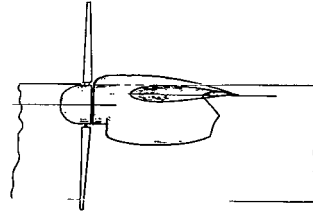
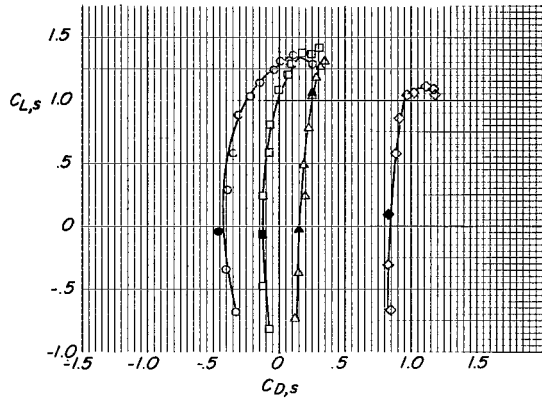
$(C_{T,s})_{nominal}$

- .96
- △ .91
- ◇ .84
- ▽ .76

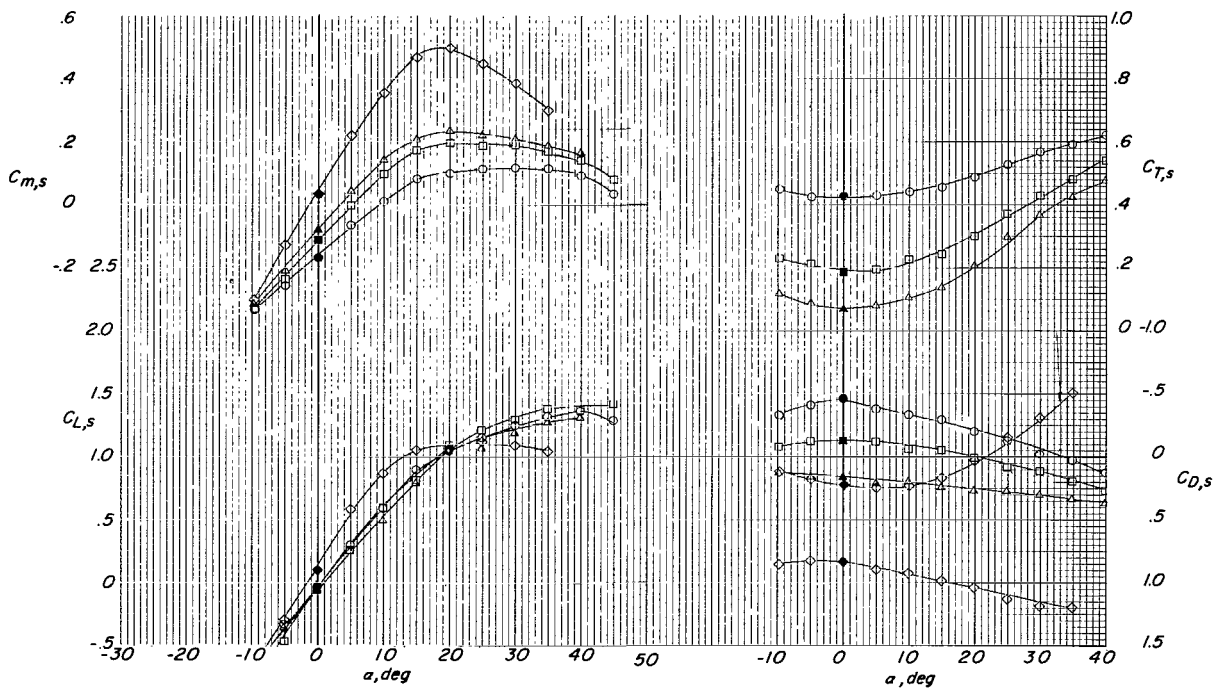


(c) Concluded.

Figure 22.- Concluded.



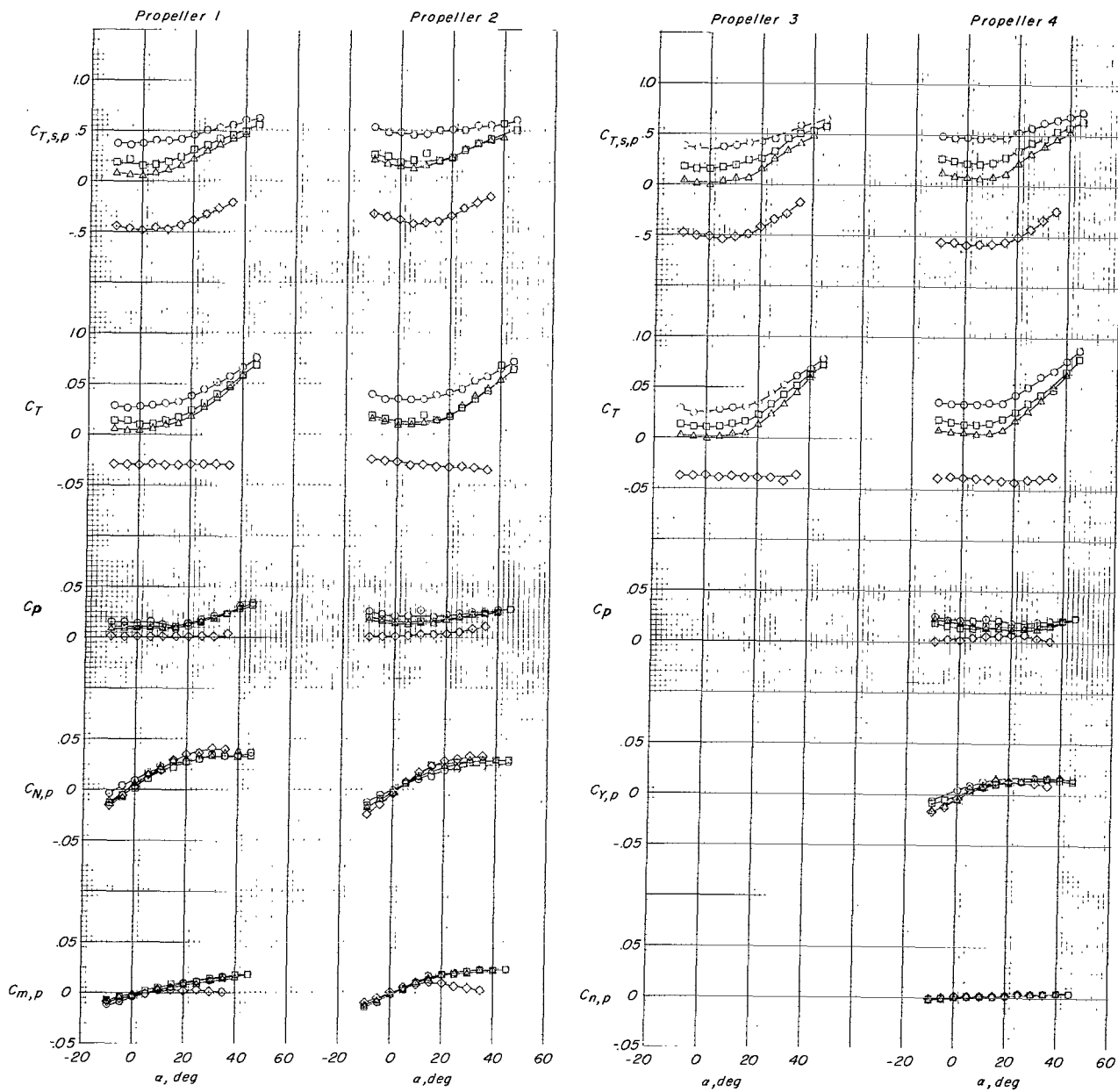
- $(C_{T,s})_{nominal}$
- .42
  - .19
  - △ .07
  - ◇ -.49 (Windmilling)



(a)  $i_w = 0^\circ$ ;  $\delta_f = 0^\circ$ ; slat off.

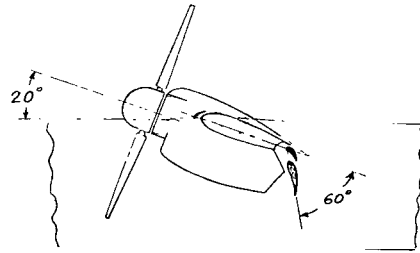
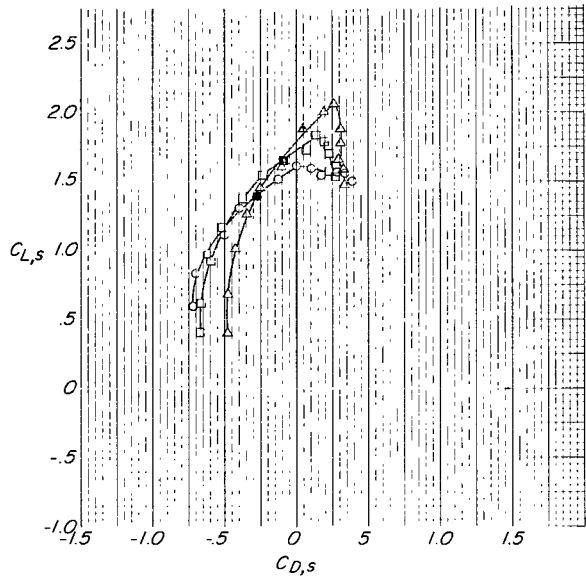
Figure 23.- Aerodynamic characteristics of tilt-wing VTOL model for several wing-incidence angles at various nominal thrust coefficients.  $i_t = \text{off}$ ;  $h/\bar{c} = \infty$ ;  $\beta_{.75R} = 8^\circ$ ; 7000 rpm.

$(C_{T,S})_{nominal}$   
 ○ .42  
 □ .19  
 △ .07  
 ◇ -.49(Windmilling)

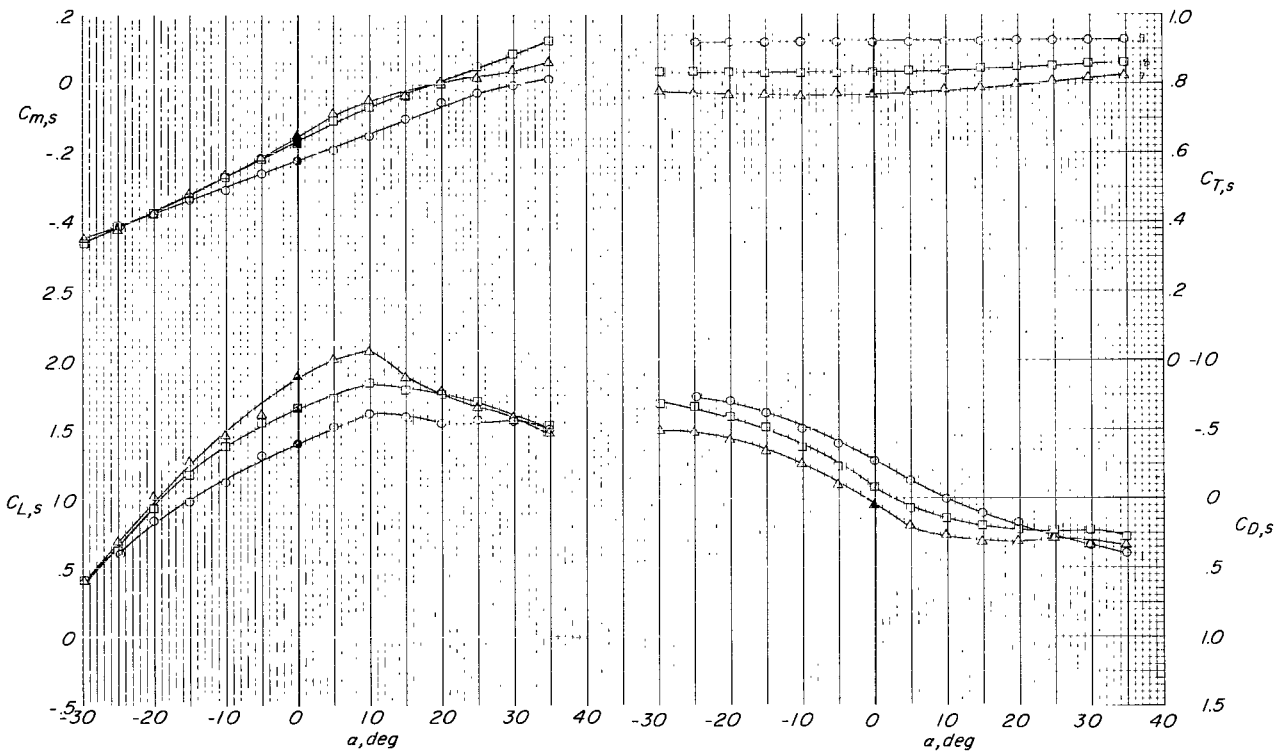


(a) Concluded.

Figure 23.- Continued.



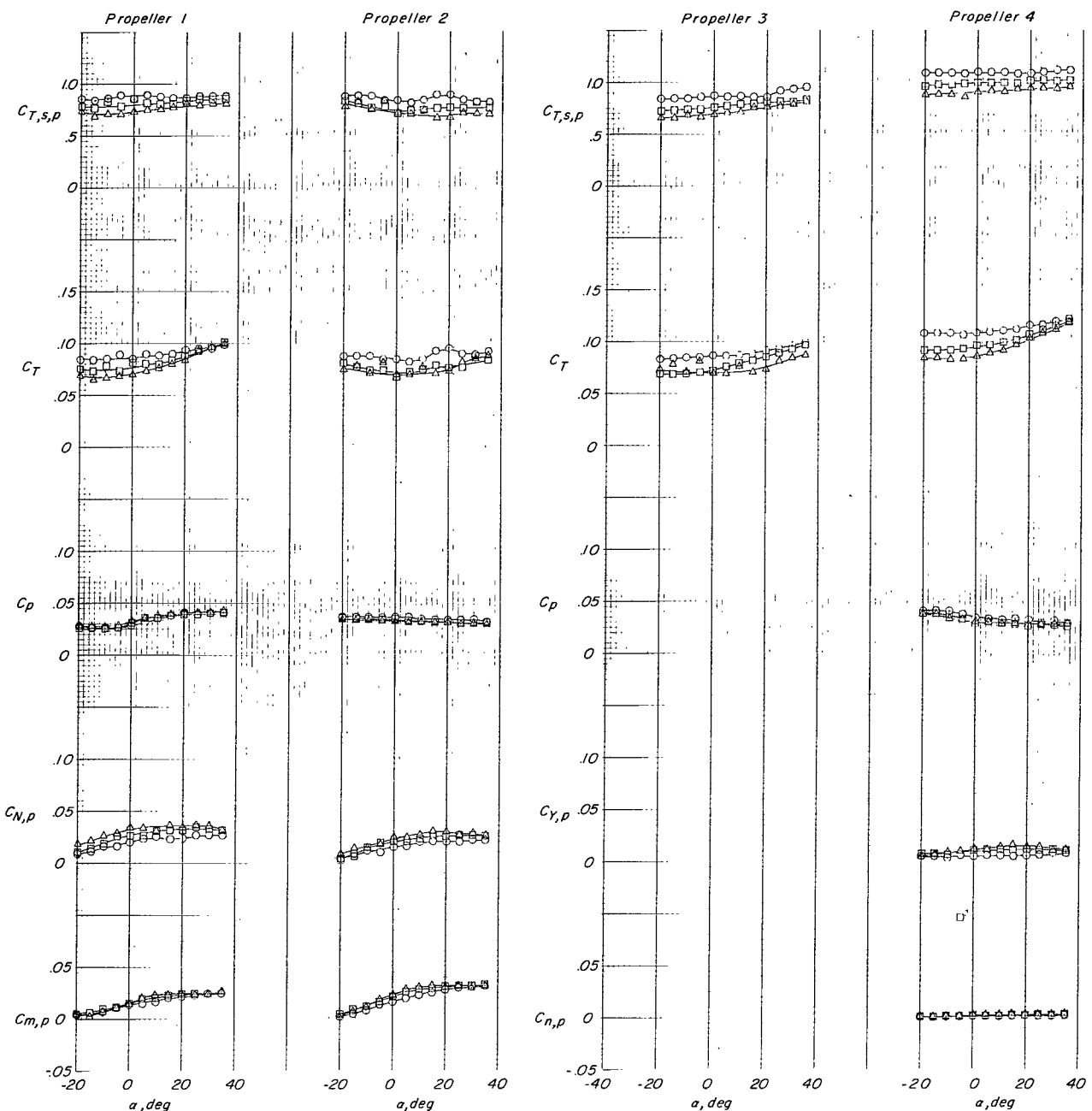
$(C_{T,s})_{nominal}$   
 ○ .92  
 □ .83  
 △ .77



(b)  $i_w = 20^\circ$ ;  $\delta_f = 60^\circ$ ;  $S_1$  slat.

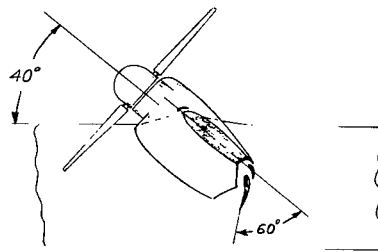
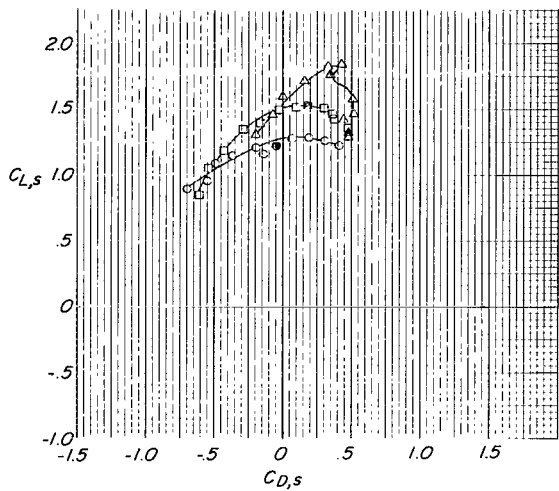
Figure 23.- Continued.

$(C_{T,s})_{nominal}$   
 ○ .92  
 □ .83  
 △ .77

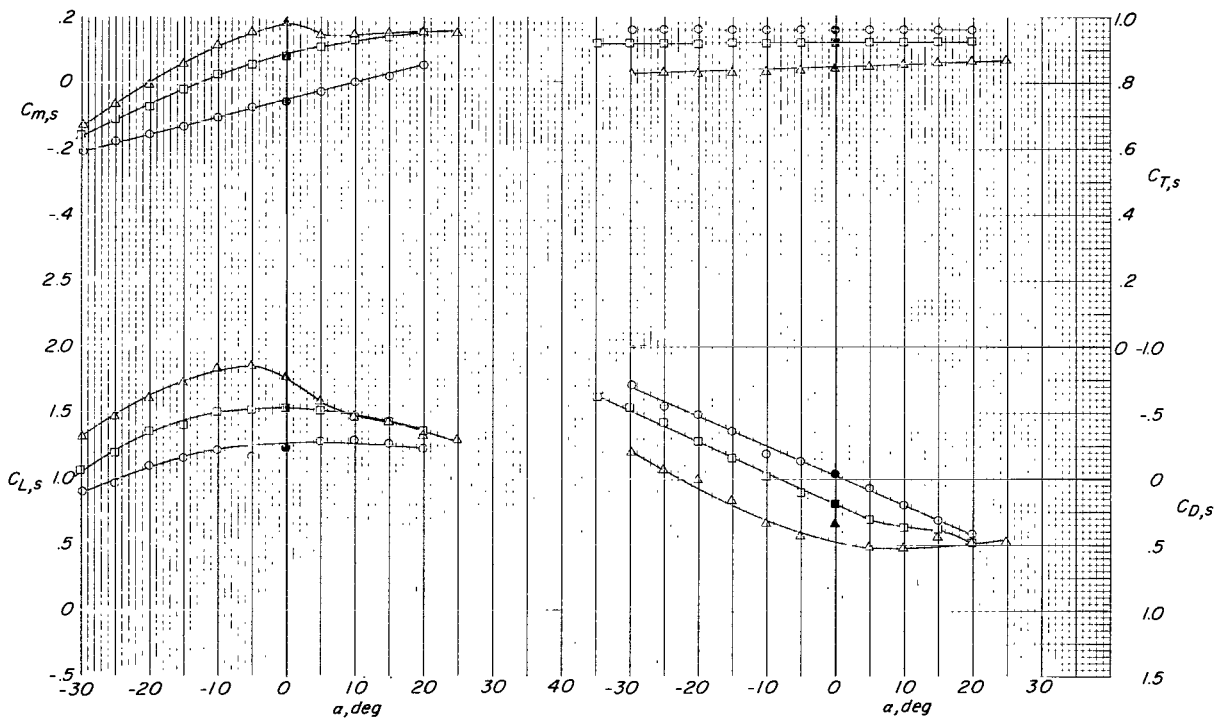


(b) Concluded.

Figure 23.- Continued.



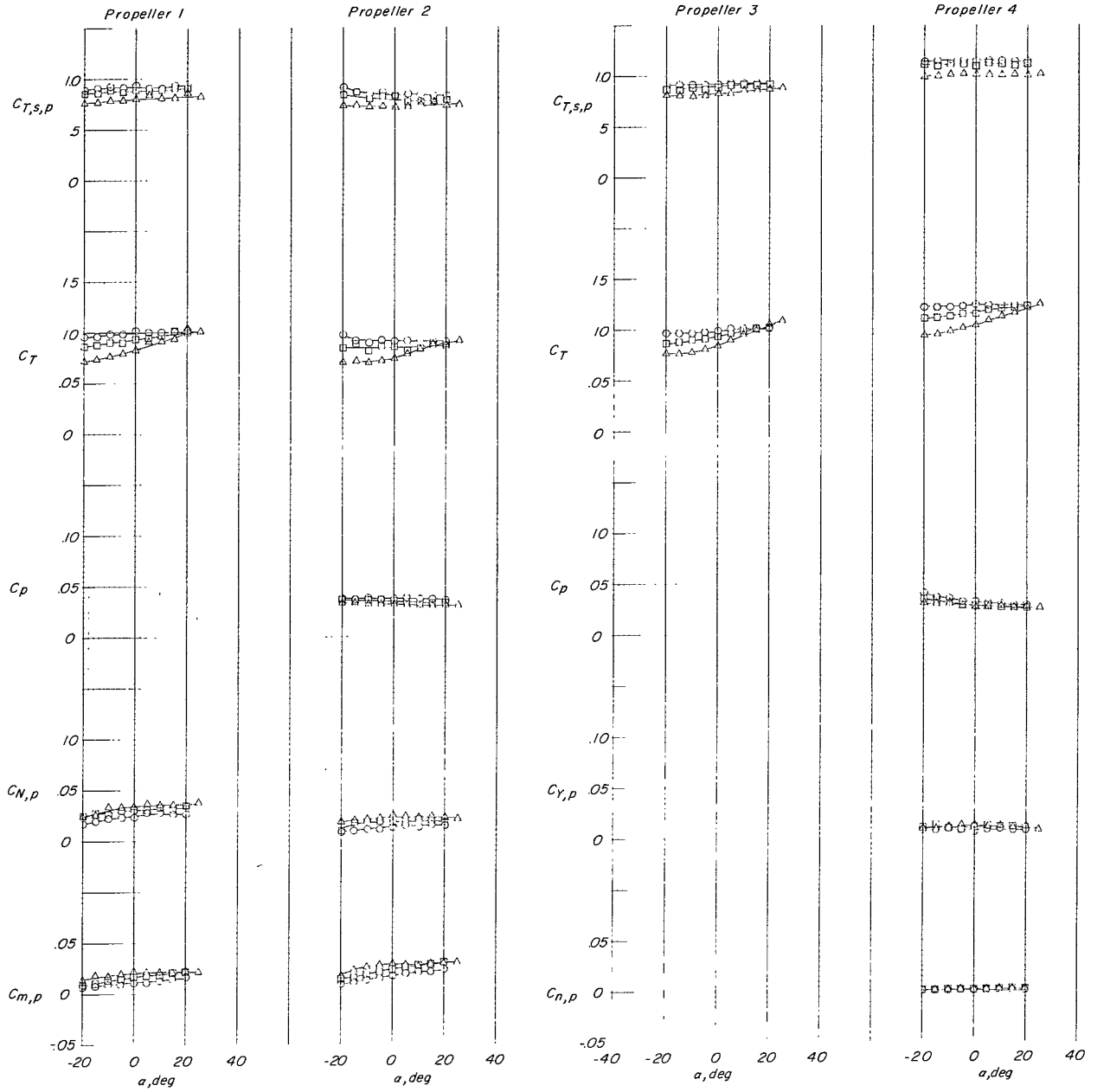
$(C_{T,s})_{nominal}$   
 ○ .96  
 □ .92  
 △ .85



(c)  $i_w = 40^\circ$ ;  $\delta_f = 60^\circ$ ;  $S_1$  slat.

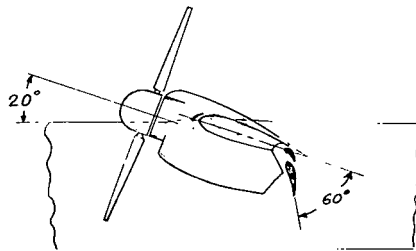
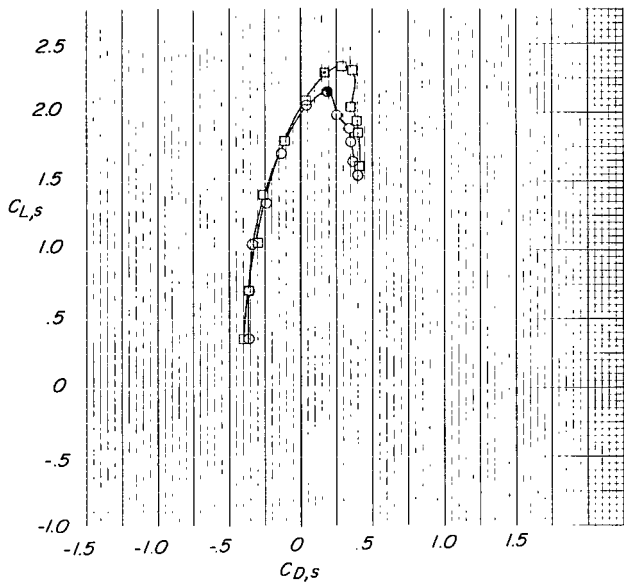
Figure 23.- Continued.

$(C_{T,s})_{nominal}$   
 ○ .96  
 □ .92  
 △ .85

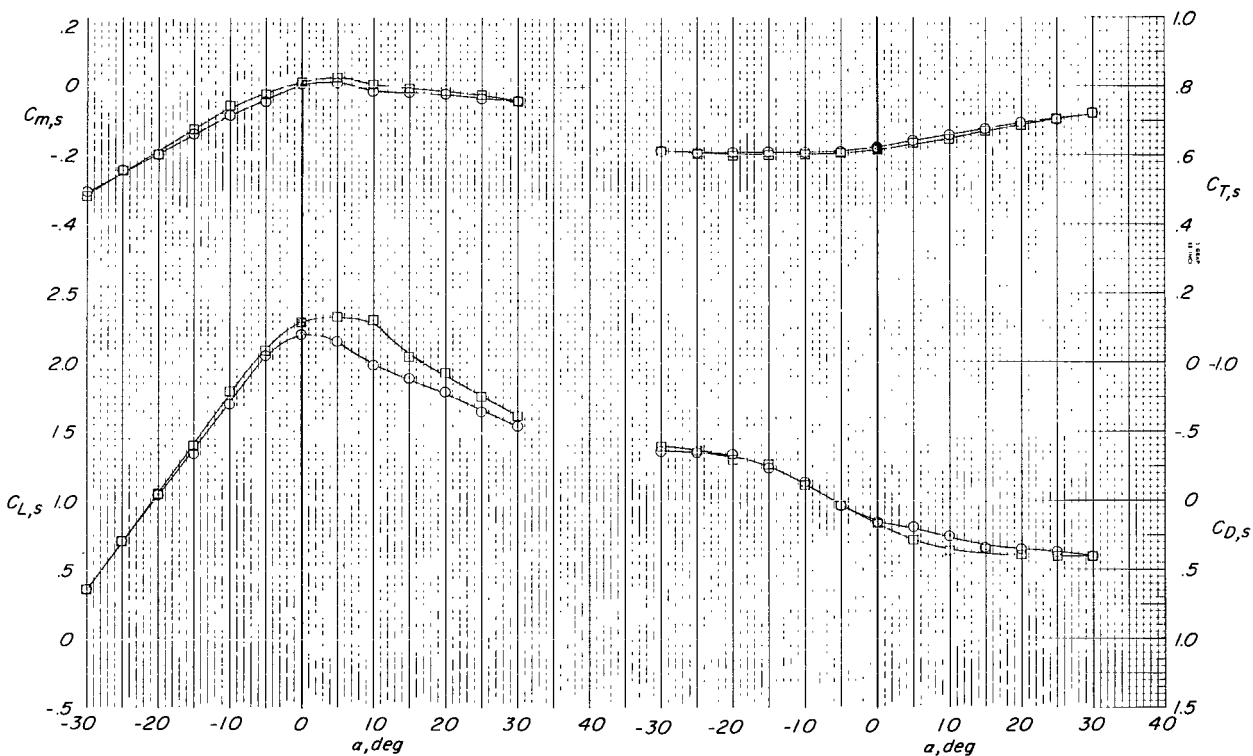


(c) Concluded.

Figure 23.- Concluded.

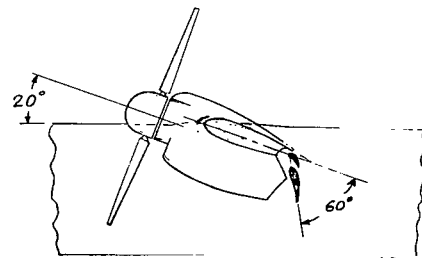
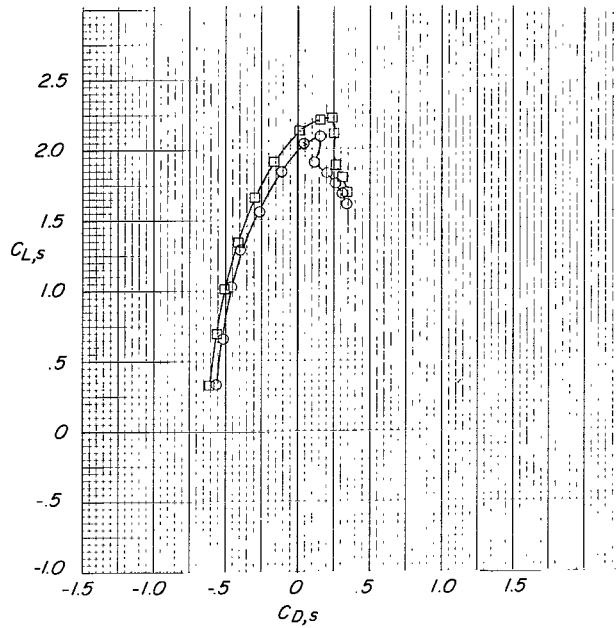


Slat  
 ○  $S_1$   
 □  $S_2$

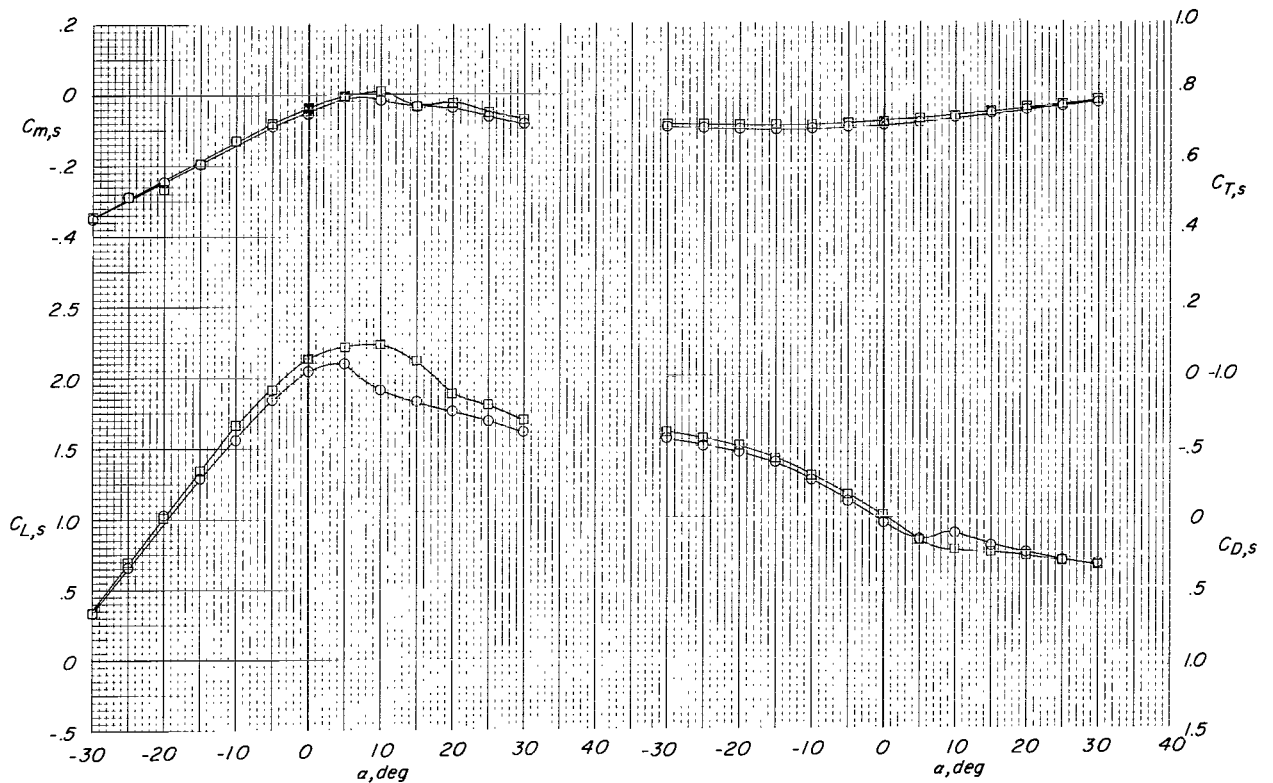


(a)  $(C_{T,s})_{\text{nom}} \approx 0.62$ .

Figure 24.- Comparison of aerodynamic characteristics of a tapered nacelle to propeller tip slat ( $S_1$ ) and a nacelle to nacelle slat ( $S_2$ ) on a tilt-wing VTOL model at various nominal thrust coefficients.  $i_w = 20^\circ$ ;  $i_t = 10^\circ$ ;  $\delta_f = 60^\circ$ ;  $\beta_{.75R} = 12^\circ$ ; 7000 rpm;  $h/\bar{c} = \infty$ .

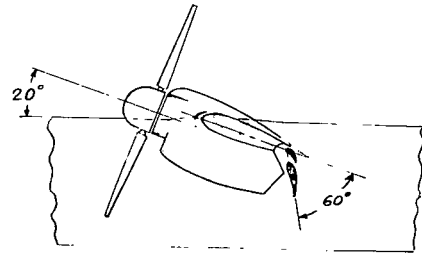
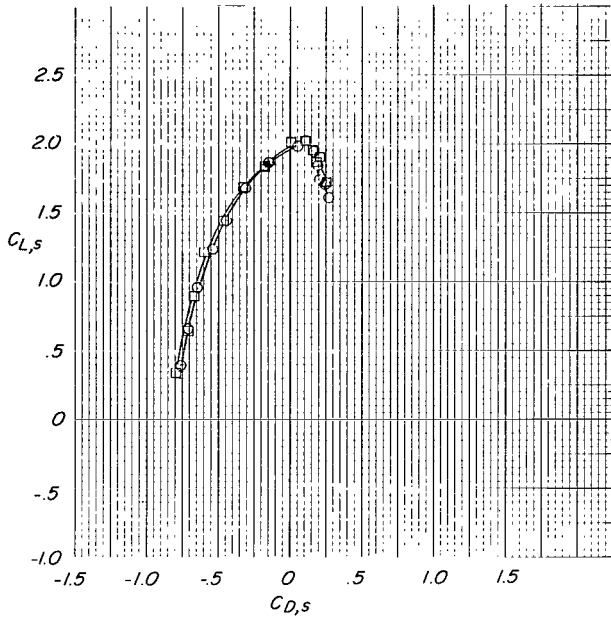


Slat  
 ○  $S_1$   
 □  $S_2$

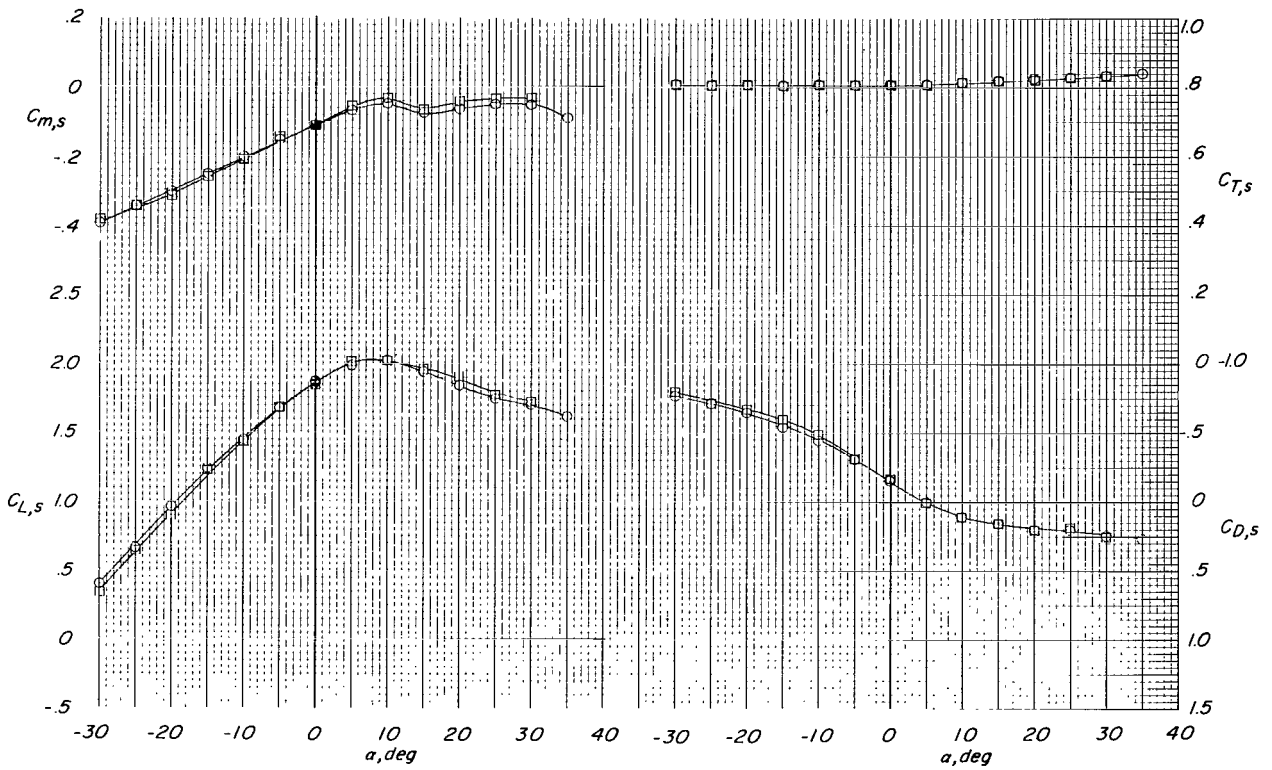


(b)  $(C_{T,s})_{\text{nom}} \approx 0.70$ .

Figure 24.- Continued.

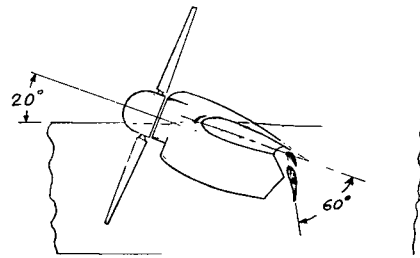
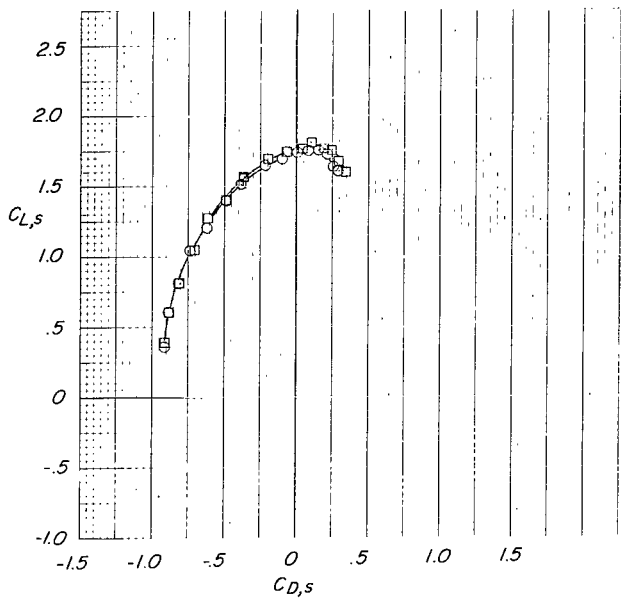


Slat  
 ○  $S_1$   
 □  $S_2$

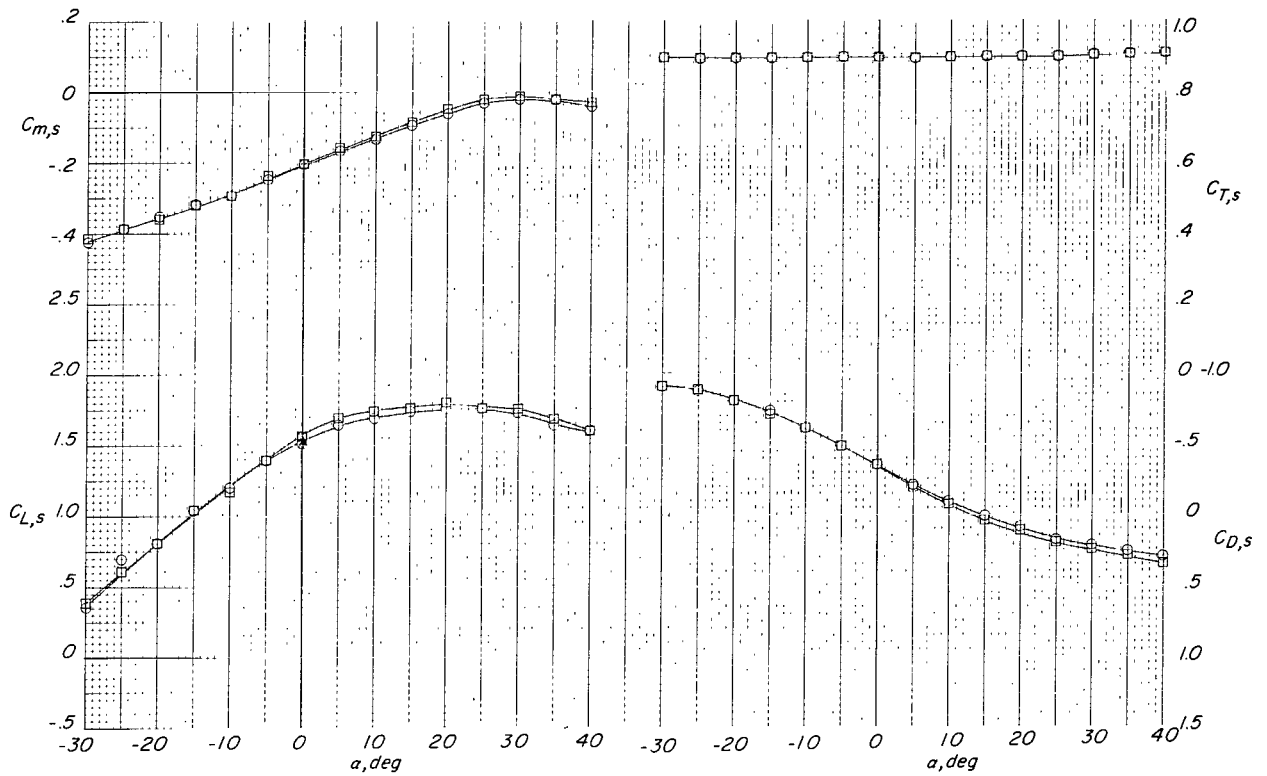


(c)  $(C_{T,s})_{nom} \approx 0.80$ .

Figure 24.- Continued.

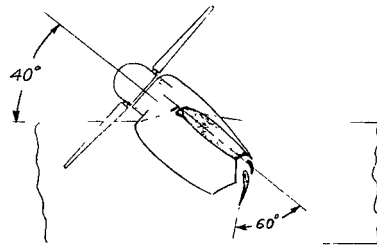
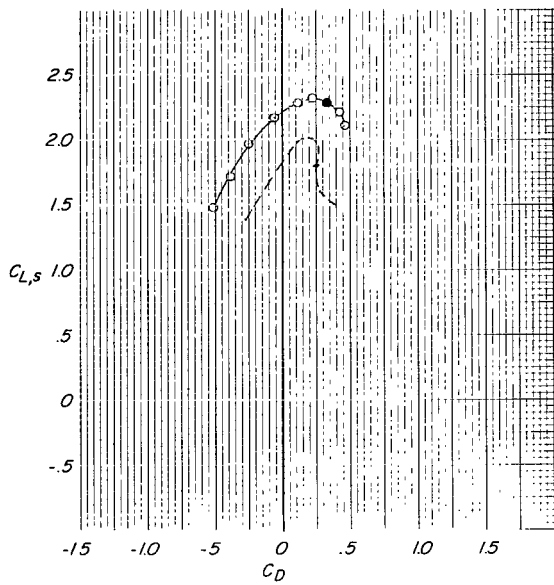


Slat  
 ○  $S_1$   
 □  $S_2$

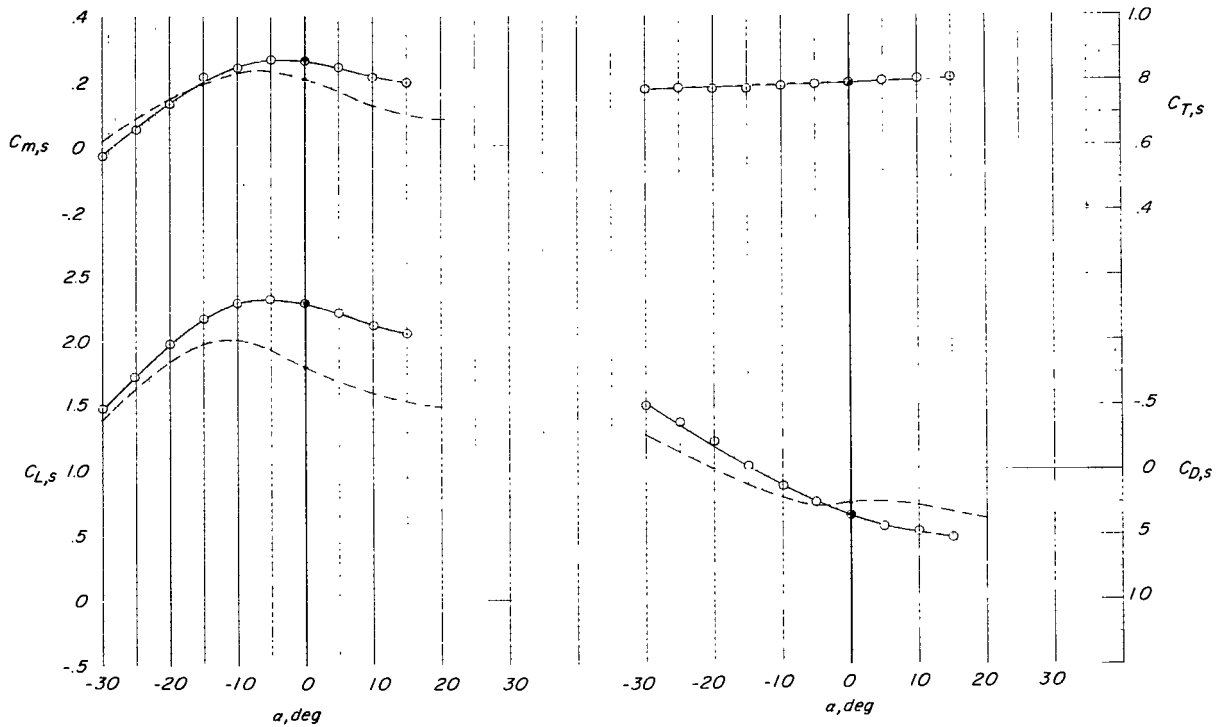


(d)  $(C_{T,s})_{\text{nom}} \approx 0.89$ .

Figure 24.- Concluded.

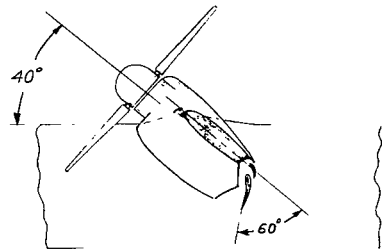
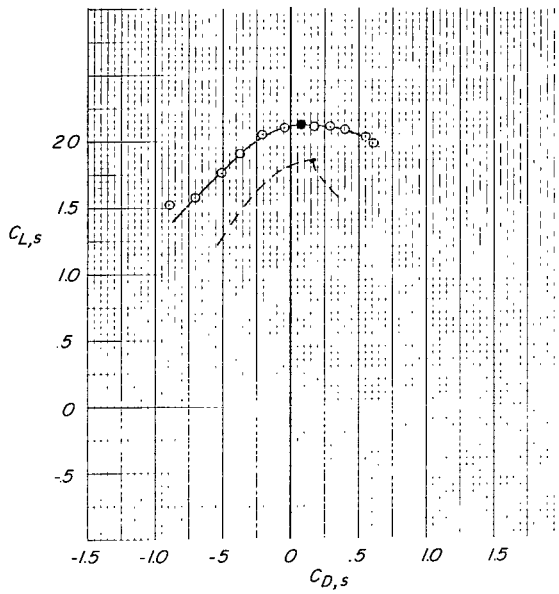


Chord extension  
 ○ On  
 --- Off

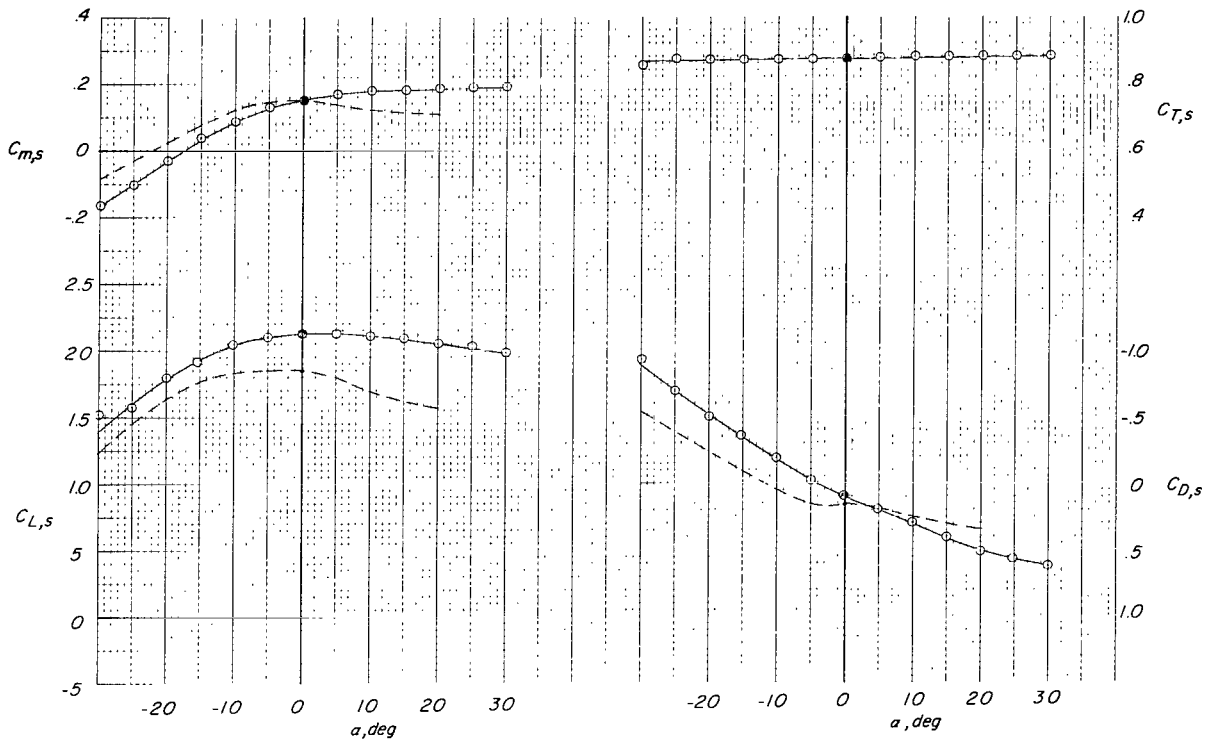


(a)  $(C_{T,s})_{nom} \approx 0.79$ .

Figure 25.- Effect of adding a 10-percent chord extension with  $10^\circ$  droop (fig. 9) to basic tilt-wing VTOL model configuration.  $i_w = 40^\circ$ ;  $i_t = 20^\circ$ ;  $\delta_f = 60^\circ$ ;  $S_1$  slat;  $\beta_{75R} = 12^\circ$ ; 7000 rpm;  $h/\bar{c} = \infty$ .

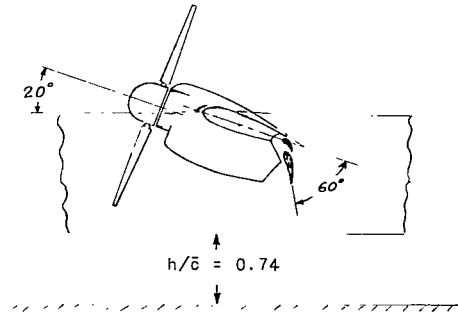
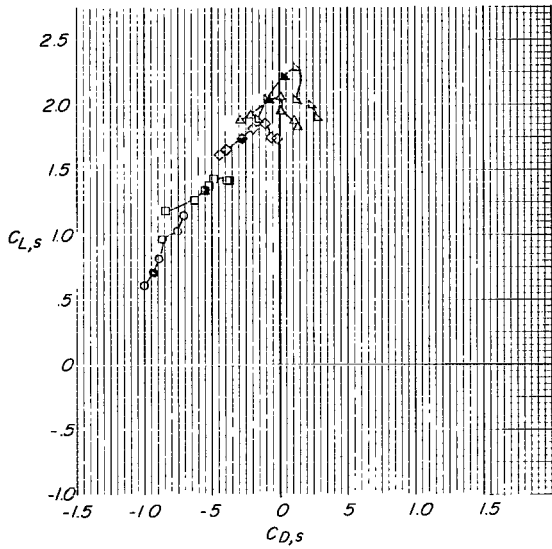


Chord extension  
 ○ On  
 --- Off

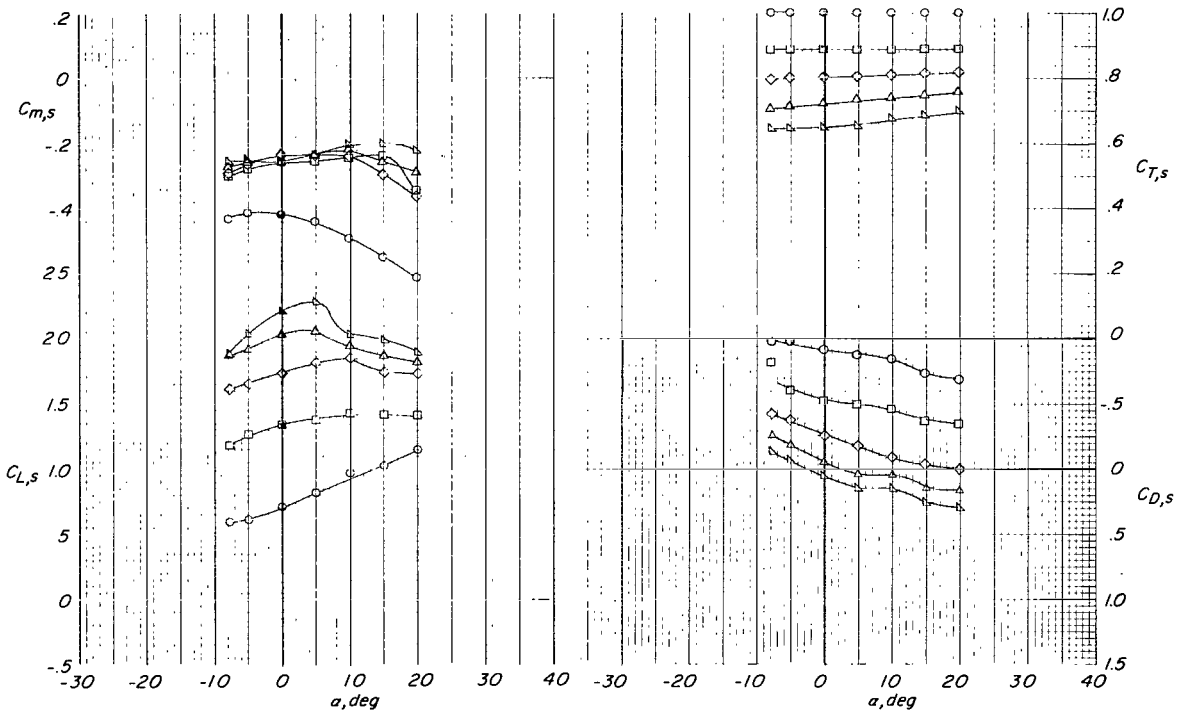


(b)  $(C_{T,s})_{\text{nom}} \approx 0.87$ .

Figure 25.- Concluded.



- $(C_{T,s})_{nominal}$
- 1.00
  - 0.89
  - ◇ 0.80
  - △ 0.72
  - ▽ 0.65

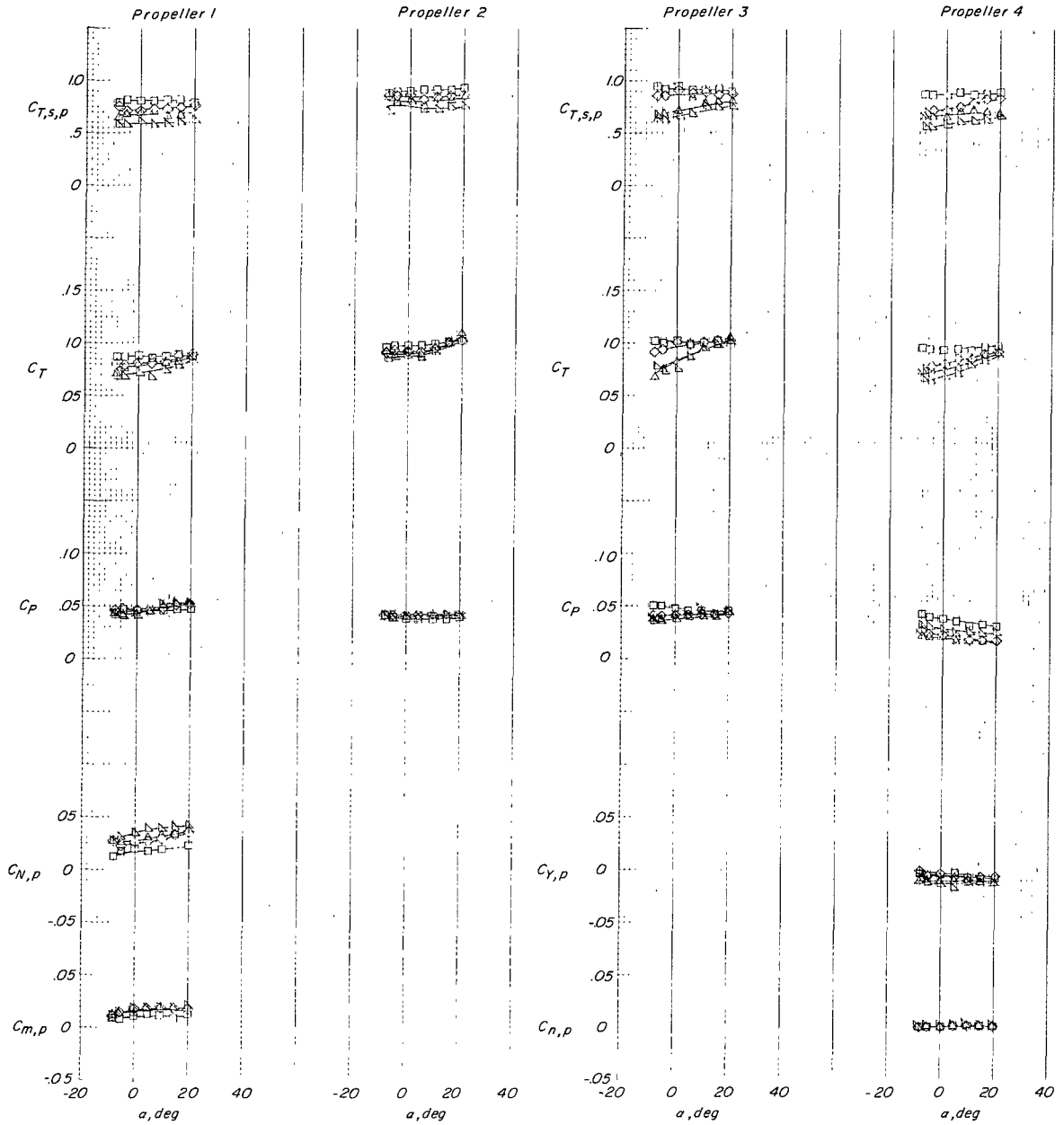


(a)  $i_w = 20^\circ$ .

Figure 26.- Aerodynamic characteristics of tilt-wing VTOL model for several wing incidence angles at various nominal thrust coefficients.  $S_1$  slat;  $\beta_{75R} = 12^\circ$ ; 7500 rpm;  $h/\bar{c} = 0.74$ ;  $i_t = 20^\circ$ ;  $\delta_f = 60^\circ$ .

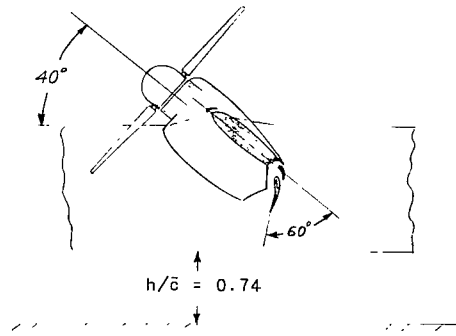
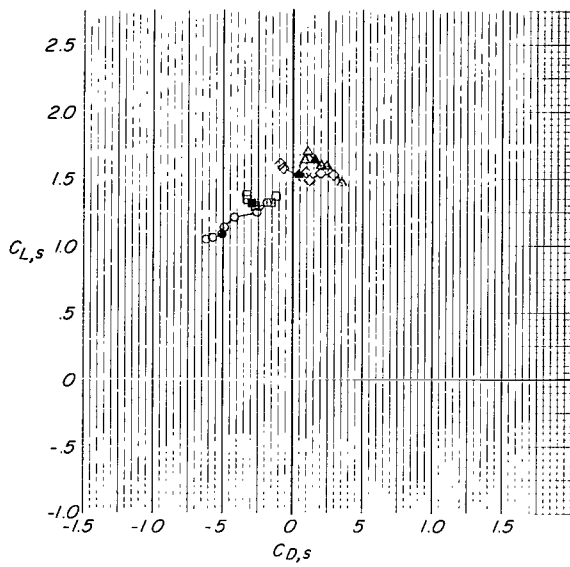
$(C_{T,s})_{nominal}$

- .89
- ◇ .80
- △ .72
- ▽ .65

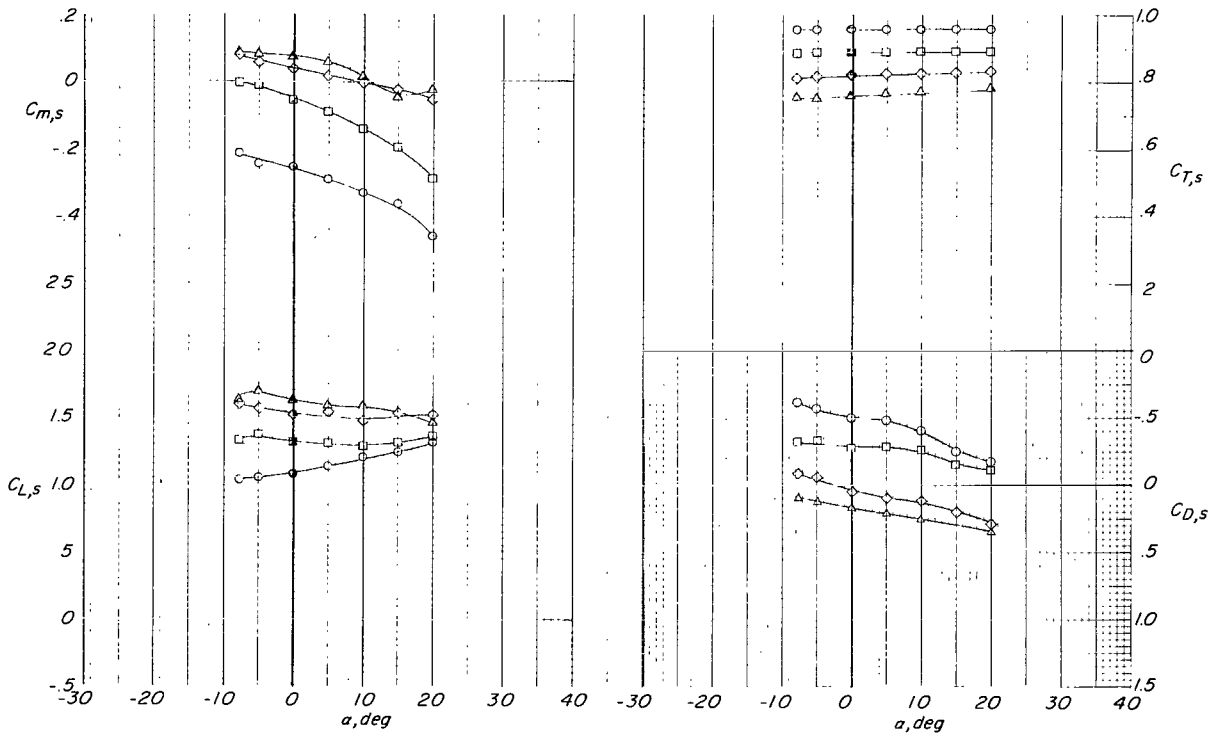


(a) Concluded.

Figure 26.- Continued.



- $(C_{T,s})_{nominal}$
- .96
  - .89
  - ◇ .82
  - △ .76

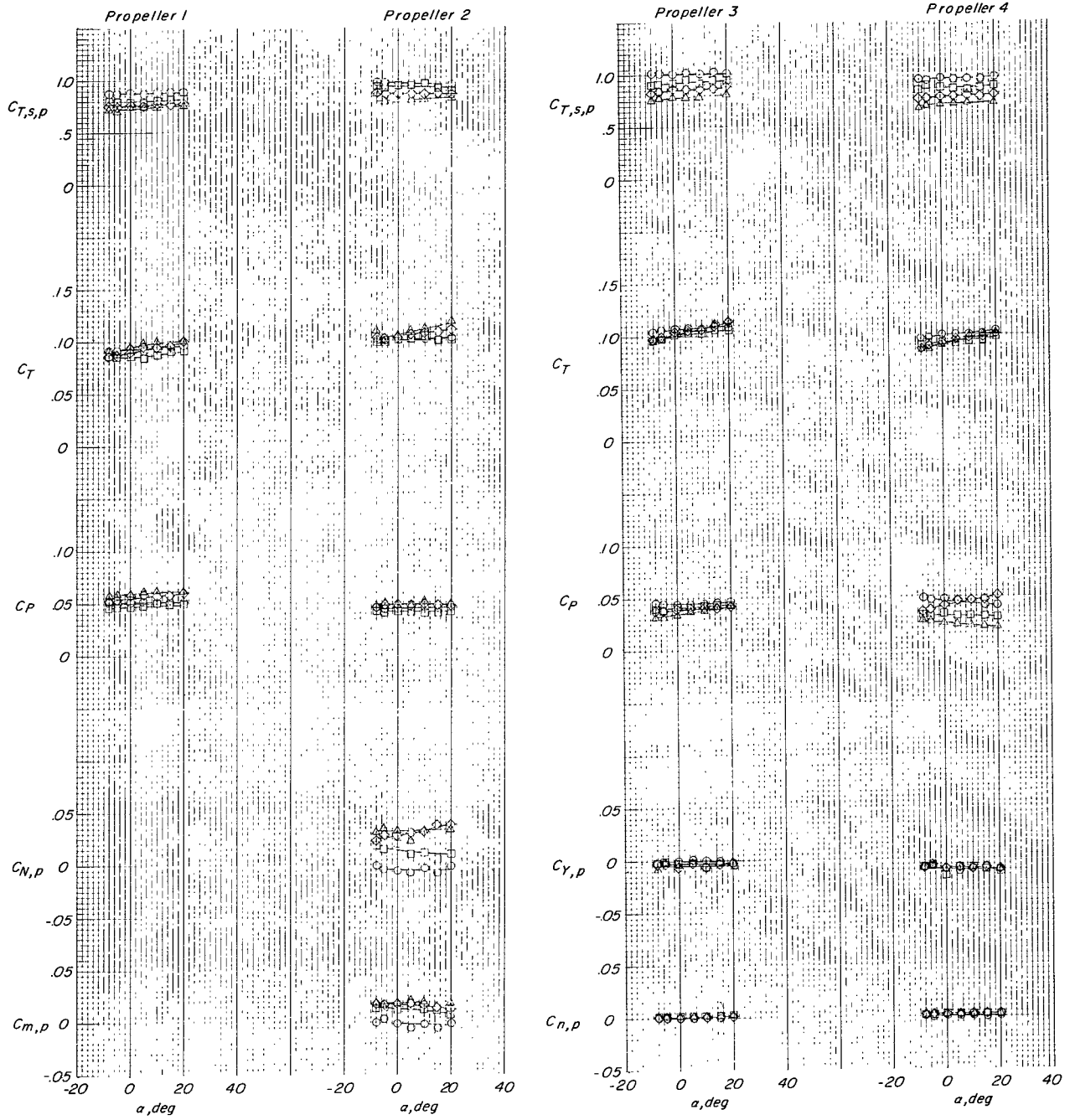


(b)  $i_w = 40^\circ$ .

Figure 26.- Continued.

$(C_{T,s})_{nominal}$

- .96
- .89
- ◇ .82
- △ .76



(b) Concluded.

Figure 26.- Concluded.

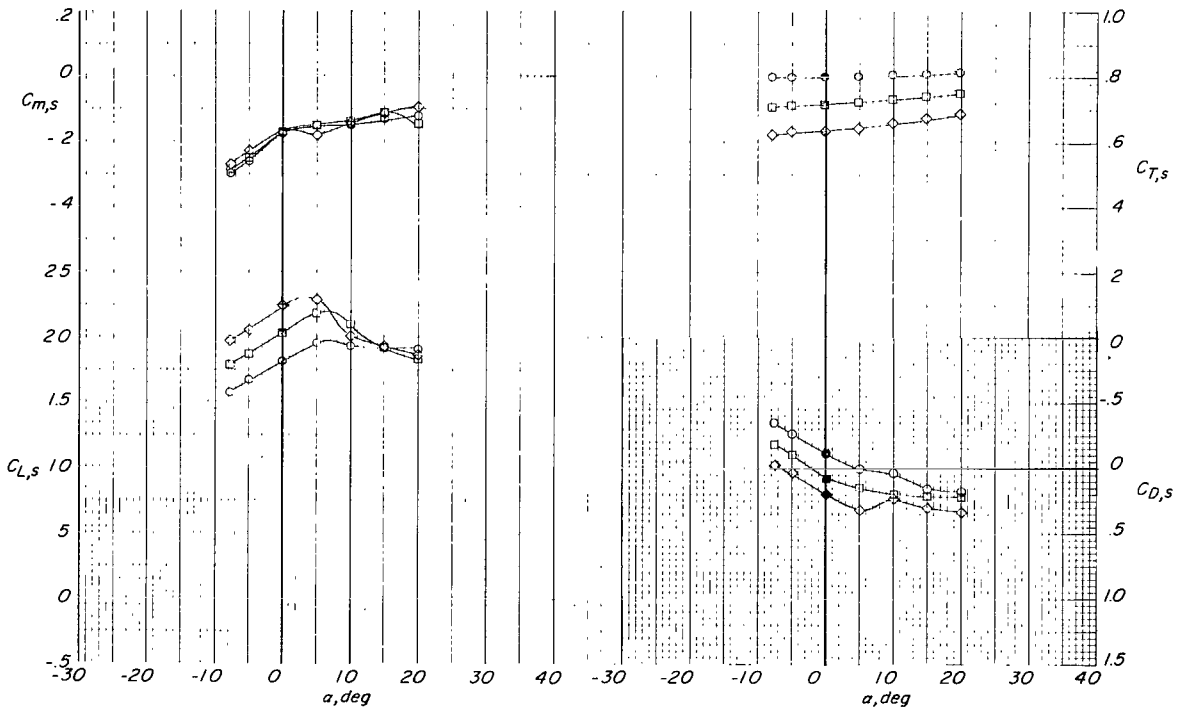
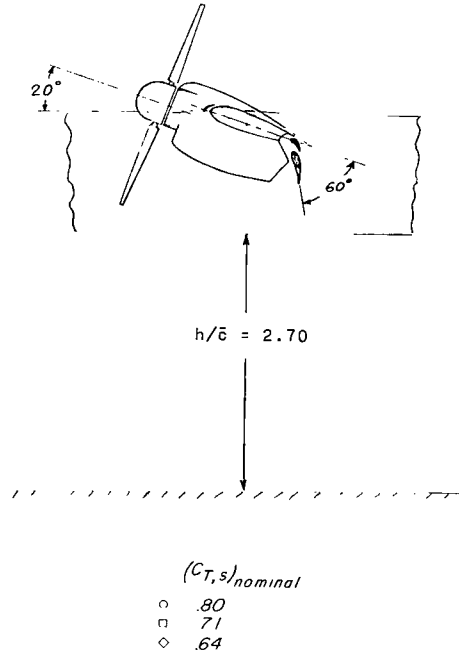
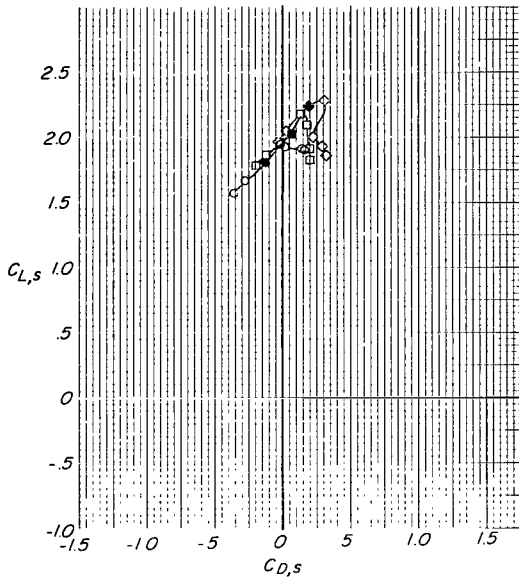
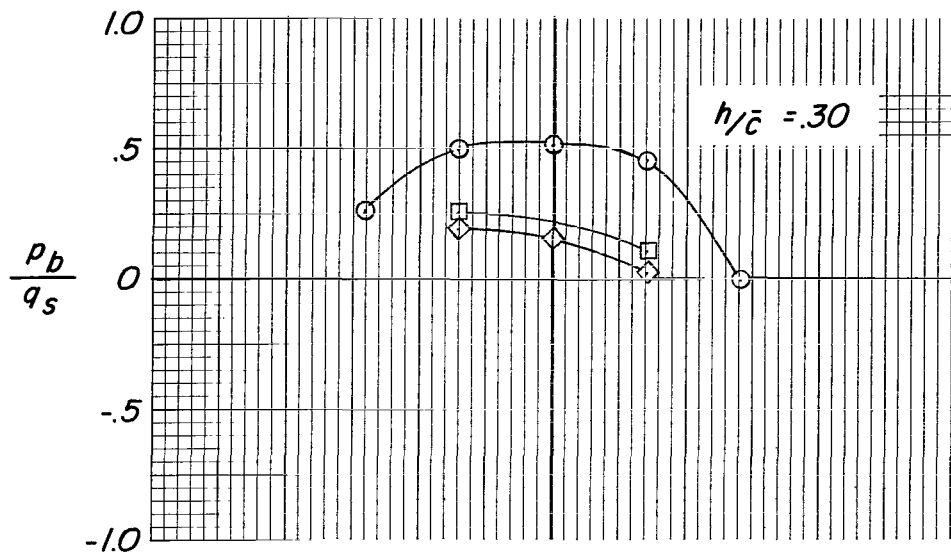


Figure 27.- Aerodynamic characteristics of tilt-wing VTOL model with and without inboard nacelle nose-down droop at various thrust coefficients.  $\delta_f = 60^\circ$ ;  $i_w = 20^\circ$ ;  $i_t = 20^\circ$ ;  $S_1$  slat;  $h/\bar{c} = 2.70$ .



- $\circ$  Bottom center line
- $\square$  Bottom left
- $\diamond$  Bottom right

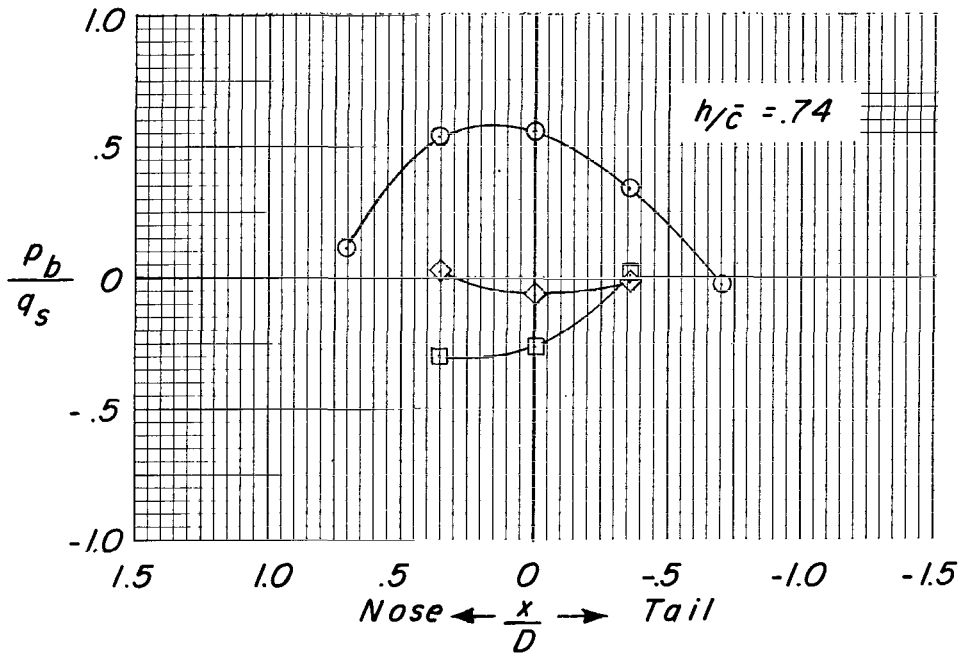
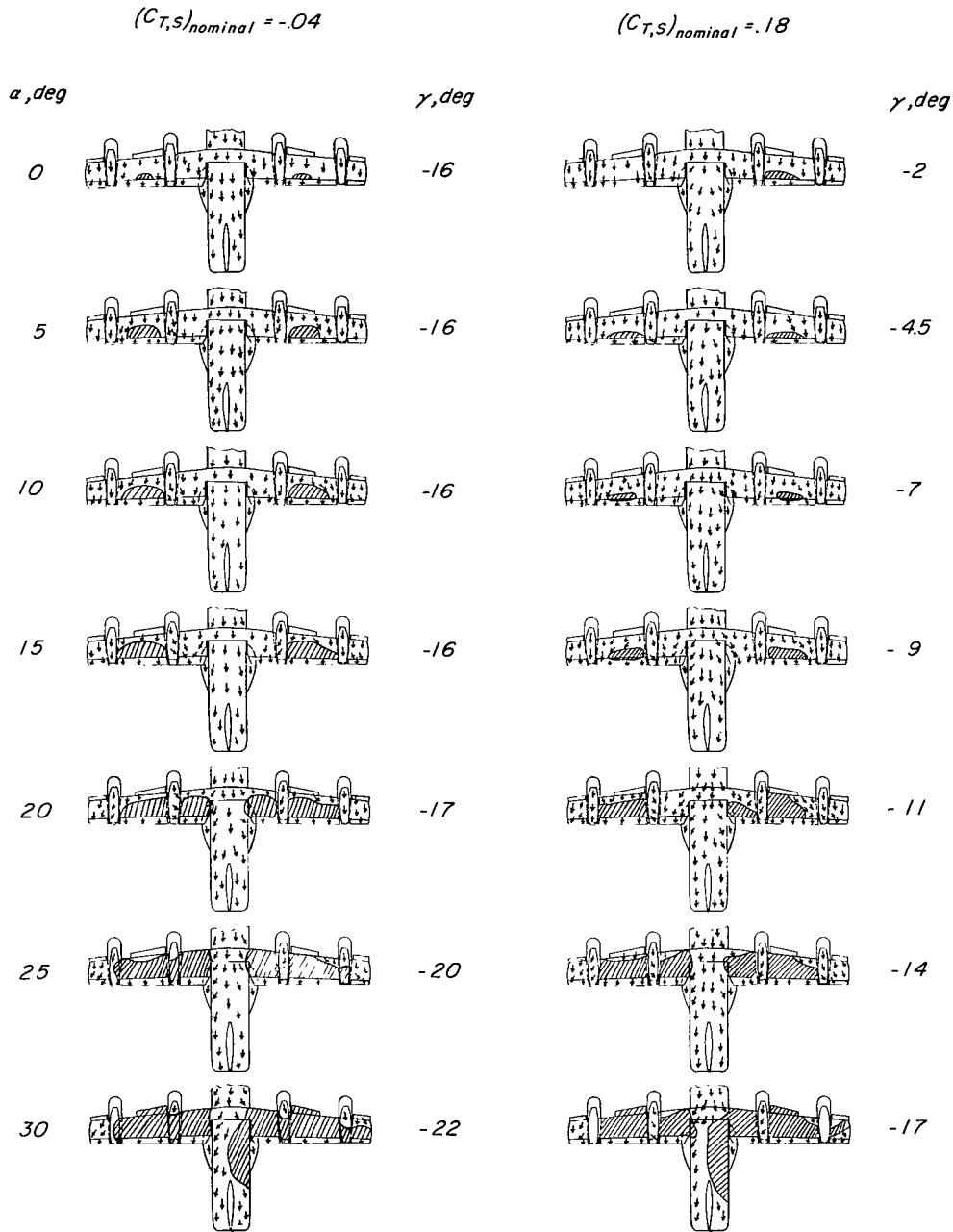


Figure 28.- Effect of aerodynamic pressure on fuselage bottom of a four-propeller tilt-wing VTOL model at zero velocity for several ground heights.  $\alpha = 0^\circ$ ;  $i_w = 90^\circ$ ;  $\delta_f = 0^\circ$ ;  $i_t = 20^\circ$ ; slat off;  $\beta_{.75R} = 12^\circ$ ; 7500 rpm.

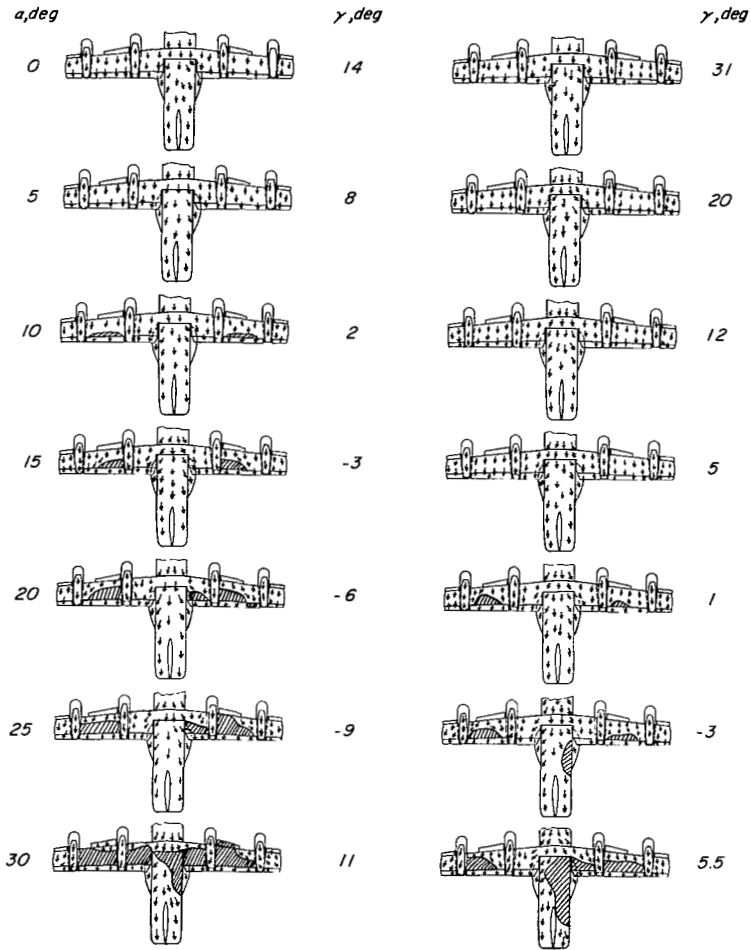


(a)  $i_w = 0^\circ$ ;  $\delta_f = 40^\circ$  (see fig. 13(a)).

Figure 29.- Flow patterns indicated by tufts on tilt-wing VTOL model at various thrust coefficients and wing incidence angles.  $S_1$  slat;  $h/\bar{c} = \infty$ ;  $i_t = 20^\circ$ ;  $\beta_{.75R} = 12^\circ$ .

$(C_{T,S})_{nominal} = .41$

$(C_{T,S})_{nominal} = .59$

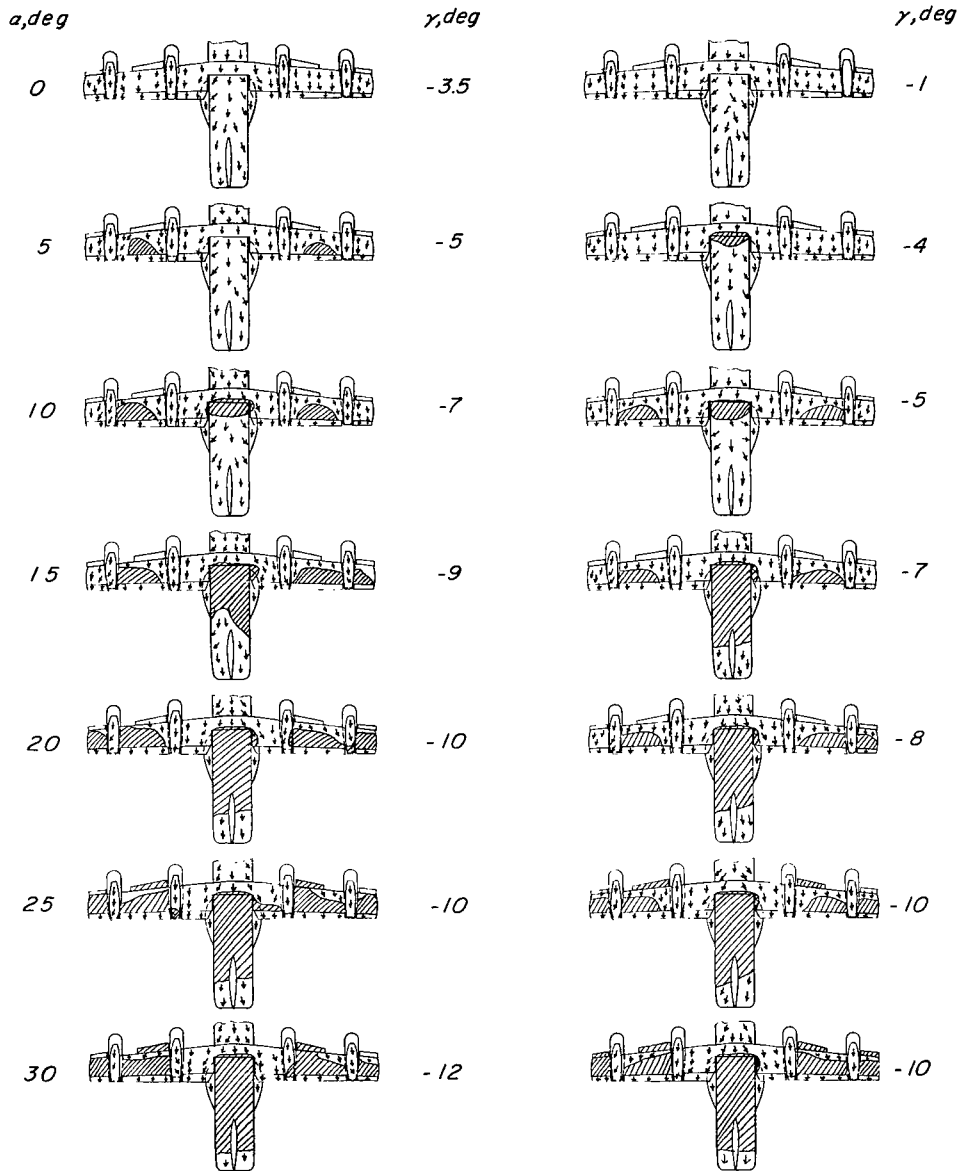


(a) Concluded.

Figure 29,- Continued.

$(C_{T,S})_{nominal} = .63$

$(C_{T,S})_{nominal} = .73$



(b)  $i_w = 20^\circ$ ;  $\delta_f = 60^\circ$  (see fig. 14(c)).

Figure 29.- Continued.

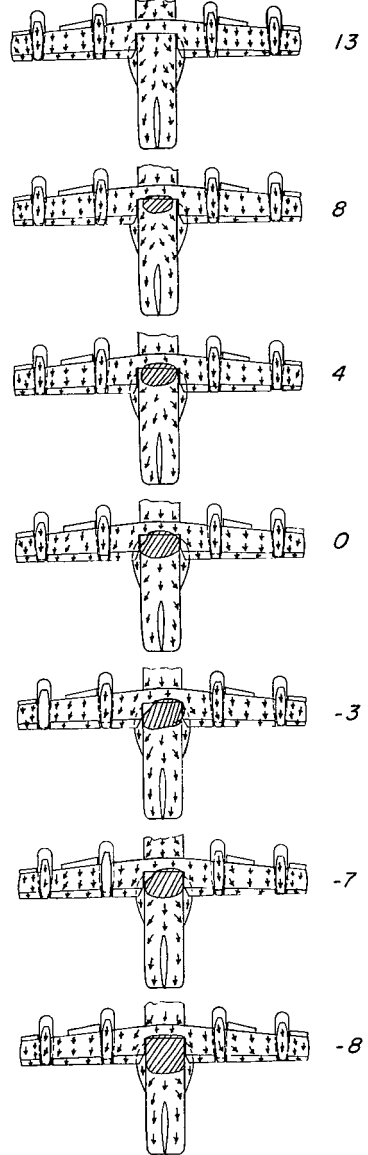
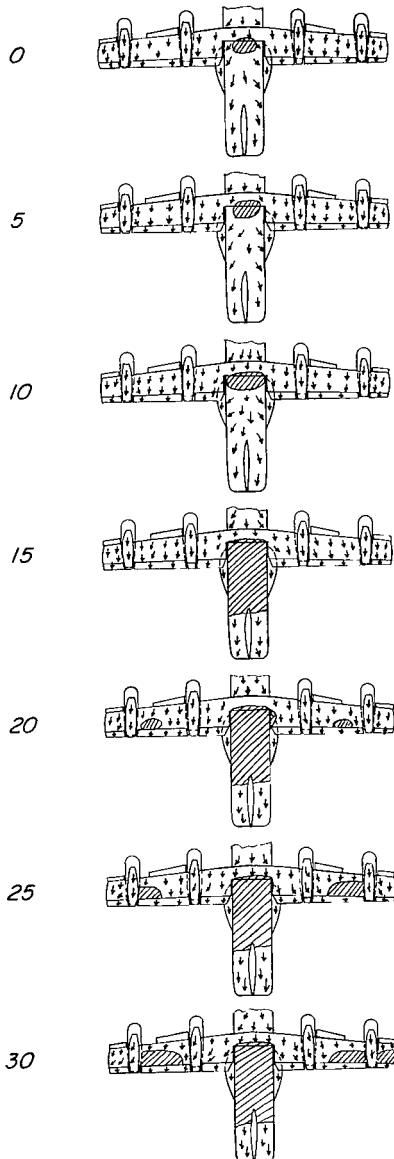
$(C_{T,S})_{nominal} = .82$

$(C_{T,S})_{nominal} = .89$

$a, deg$

$\gamma, deg$

$\gamma, deg$



(b) Concluded.

Figure 29.- Continued.

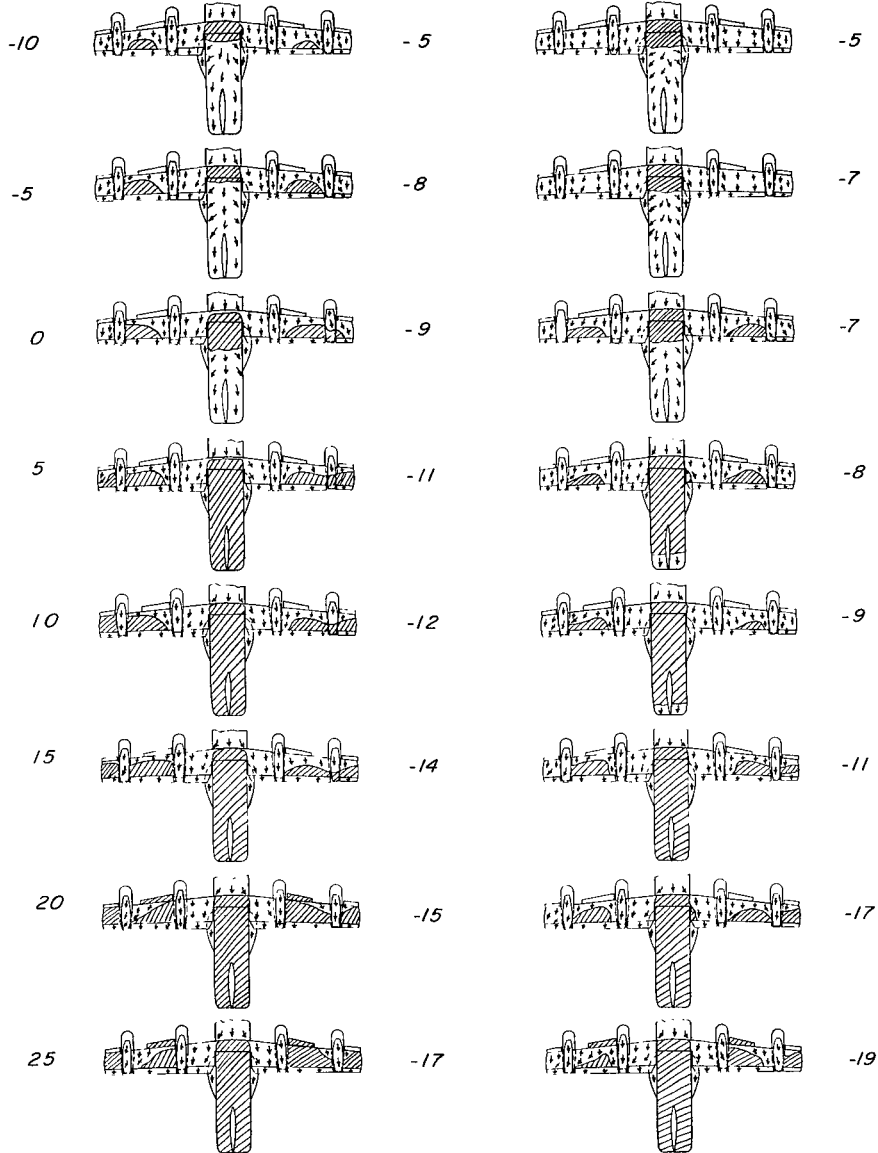
$(C_{T,S})_{nominal} = .75$

$(C_{T,S})_{nominal} = .83$

$\alpha, deg$

$\gamma, deg$

$\gamma, deg$

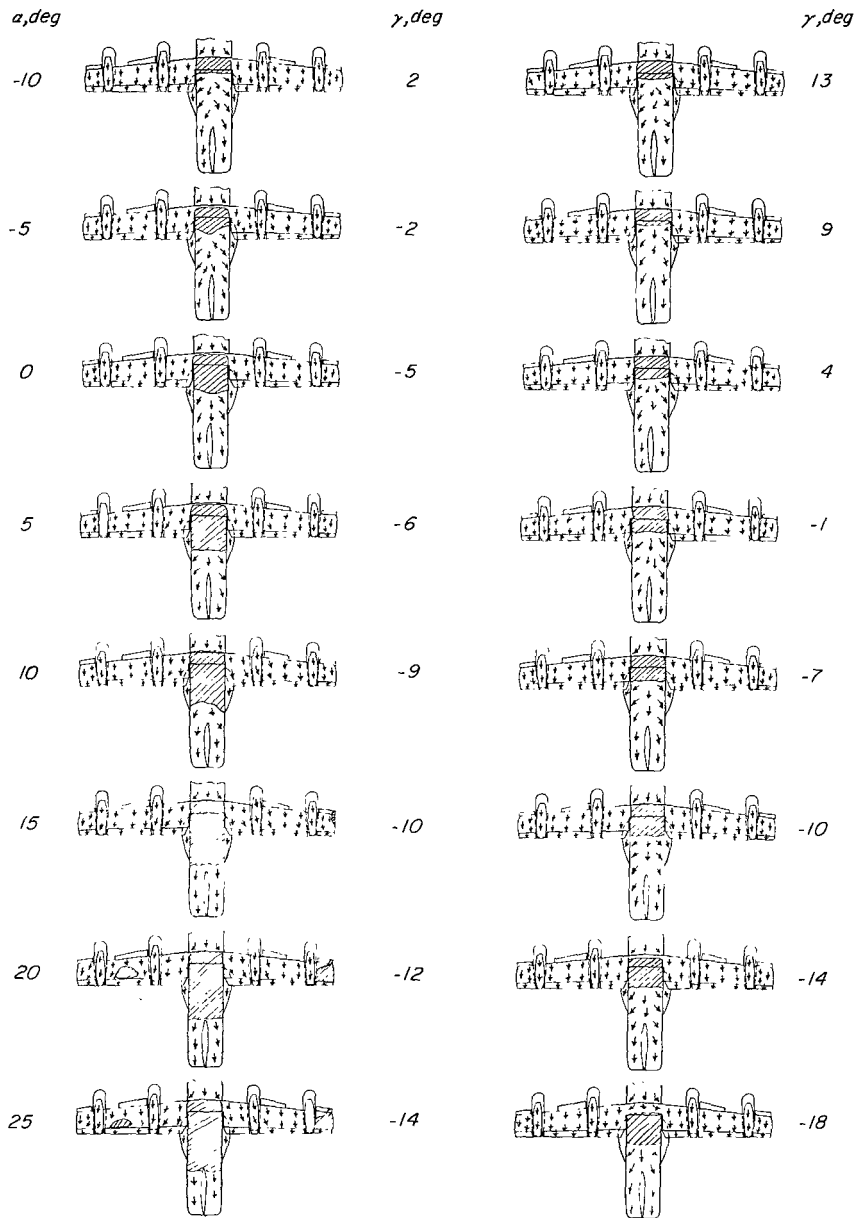


(c)  $i_w = 40^\circ$ ;  $\delta_f = 60^\circ$  (see fig. 14(e)).

Figure 29.- Continued.

$(C_{T,S})_{nominal} = .90$

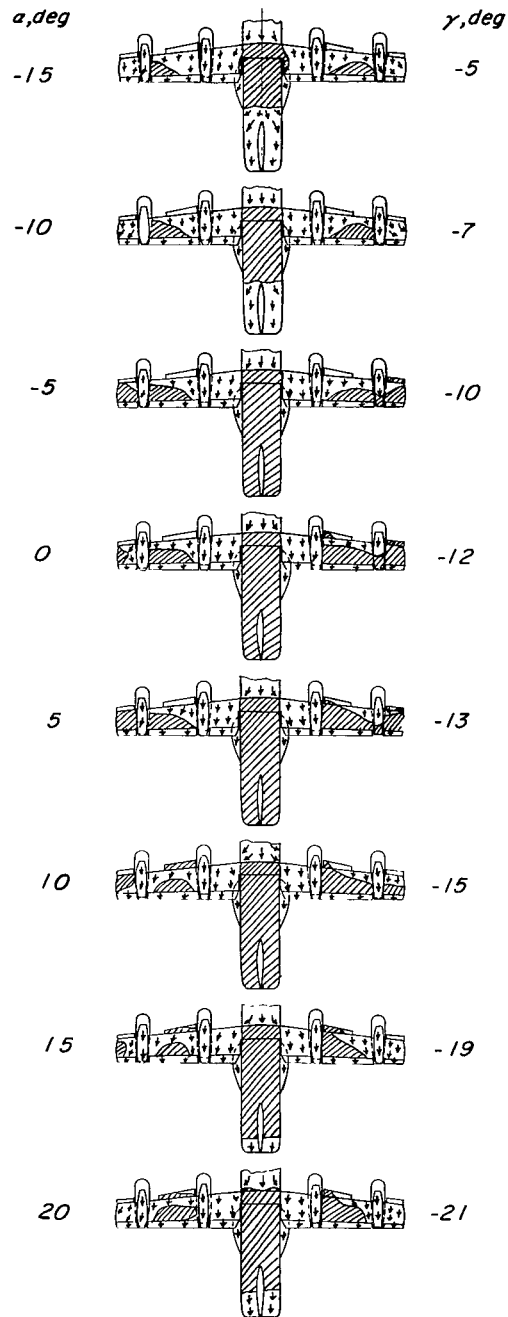
$(C_{T,S})_{nominal} = .96$



(c) Concluded.

Figure 29.- Continued.

$$(C_{T,S})_{nominal} = .79$$

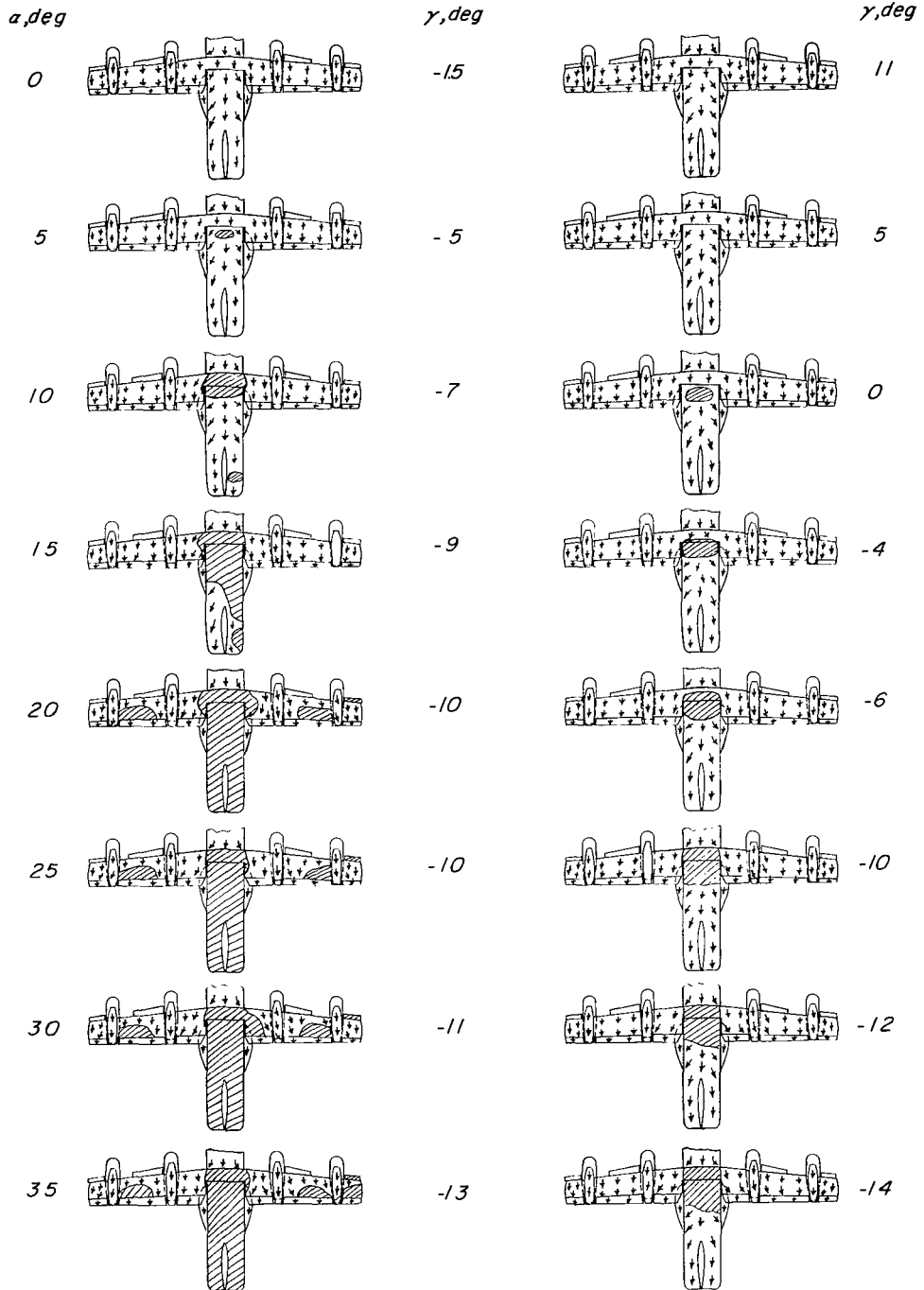


(d)  $i_w = 56^\circ$ ;  $\delta_f = 40^\circ$  (see fig. 13(d)).

Figure 29.- Concluded.

$(C_{T,S})_{nominal} = .77$

$(C_{T,S})_{nominal} = .92$

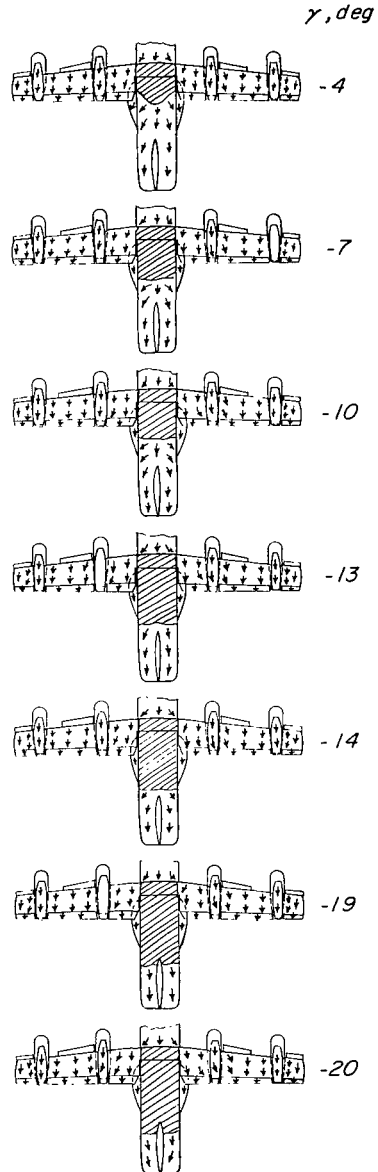
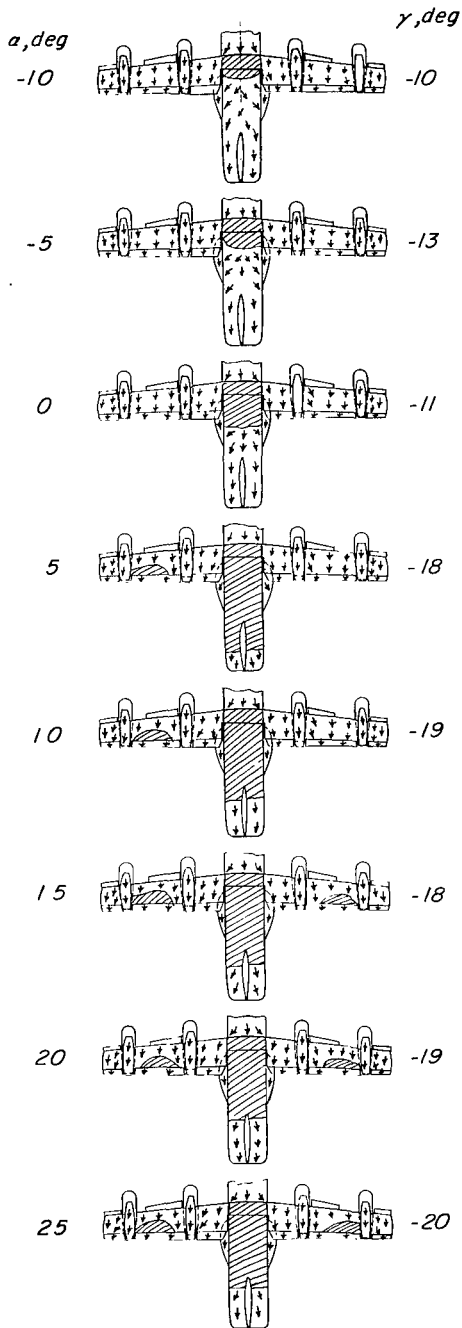


(a)  $i_w = 20^\circ$ ;  $\delta_f = 60^\circ$  (see fig. 23(b)).

Figure 30.- Flow patterns indicated by tufts on tilt-wing model at various thrust coefficients and wing-incidence angles.  $S_1$  slats;  $h/\bar{c} = \infty$ ;  $i_t = \text{off}$ ;  $\beta_{.75R} = 8^\circ$ .

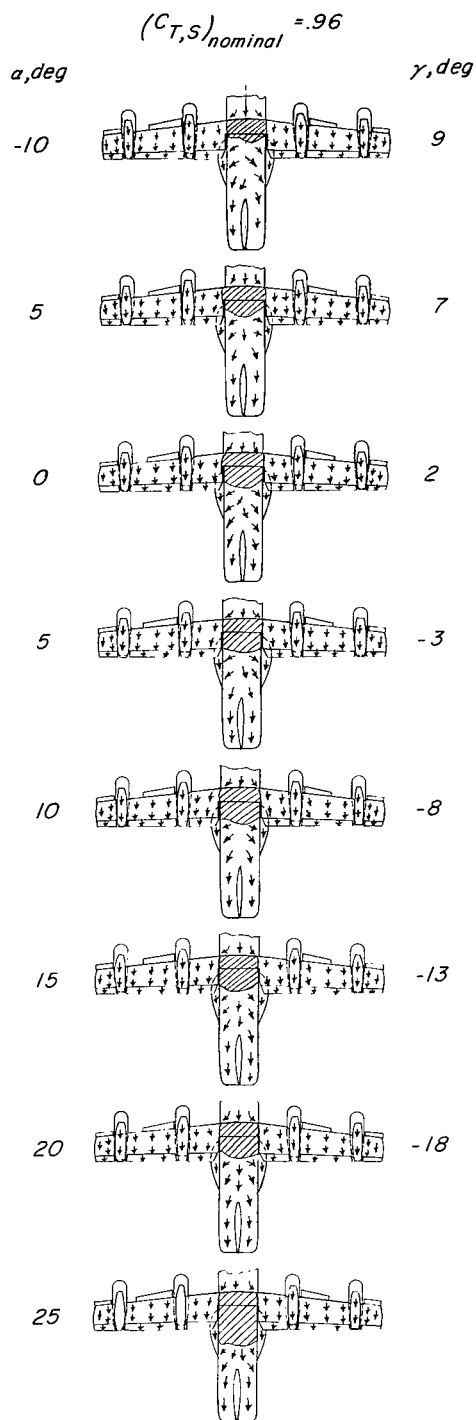
$(C_{T,S})_{nominal} = .85$

$(C_{T,S})_{nominal} = .92$



(b)  $i_w = 40^{\circ}$ ;  $\delta_f = 60^{\circ}$  (see fig. 23(c)).

Figure 30.- Continued.



(b) Concluded.

Figure 30.- Concluded.

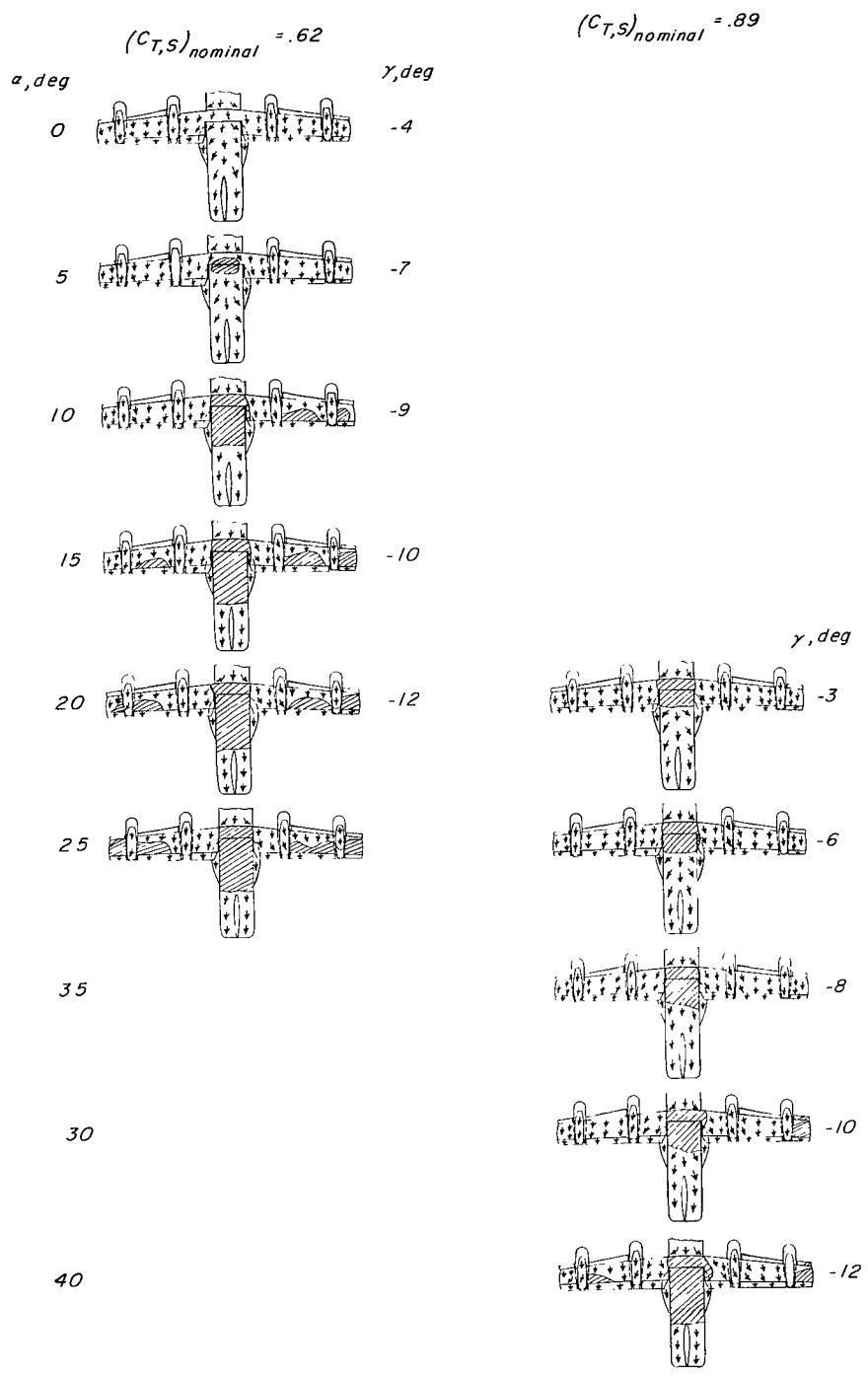
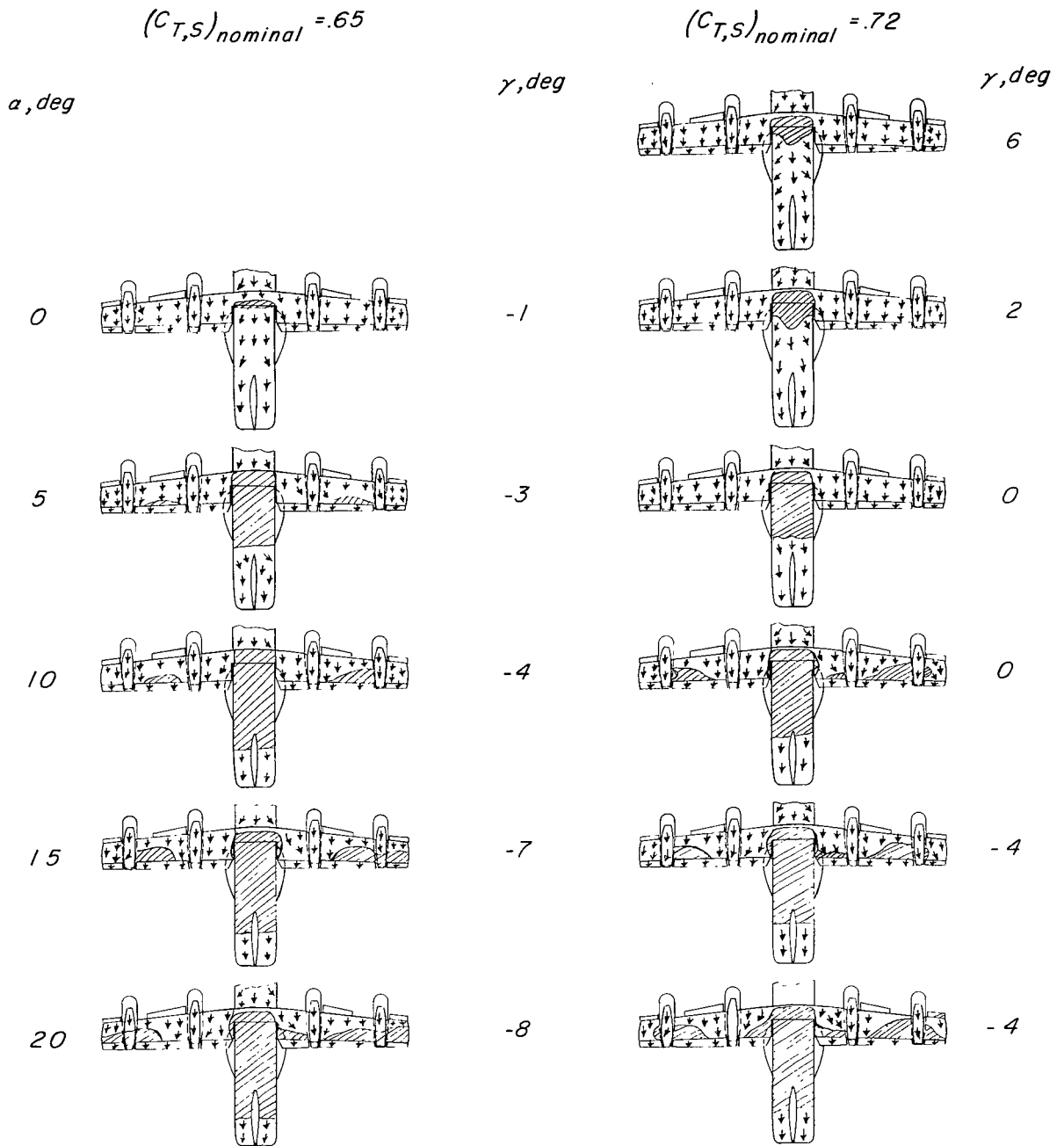
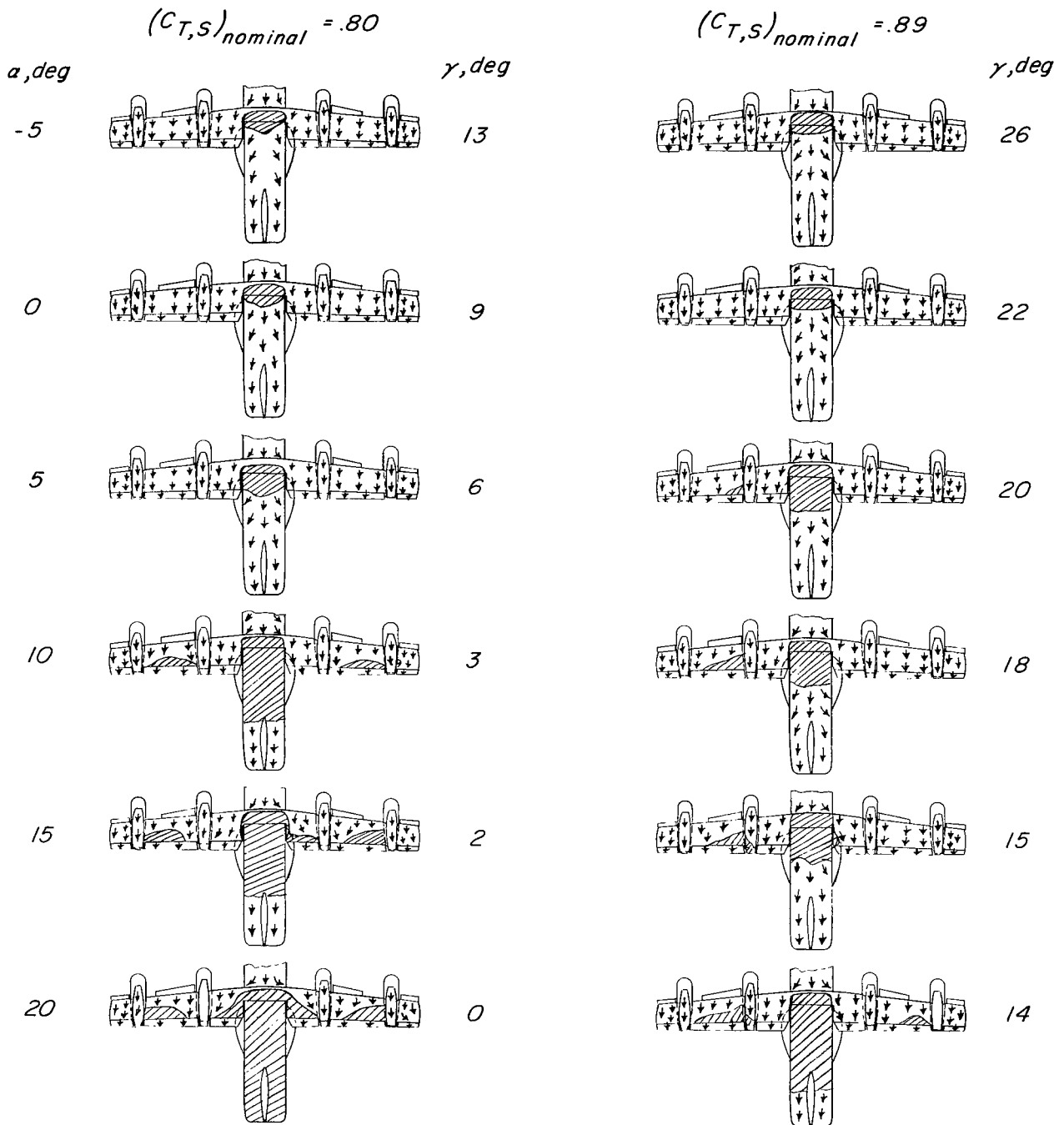


Figure 31.- Flow patterns indicated by tufts on tilt-wing VTOL model at various thrust coefficients and wing-incidence angles.  $h/\bar{c} = \infty$ ;  $\beta_{.75R} = 12^\circ$ ;  $i_t = 10^\circ$ ;  $i_w = 20^\circ$ ;  $\delta_f = 60^\circ$ ; S2 slat. (See fig. 24.)



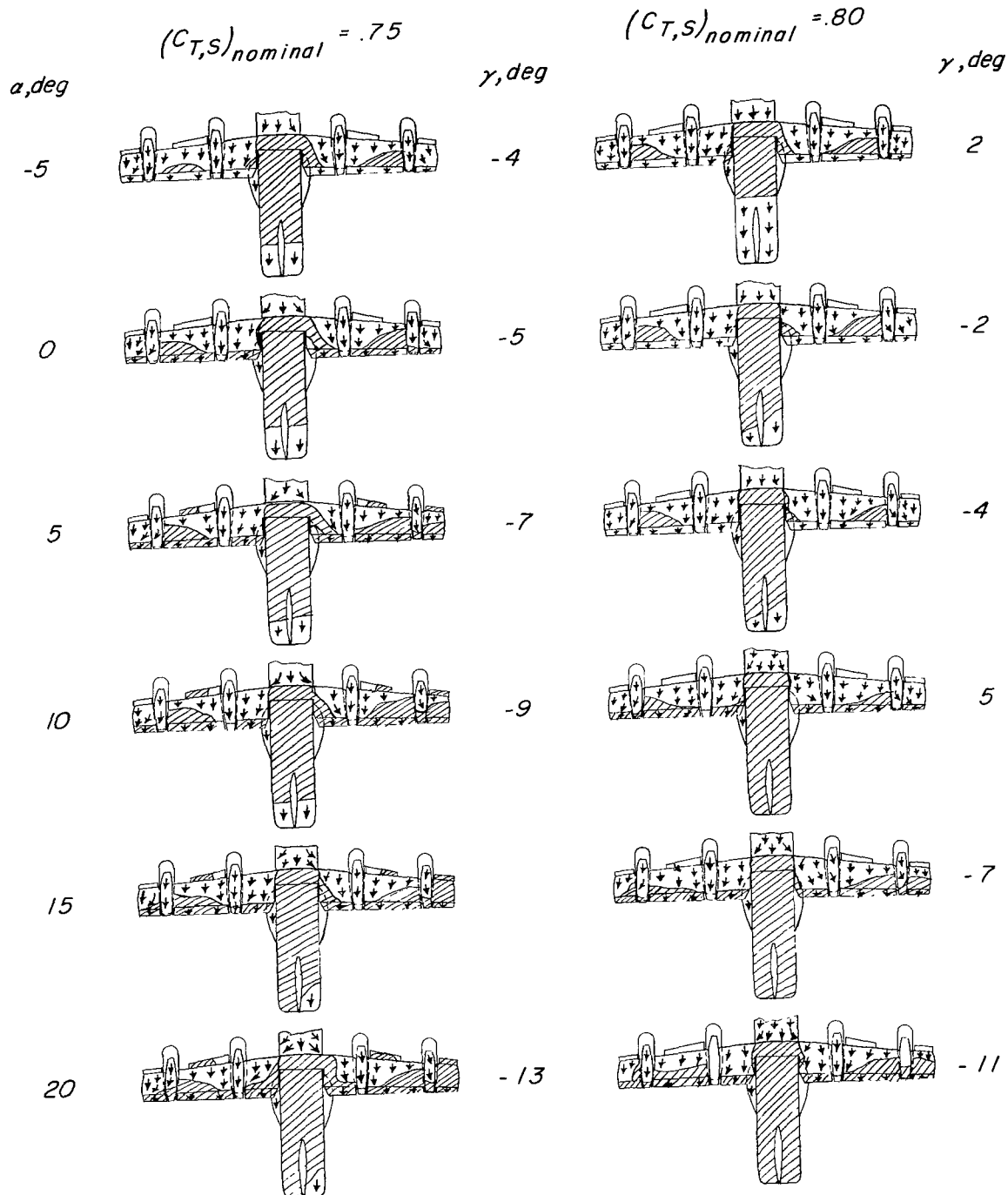
(a)  $i_w = 20^\circ$ ;  $\delta_f = 60^\circ$ .

Figure 32.- Flow patterns indicated by tufts on tilt-wing VTOL model at various thrust coefficients and wing-incidence angles.  $S_1$  slat;  $\beta_{.75R} = 12^\circ$ ;  $h/\bar{c} = 0.74$ . (See fig. 26.)



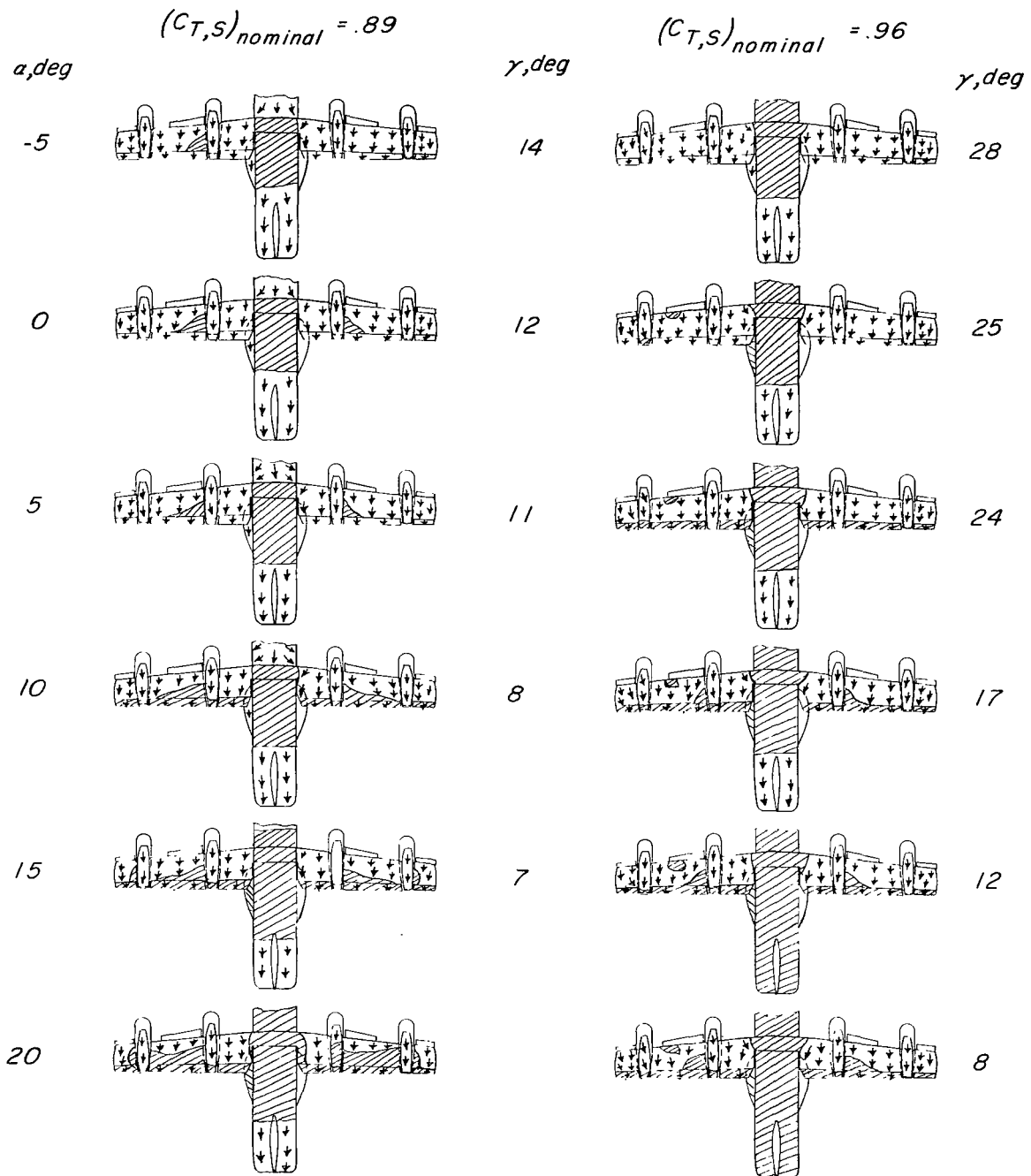
(a) Concluded.

Figure 32.- Continued.



(b)  $i_w = 40^\circ$ ;  $\delta_f = 60^\circ$ .

Figure 32.- Continued.



(b) Concluded.

Figure 32.- Concluded.

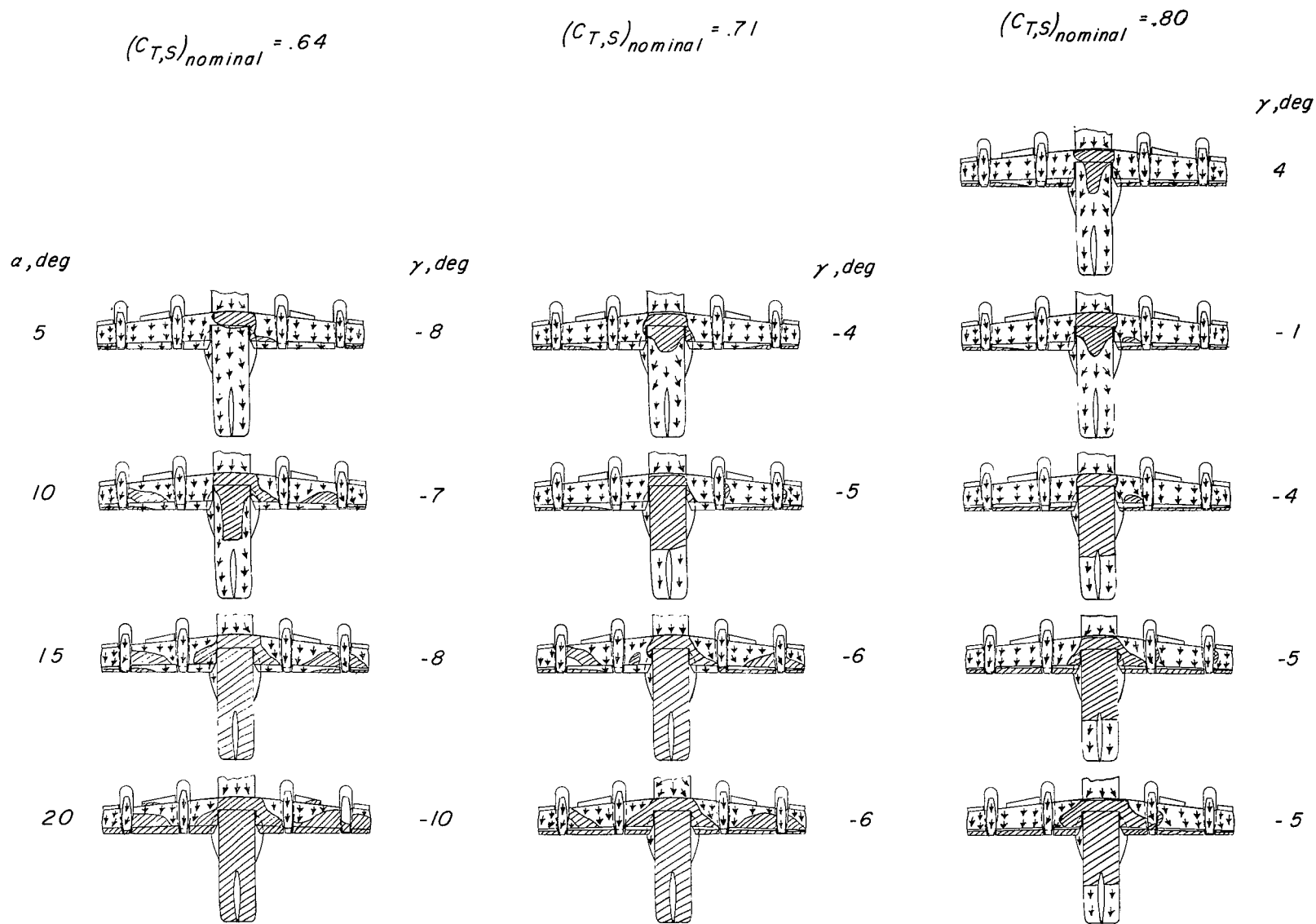


Figure 33.- Flow patterns indicated by tufts on tilt-wing VTOL model at various thrust coefficients and wing-incidence angles.  $S_1$  slat;  $\beta_{.75R} = 12^\circ$ ;  $i_w = 20^\circ$ ;  $\delta_f = 60^\circ$ ;  $h/\bar{c} = 2.7$ .

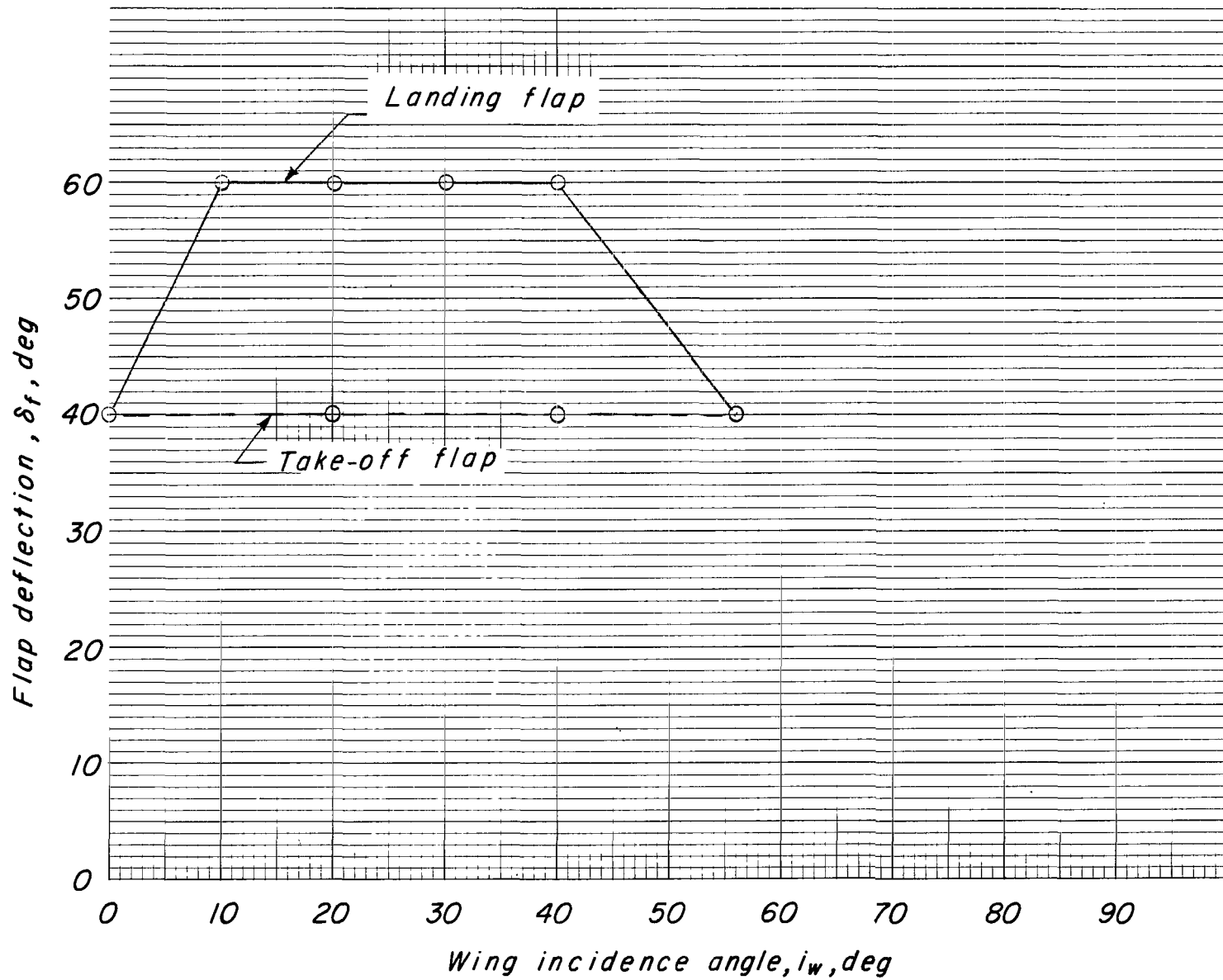


Figure 34.- Wing incidence - flap deflection program for tilt-wing VTOL model.

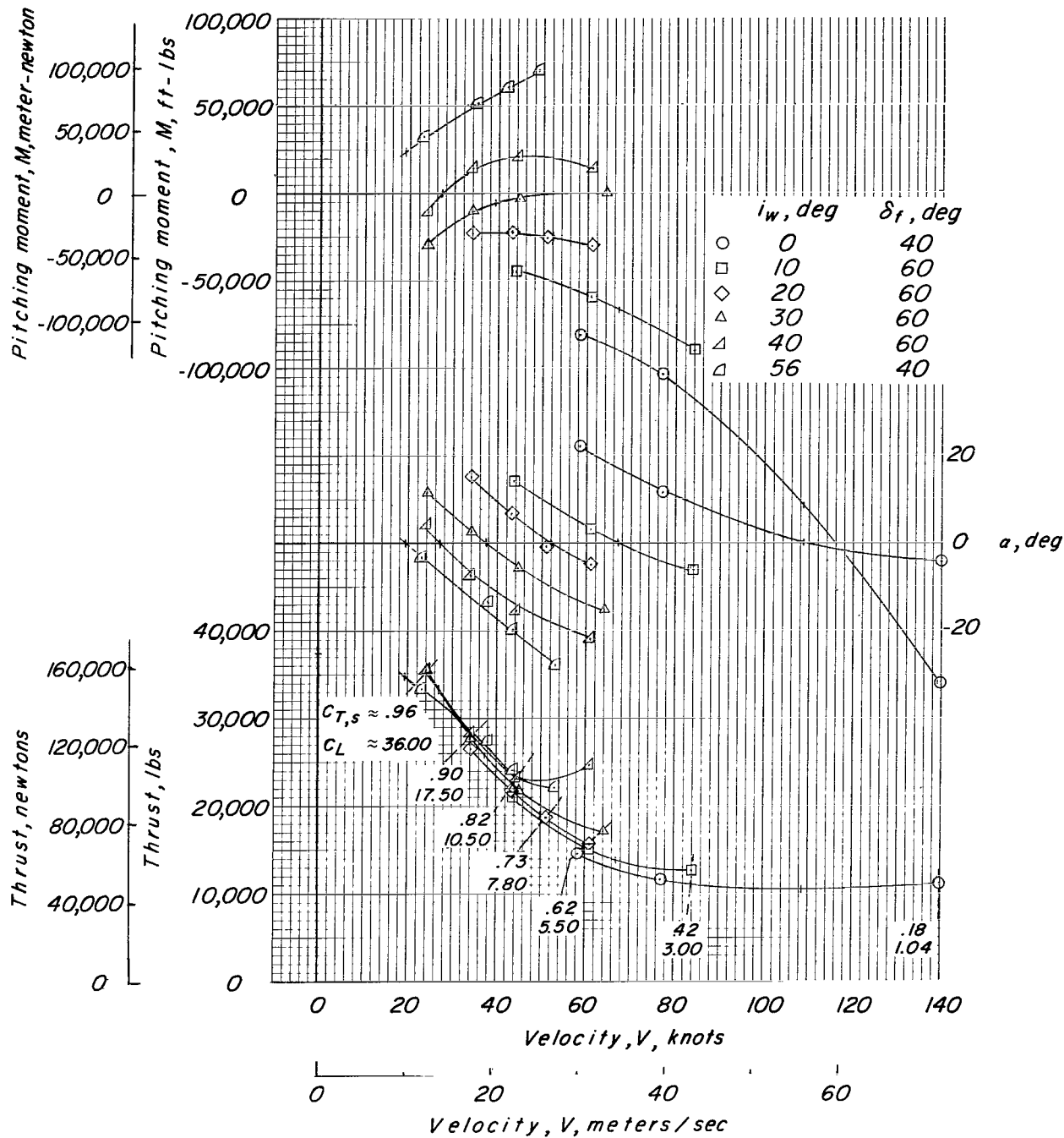


Figure 35.- Typical set of scaled-up wind-tunnel transition data for assumed tilt-wing VTOL airplane.  $W/S = 70 \text{ lb/ft}^2$  ( $3350 \text{ newtons/meter}^2$ );  $C_{D,s} = 0$ ;  $\gamma = 0^\circ$ ;  $h/\bar{c} = \infty$ ;  $i_t = 20^\circ$ .

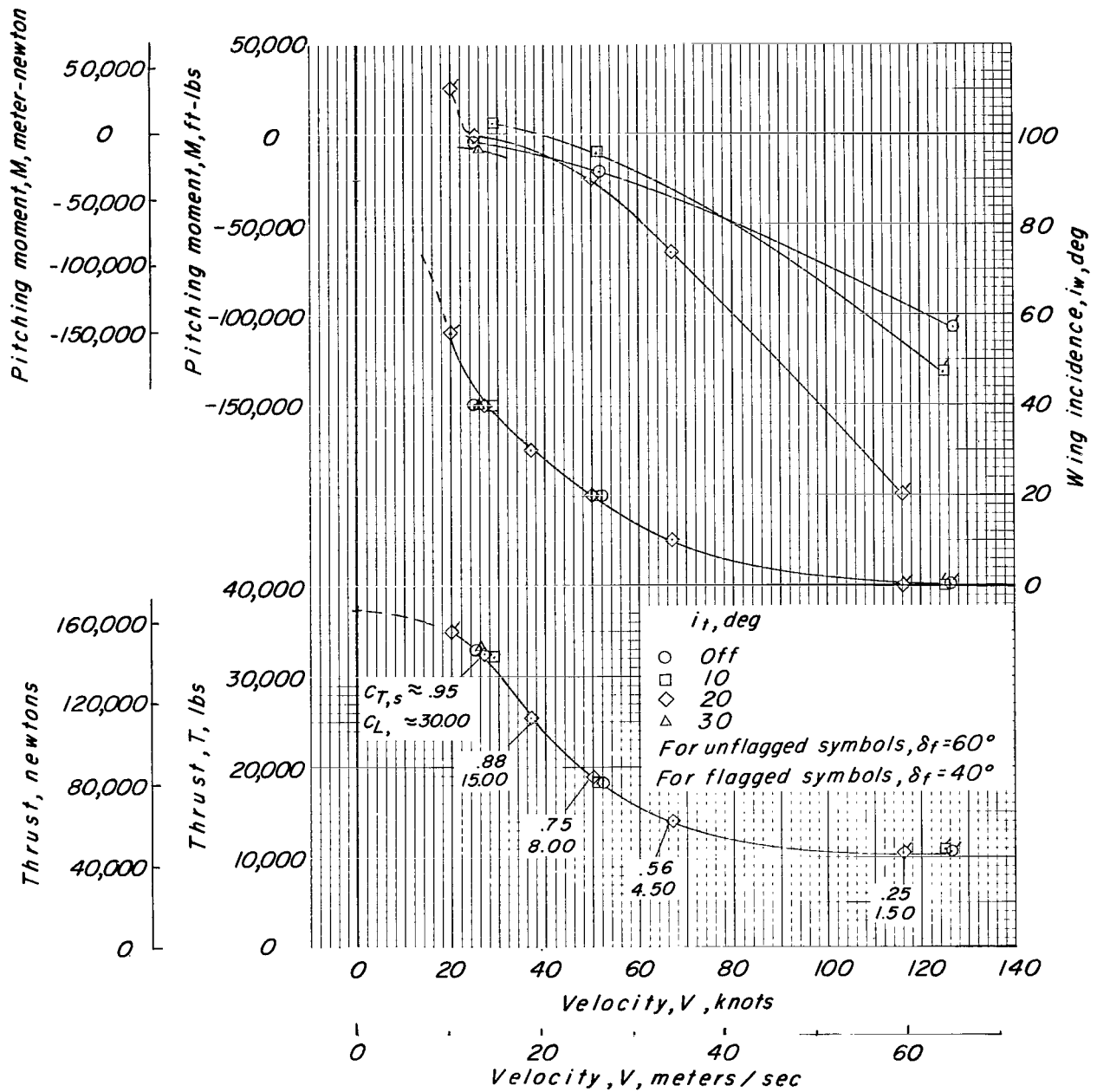


Figure 36.- Effect of horizontal-tail incidence on steady-level flight transition characteristics of assumed tilt-wing VTOL airplane.  
 $W/S = 70 \text{ lb/ft}^2$  (3350 newtons/meter<sup>2</sup>);  $h/\bar{c} = \infty$ ;  $i_t = 20^\circ$ ;  $\alpha = 0^\circ$ .

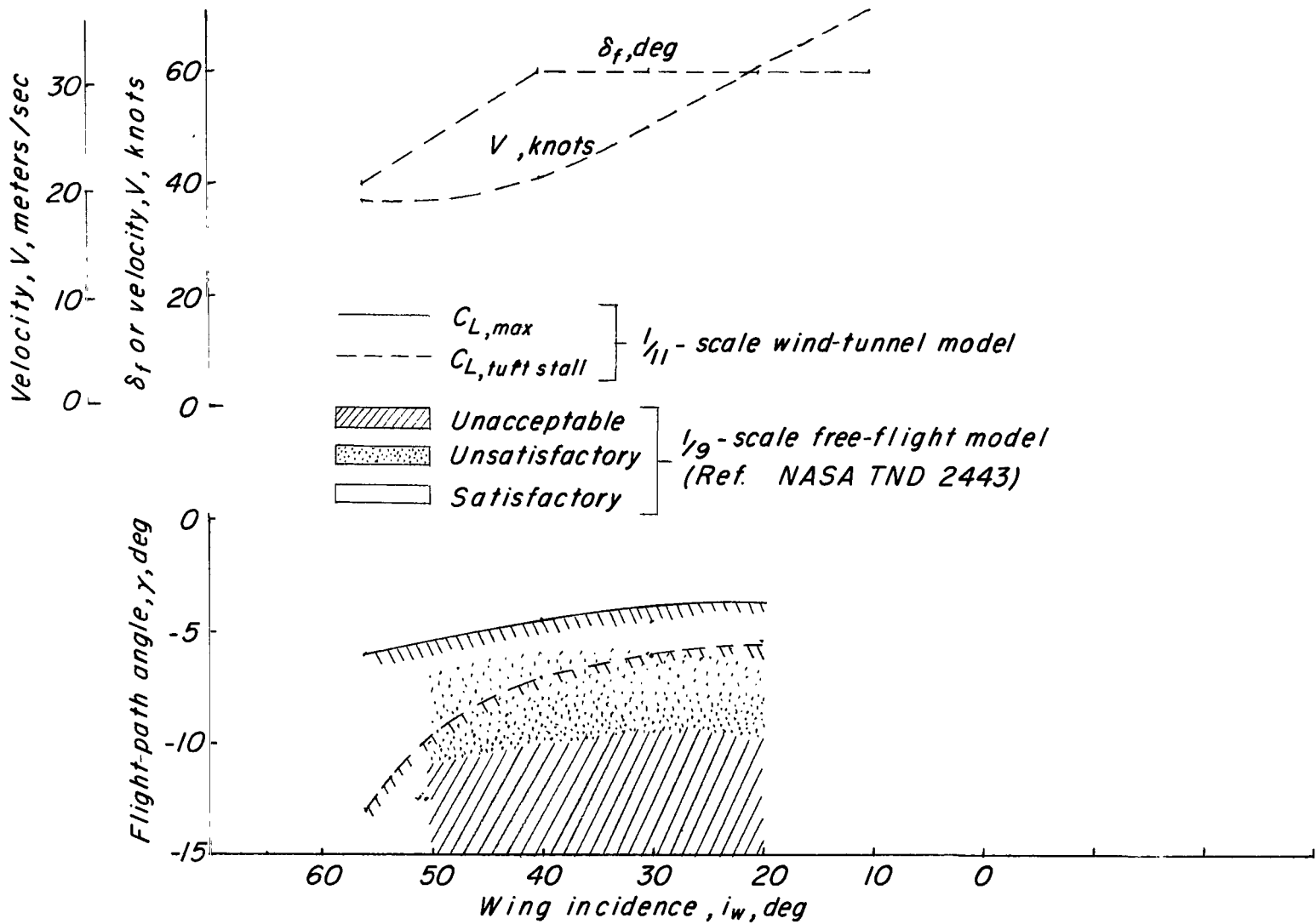


Figure 37.- Comparison of descent boundaries obtained by several techniques for four-propeller, tilt-wing VTOL configuration.  $h/\bar{c} = \infty$ ;  $\alpha = -\gamma$ ;  $W/S = 70 \text{ lb/ft}^2$  (3350 newtons/meter<sup>2</sup>).

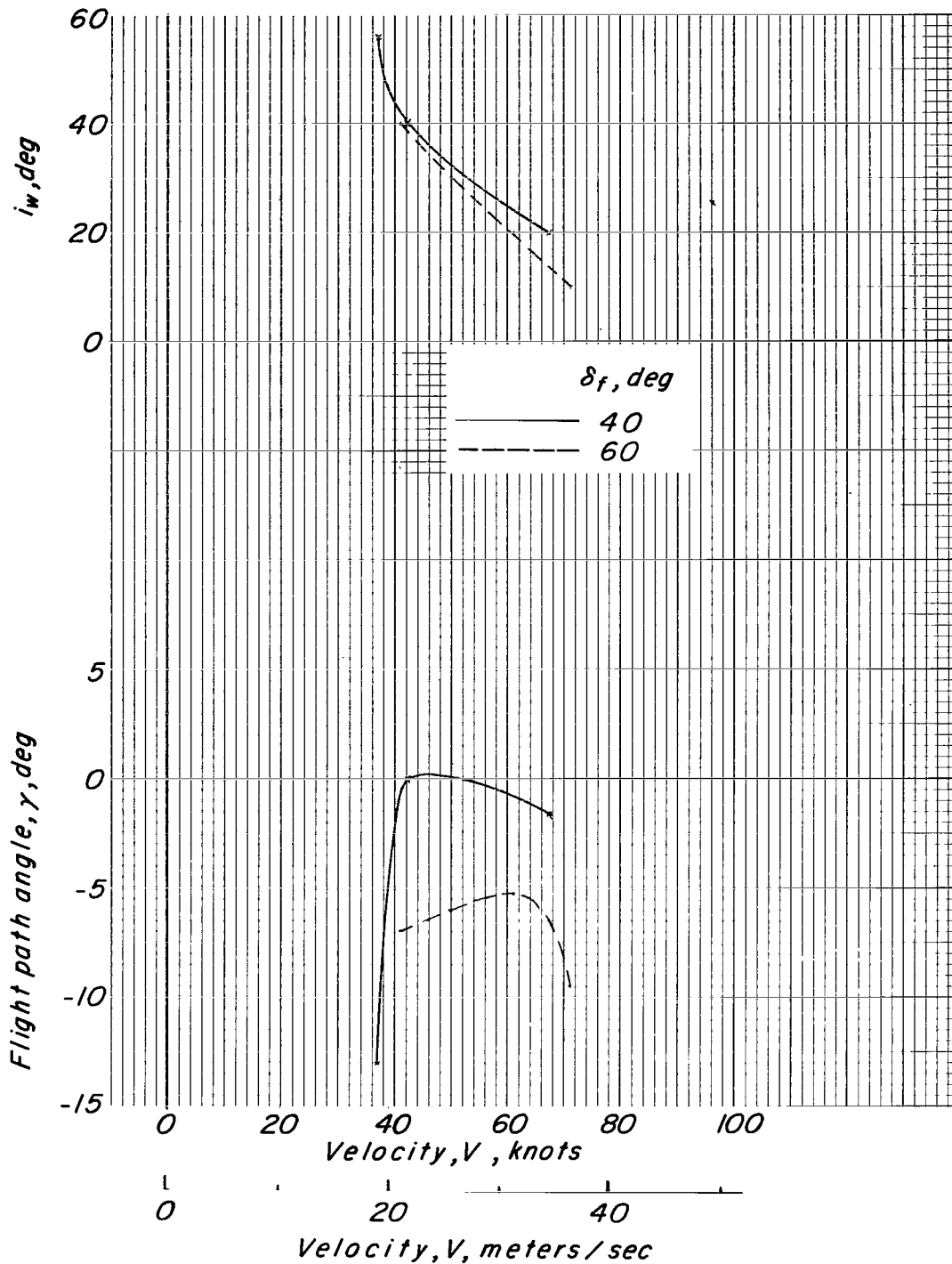


Figure 38.- Effect of flat deflection on descent boundaries in transition of assumed tilt-wing VTOL airplane. (Based on tuft stall.)  $W/S = 70 \text{ lb/ft}^2$  (3350 newtons/meter<sup>2</sup>);  $h/\bar{c} = \infty$ ;  $\alpha = \gamma$ .

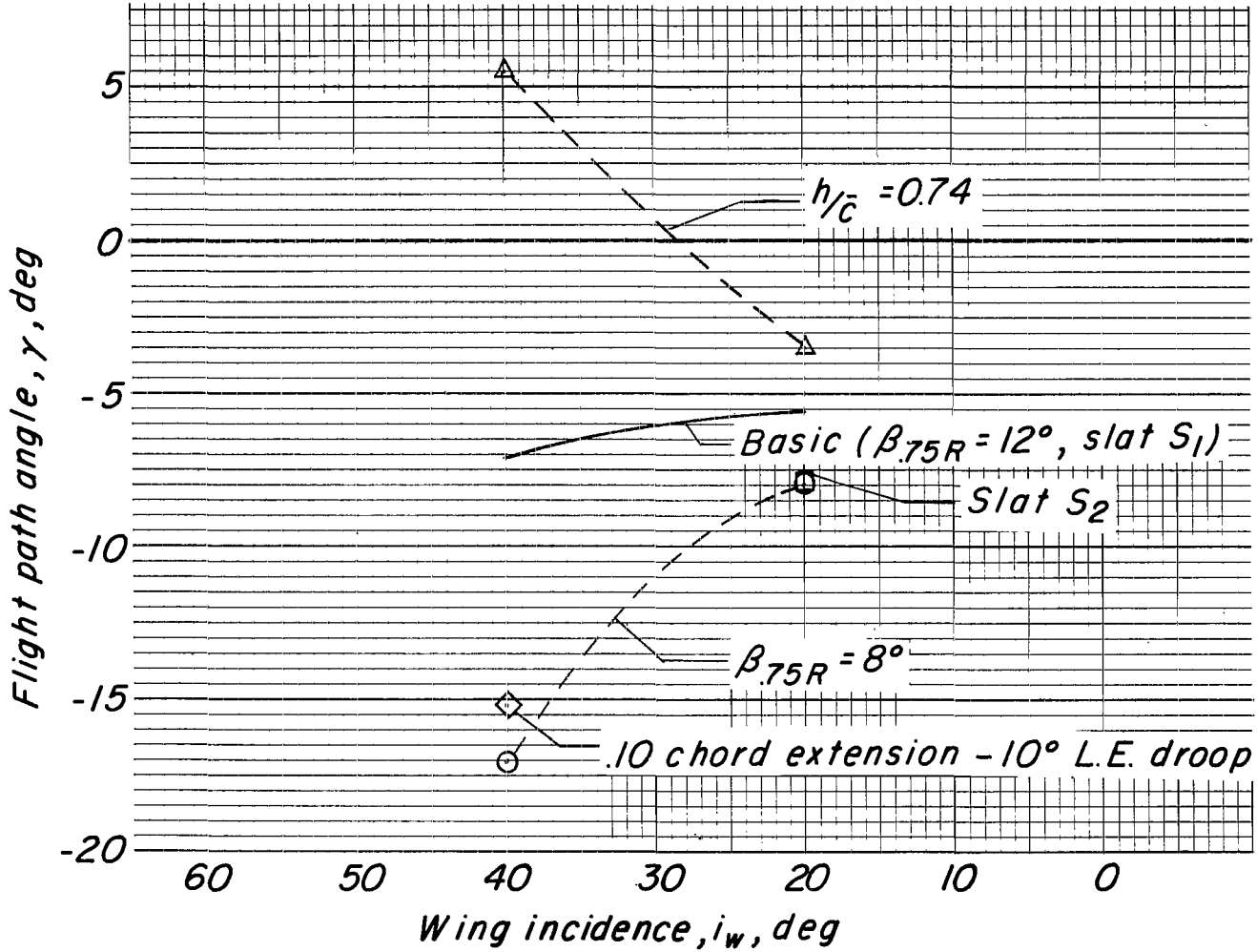


Figure 39.- Effect of various configuration changes on angle of descent of assumed tilt-wing VTOL airplane. (Based on tuft stall.)  $W/S = 70 \text{ lb/ft}^2 (3350 \text{ newtons/meter}^2)$ ;  $\alpha = -\gamma$ ;  $\beta_{75R} = 12^\circ$ , except as noted.

*"The aeronautical and space activities of the United States shall be conducted so as to contribute . . . to the expansion of human knowledge of phenomena in the atmosphere and space. The Administration shall provide for the widest practicable and appropriate dissemination of information concerning its activities and the results thereof."*

—NATIONAL AERONAUTICS AND SPACE ACT OF 1958

## NASA SCIENTIFIC AND TECHNICAL PUBLICATIONS

**TECHNICAL REPORTS:** Scientific and technical information considered important, complete, and a lasting contribution to existing knowledge.

**TECHNICAL NOTES:** Information less broad in scope but nevertheless of importance as a contribution to existing knowledge.

**TECHNICAL MEMORANDUMS:** Information receiving limited distribution because of preliminary data, security classification, or other reasons.

**CONTRACTOR REPORTS:** Technical information generated in connection with a NASA contract or grant and released under NASA auspices.

**TECHNICAL TRANSLATIONS:** Information published in a foreign language considered to merit NASA distribution in English.

**TECHNICAL REPRINTS:** Information derived from NASA activities and initially published in the form of journal articles.

**SPECIAL PUBLICATIONS:** Information derived from or of value to NASA activities but not necessarily reporting the results of individual NASA-programmed scientific efforts. Publications include conference proceedings, monographs, data compilations, handbooks, sourcebooks, and special bibliographies.

*Details on the availability of these publications may be obtained from:*

SCIENTIFIC AND TECHNICAL INFORMATION DIVISION  
NATIONAL AERONAUTICS AND SPACE ADMINISTRATION  
Washington, D.C. 20546